Micro and Nano Scale Structure Design of Sn-Based Phase Change Materials for Thermal Energy Storage

熱エネルギー貯蔵のための Sn 系相変化材料の

マイクロおよびナノスケール構造設計

ZHU Shilei

Graduate School of Engineering

Hokkaido University

September 2019

(blank)

A dissertation submitted to the

Graduate School of Engineering, Hokkaido University, for the degree of

Doctor of Philosophy in Materials Science and Engineering

(blank)

Abstract

Phase change materials (PCMs) are the materials that use phase transition process to achieve certain designed functions. In terms of thermal energy storage (TES), PCMs can be used to store and release thermal energy at a constant temperature through reversible phase transition. This feature makes them suitable storage medium in TES and the heat sink in thermal management of electronic devices. Compared to the common PCMs, like organic compounds and inorganic salts, metals exhibit high volumetric TES density which is helpful for a compact system, and high thermal conductivity which enable the fast charge and discharge of thermal energy. However, the metal PCMs should be encapsulated to avoid corrosion to container, morphology changes and deterioration of micro and nano scale metal PCMs. This thesis focuses on the nanostructure design of micro and nano scale Sn-based PCMs on the purpose of encapsulation of metal PCMs for long-term cyclic stability and morphology control.

In Chapter 1, the research background and objectives of this research are introduced.

In Chapter 2, silica was selected as the material of the protection shell for Sn PCM. A facile method was proposed for preparing a silica (SiO_2)-based material containing Sn nanoparticles (NPs) distributed inside for enhancing the thermal cyclic stability of the inserted Sn NPs. Absorption of a Sn precursor into a mesoporous SiO_2 matrix resulted in confinement of the Sn precursor in a mesoporous SiO_2 matrix. Hydrogen thermal reduction of the above composite yielded Sn nanoparticles with a diameter of ca. 30 nm uniformly distributed inside porous SiO_2 (p-SiO_2) spheres: Sn NPs@p-SiO_2. The transformation of the porous SiO_2 structure for supporting Sn NPs revealed that the process was closely related to the transformation of the amorphous hydrolyzed Sn precursor into Sn oxides followed by, probably, the rearrangement of the SiO_2 matrix via its interaction with the melting Sn. This led to the formation of stable Sn NPs@p-SiO_2. The SiO_2 matrix effectively prevented the coalescence of the Sn NPs, and the obtained product exhibited negligible changes in melting behavior during the second to 100th cycle of a freeze-melt cycle test.

In Chapter 3, alumina with higher thermal conductivity compared to silica was selected as the material of the protection shell. In this part, for the first time, alumina-encapsulated metallic Sn-based PCMs, named Sn@Al_2O_3, were successfully fabricated with tunable size (60 nm-2 μm) and core-shell structure by a facile process from low-cost chemicals. The robust fabrication process consists of a surfactant-free solvothermal synthesis of SnO_2 spheres, boehmite treatment on SnO_2 spheres, calcination in the air, and the final hydrogen reduction to transform SnO_2 to metallic

Sn. The boehmite treatment, in which the penetration of aluminum species into SnO_2 spheres played an important role, was found to be responsible for the unique structure formation of final $Sn@Al_2O_3$. The understanding of structure formation mechanism gives the possibilities of a new facile way for the synthesis of metal NPs and particle-distributed nanostructures. The obtained $Sn@Al_2O_3$ particles not only have high PCM content (92.37 wt%) but also show a stable thermal behavior and morphology during 100 melt- freeze cycles in the air atmosphere, exhibiting the potential of fast thermal energy storage within the range of 100-300°C.

In Chapter 4, the formation of $SnO_2@SiO_2$ hollow nanostructures was demonstrated, for the first time, by diffusion of liquid state Sn cores in $Sn@SiO_2$ core-shell NPs and further interaction with SiO_2 with real-time observation via in situ transmission electron microscopy (TEM). Based on the in-situ results, a designed transformation of nanoparticle structure from core-shell $Sn@SiO_2$ to yolk-shell $Sn@SiO_2$ and hollow $SnO_2@SiO_2$ is demonstrated, showing the controllable structure from starting core-shell $Sn@SiO_2$ NPs via liquid state Sn diffusion in SiO_2 shell and further fixing of Sn by interaction with the dangling bond of SiO_2. The proposed approach expands the toolbox for the design and preparation of yolk-shell and hollow nanostructure, thus provides us a new strategy in fabrication of more complicated nanostructures, which can not only be applied in PCMs design but also in catalyst, batteries, etc.

Finally, Chapter 5 is a summary of all the results obtained in each chapter and prospective for future research in the above areas.

Contents

Chapter 1. General Introduction 1

1.1 Thermal Energy Storage 1

1.1.1 Classification of Thermal Energy Storage 5

1.2 Phase Change Materials 7

1.2.1 Selection Criteria of PCMs 9

1.2.1.1 Thermal Properties 9

1.2.1.2 Physical Properties 10

1.2.1.3 Kinetic Properties 11

1.2.1.4 Chemical Properties 11

1.2.2 Classification of PCMs 12

1.2.2.1 Organics 12

1.2.2.2 Inorganics 14

1.3 Low Melting Point Metals for PCMs 16

1.4 Micro/Nano Encapsulation of PCMs 19

1.4.1 Approaches for Micro/Nano Encapsulation of PCMs 21

1.4.1.1 Polymerization Methods 21

1.4.1.2 Physico-Chemical Methods 22

1.4.1.3 Physical Methods 23

1.4.2 Micro/Nano Encapsulation of Metals and Alloys 24

1.4.2.1 Micro/Nano Encapsulation of Low Melting Point Metals and Alloys 24

1.4.2.2 Micro/Nano Encapsulation of High Melting Point Metals and Alloys 33

1.5 The Objectives of This Study 43

References 43

Chapter 2. Porous SiO_2 Spheres Encapsulated Sn Nanoparticles for Thermal Energy Storage 51

Abstract 52

2.1 Introduction 52

2.2 Experimental 54

2.2.1 Chemicals 54

2.2.2 Preparation of p-SiO_2 spheres. 54

2.2.3 Synthesis of Sn NPs@p-SiO_2 55

2.2.4 Characterization 55

2.3 Results and Discussions 56

2.3.1 Preparation strategy of Sn NPs@p-SiO_2 56

2.3.2 Confirmation of the obtained Sn NPs@*p*-SiO_2 structure 57

2.3.3 Formation mechanism of the Sn NPs@p-SiO_2 structure 63

2.3.4 Thermal Stability 74

2.4 Conclusions 77

References 79

Chapter 3. Al_2O_3 Encapsulated Sn Microparticles for Thermal Energy Storage 82

Abstract 83

3.1 Introduction 84

3.2 Materials and Methods 86

3.2.1 Chemicals 87

2.2.2 Synthesis of SnO_2 Spheres 87

3.2.3 Synthesis of Sn@Al_2O_3 87

3.2.4 Characterization 88

3.3 Results and Discussions 89

3.3.1 Morphology and Structure Characterizations of Sn@Al_2O_3 89

3.3.2 Structure Formation Mechanism 90

3.3.3 Thermal Storage Stability 99

3.4 Conclusions 107

References 108

Chapter 4. SiO_2 Encapsulated Core-Shell Nanoparticles: Structure Transformation via Liquid Metal Diffusions 111

Abstract 112

4.1 Introduction 113

4.2 Methods 114

4.2.1 Synthesis of Sn nanoparticles 115

4.2.2 Synthesis of Sn@SiO_2 core-shell nanoparticles 115

4.2.3 In situ TEM observation 116

4.2.4 Ex situ TEM observation 117

4.3. Results and discussion 117

4.3.1 Structure characterization 117

4.3.2 Dynamic motions of Sn nanodroplets inside SiO_2 structure..... 120

4.3.3 Outward diffusion of liquid-state Sn cores 123

4.3.4 Controllable nanostructure of Sn@SiO_2 129

4.4. Conclusions..... 135

References..... 136

Chapter 5. Conclusion and prospective 139

Appendix..... 141

A. Supporting Information for Chapter 2 141

B. Supporting Information for Chapter 3..... 151

C. Supporting Information for Chapter 4..... 161

Acknowledgments..... 170

Publication list 172

Conference 173

Tables

Table 1.1 Physical properties of low melting point metals and alloys. P16

Table 3.1 Summary of core-shell encapsulated low-melting-point metal PCMs. P112

Figures

Figure 1.1 Solar thermal power plants in Morocco. P3

(a) Noor 1: a parabolic-trough type CSP plant made up of 500,000 arched mirrors, each about 40 feet off the ground; (b) Noor 3: a tower type CSP plant (in construction).

Figure 1.2 Process of thermal energy storage in PCMs. P9

In solid-liquid PCMs, thermal energy is stored without increasing the temperature of the system at the melting temperature (T_m). During a certain range of temperature (ΔT, shown as green area), the thermal energy storage capacity of PCM is much higher than that of sensible heat storage materials.

Figure 1.3 Encapsulated Sn nanoparticles that synthesized by modified polyol reduction method followed by sol–gel silica encapsulation for advanced heat transfer and thermal energy storage. P26

TEM image of (a) as-prepared Sn nanoparticles and (b) Sn/SiO_2 nanoparticles; High-resolution TEM images of (c) Sn/SiO_2 phase change nanoparticles showing crystalline silica shell with a thick grain boundary between the shell and the Sn core. (d) Unencapsulated Sn nanoparticles showing amorphous SnO_x layer formed on the surface. TEM images of Sn/SiO_2 phase change nanoparticles (e) before and (f) after 20 heating and cooling cycles.

Figure 1.4 Synthesis and morphology of Zn@TiO_2 and Zn@Al_2O_3. P28

(A) Experimental procedure for synthesizing Zn/TiO_2 microparticles and Zn/Al_2O_3 microparticles, and the insert is a picture showing the synthesized Zn/Al_2O_3 microparticles. (B) SEM images of (a) pure Zn, (b) Zn/TiO_2, and (c) Zn/Al_2O_3

microparticles. (d) and (e) TEM cross-sectional images and EDS analysis for Zn/TiO_2 and Zn/Al_2O_3 microparticles, respectively.

Figure 1.5 Microencapsulated gallium–indium (Ga–In) liquid metal. P30

SEM images of Ga–In filled capsules at varying size scales. Capsules prepared (a) at an agitation rate of 1500 rpm (b) at an agitation rate of 2750 rpm and (c) via sonication.

Figure 1.6 Thermal and mechanical properties of graphite foam/Wood's alloy composite for thermal energy storage. P31

SEM image of (a) the unfilled graphite foam (b) the polished surface of the alloy filled graphite foam. (c) Thermal expansion of the Wood's alloy, graphite foam, and graphite foam/Wood's alloy composite. (d) The compression strength and bending strength of the composites as a function of the temperature.

Figure 1.7 Metal nanoparticle–carbon matrix composites with tunable melting temperature as PCMs for TES. P33

The different onset temperatures of the exothermic peaks show the tunable melting temperature of Pb@C composites.

Figure 1.8 Microencapsulation of Al-Si-based PCM for high-temperature thermal energy storage. P35

(A) SEM image of Al-Si MEPCM. (B) Cross-section EDS elemental mapping results of Al-Si MEPCM. (C) DSC curves of MEPCM at the first and after 10 melt-freeze cycles in air. (D) The changes in the latent heat of MEPCM during melt-freeze cyclic test. The inset SEM image shows the morphology of MEPCM after 10 melt-freeze cycles.

Figure 1.9 A microencapsulated Al–Si phase change material with high-temperature thermal stability and durability over 3000 cycles. P37

(a) Procedures for the preparation of Al-Si/Al_2O_3 core/shell MEPCM particles. (b) Evolution of latent heat of MEPCMs with the number of melting–solidification cycles. Inset shows the SEM images of the MEPCMs after 1000 melting–solidification cycles.

Figure 1.10 Inorganic microencapsulated core-shell structure of Al-Si alloy microparticles with silane coupling agent. P39

SEM images of Al-Si alloy microparticles (a) after surface modification and (b) after surface modification and heating at 400°C. The inset figure in b shows the sketch of Al-Si/Al_2O_3 core/shell particles. (c) Reaction mechanism of silane coupling agent treatment to Al–Si alloy.

Figure 1.11 Facile synthesis of Al@Al_2O_3 microcapsule via a Ni modified method for high-temperature thermal energy storage. P41

Figure 1.12 Synthesis of Al-25 wt% Si@Al_2O_3@Cu MEPCMs for high temperature thermal energy storage. P42

(a) SEM view and schematic of core/shell Al-25 wt% Si@Al_2O_3@Cu MEPCM particle. (b) Experimental procedure for Synthesis of Al-25 wt% Si@Al_2O_3@Cu MEPCM.

Scheme 2.1 Preparation of Sn NPs@p-SiO_2. P62

Step 1: Synthesis of p-SiO_2 spheres as structure matrix; Step 2: Impregnation of the Sn precursor; Step 3: Reduction of the Sn precursor inside the SiO_2 matrix to obtain Sn NPs embedded into p-SiO_2.

Figure 2.1 XRD patterns of Sn NPs@p-SiO_2. P63

Sn NPs@p-SiO_2 (red) and p-SiO_2 (blue).

Figure 2.2 Morphology of as-synthesized p-SiO_2 spheres and Sn NPs@p-SiO_2. P65

TEM images of (a) as-synthesized p-SiO_2 spheres and (b) Sn NPs@p-SiO_2, (c) SAED pattern of Sn NPs@p-SiO_2, and (d) size histogram of Sn NPs in p-SiO_2.

Figure 2.3 XPS image of Sn NPs@p-SiO_2. P67

(a) wide scan, (b) and (d) narrow scan of Sn 3d at the particle surface and after Ar etching to a depth up to 210 nm, respectively, and (c) depth profile for the Sn 3d region.

Figure 2.4 XPS composition depth profile of Sn@p-SiO_2. P68

Composition depth profile: (a) Si and Sn, (b) Sn and SnO_2.

Figure 2.5 TG-DTA results of the annealing of the Sn precursor loaded p-SiO_2 under 3% H_2/N_2 gas flow. P71

The mass percentage at 25°C was set as 100%.

Figure 2.6 XRD results of products at different reduction temperatures. P73

Figure 2.7 TEM images of products obtained at different reduction temperatures. P76

(a) 260°C, (b) 330°C, (c) 360°C, (d) 400°C, (e) 460°C, and (f) 600°C. All inset scale bars indicate 100 nm.

Figure 2.8 Morphology of calcined p-SiO_2 and the products obtained by loading the Sn precursor into calcined p-SiO_2 spheres followed by reduction using 3% H_2/N_2 gas for 6 h. P77

(a) TEM image of calcined p-SiO_2, (b, c) TEM images of the products obtained by loading the Sn precursor into calcined p-SiO_2 spheres followed by reduction using 3% H_2/N_2 gas for 6 h, and (d) SAED pattern of the black NP shown in the orange rectangle in (b), which was assigned to metallic Sn.

Figure 2.9 Illustration of the formation mechanism of Sn NPs@p-SiO_2. P78

(a) $Sn_{21}Cl_{16}(OH)_{14}O_6$ and other amorphous Sn precursors were absorbed into p-SiO_2 spheres after the impregnation of the $SnCl_2$ precursor; (b) amorphous Sn precursor was formed after annealing at a temperature below 260°C; (c) crystal Sn oxides, SnO_x where x = 1, 2, formed at ca. 330°C with the change in the pore structure of the p-SiO_2 spheres; (d) SnO_x were reduced and Sn NPs formed inside the p-SiO_2 spheres with the ability to further expand the pore inside the p-SiO_2 spheres.

Figure 2.10 Thermal properties of Sn NPs@p-SiO_2. P81

(a) DSC results of 100 melt-freeze cycles for Sn NPs@p-SiO_2. (b) The enthalpy of melting vs cycle number. (c) Example of the DSC curve for the 5^{th} cycle in the 220 – 245°C range for calculating the enthalpy of melting. (d) Melting temperature of Sn NPs confined into p-SiO_2 (blue empty circles) at each cycle compared to the melting temperature of bulk Sn (red dashed line).

Figure 2.11 Morphology of Sn NPs@p-SiO_2 after 20 melt-freeze cycles$_2$. P82

(a) TEM image of Sn NPs@p-SiO_2 after 20 melt-freeze cycles and (b) particle size distribution of Sn NPs embedded in p-SiO_2 shown in (a).

Scheme 3.1 Synthesis process of Sn@Al_2O_3 spheres. P92

Step 1: Synthesis of SnO_2 spheres through hydrothermal method; Step 2: Boehmite treatment and calcination in the air; Step 3: Reduction of the Sn precursor SnO_2@Al_2O_3 to obtain Sn@Al_2O_3.

Figure 3.1 Morphology of as-synthesized Sn@Al_2O_3 spheres. P96

TEM (a) and SEM (b) images of Sn@Al_2O_3 particles. SAED patterns of black cores inside shell of Sn@Al_2O_3 (c) and shell with light contrast (d). (e) XRD pattern of as-prepared Sn@Al_2O_3 particle powder.

Figure 3.2 Morphology of the intermediate SnO_2@Al_2O_3. P103

(a) TEM and (c) SEM image of SnO_2 spheres after boehmite treatment and calcination (SnO_2@Al_2O_3). (b) SAED pattern of the shatter at the surface of SnO_2

spheres (area shown in the red circle in (a)). Cross-section SEM images of (d) SnO_2@Al_2O_3 spheres, (e) SnO_2 spheres and (f) Sn@Al_2O_3 sphere. (g) XRD patterns of the as obtained SnO_2@Al_2O_3 (red curve) and SnO_2 sphere after calcined in the air (green).

Figure 3.3 XPS investigation of SnO_2@Al_2O_3. P104

(a) XPS wide scan of as synthesized SnO_2@Al_2O_3. (b) XPS narrow scan of as synthesized SnO_2@Al_2O_3 on Al 2p which can be deconvoluted into two components. Narrow scan on (c) Al 2p and (d) Sn 3d after Ar etching with different etching depths.

Figure 3.4 Size tunable SnO_2@Al_2O_3 and Sn@Al_2O_3. P105

TEM images of (e-h) Sn@Al_2O_3 with different morphologies (e: Sn@Al_2O_3-1600, f: Sn@Al_2O_3-600, g: Sn@Al_2O_3-350, h: Sn@Al_2O_3-60) reduced from corresponding (a-d) SnO_2@Al_2O_3 (a: SnO_2@Al_2O_3-1600, b: SnO_2@Al_2O_3-600, c: SnO_2@Al_2O_3-350, h: SnO_2@Al_2O_3-60) prepared using SnO_2 with various sizes, i.e. (a) ~1.6 μm, (b) ~600 nm, (c) ~350 nm; (d) ~60 nm. (i-l) The corresponding scheme for the formation of Sn@Al_2O_3. All scale bars are 500 nm.

Figure 3.5 Thermal Stability of Sn@Al_2O_3. P110

(a) Relative melting enthalpy in 100 melt-freeze cycles of Sn@Al_2O_3-1600 compared with bulk Sn ($\Delta H/\Delta H_0$) during melt-freeze cycles (red spheres) where ΔH and ΔH_0 are enthalpy of melting of Sn@Al_2O_3-1600 and that of bulk Sn respectively. Relative melting enthalpy of Sn@Al_2O_3-60 and Sn NPs@p-SiO_2 are labeled with green and blue spheres respectively. (b) Onset temperature (T_{onset}), peak temperature (T_{peak}), offset temperature (T_{offset}) of the endothermic peak for each melt-freeze cycle in air atmosphere in a DSC machine. (c) XRD patterns of Sn@Al_2O_3-1600 before and after 100 melt-freeze cycles in the air.

Figure 3.6 Morphology comparison of Sn@Al_2O_3-1600 before and after cyclic test. P111

Morphology comparison of Sn@Al_2O_3-1600 in TEM and SEM images before (a, b) and after (d, e) 100 melt-freeze cycles in the air. (c, f) The SEM images of commercial Sn powder before and after melt-freeze cycles in the same condition. The scale bar in (a, d) is 500 nm, in (b, e) is 1 μm and that in (c, f) is 20 μm.

Figure 3.7 Supercooling of Sn@Al_2O_3. P112

DSC curves for melt-freeze cycle of (a) Sn@Al_2O_3-1600, (b) commercial Sn powder, showing the existence of supercooling. (a1) and (a2) are the enlarged areas shown by red squares in (a).

Figure 4.1 Morphology of Sn@SiO_2 before and after heating in TEM. P127

(a, b) TEM image of Sn@SiO_2 samples, with two different Sn core sizes (a: 20 nm, b: 30 nm) and shell thicknesses (a: 20 nm, b: 8 nm), which are loaded on a tungsten wire inside a heating holder observed in vacuum at room temperature (25°C), respectively. (c) The SAED pattern of Sn@SiO_2 shown in (a). TEM images of Sn@SiO_2 after heating from room temperature (25°C) to 300°C in vacuum performed in a high-voltage TEM operated in 1000 kV in (d, e) strong electron beam condition (37.3 pA·cm^{-2}) and (f) weak beam condition (2.7 pA·cm^{-2}), inset: SAED pattern shows as-formed SnO_2. All scale bars are 100 nm.

Figure 4.2 *In situ* observation of Sn@SiO_2 at 300°C in vacuum at strong electron beam condition (37.3 pA·cm^{-2}). P129

(a) Random motion and gradual decrease in size of Sn droplets that embed inside SiO_2 shell indicate the possible diffusion of Sn at an elevated temperature (300°C). The blue arrows show the moving direction of Sn droplets according to the movie. Deformation of SiO_2 shell structure occurred during observation: (b) breakage of connected SiO_2 shell of two Sn@SiO_2 core-shell particles and (c) connection of two individual particles are shown (marked with green arrows).

Figure 4.3 In-situ observation of the disappearance of single liquid-state Sn core. P132

In situ observation of the disappearance of single liquid-state Sn core in (a) strong electron beam condition (37.3 pA·cm^{-2}) (mode I: balloon-like liquid-state Sn layer forms and decreases in thickness due the outward diffusion of Sn into the outside SiO_2 structure, and disappears in seconds) and (b) weak electron beam condition (2.7 pA·cm^{-2}) (mode II: the remained Sn core slowly decreases in size due to the diffusion of Sn, and gradually disappears) at 300°C in vacuum, respectively. The blue solid line in (a) and (b) show the outline of remained Sn core during diffusion process. The position of SiO_2 shell in (b) is outlined by a blue dash line. Schematics of two different diffusion modes: (c) mode I and (d) mode II, illustrating the diffusion process that shown in (a) and (b). In (c) and (d), the outline of remained Sn core and the thickness of liquid Sn layer are marked by orange dash lines and green dash lines, respectively. The white arrows are used for showing diffusion directions (white crosses "x" represent the arrow directed into the page).

Figure 4.4 Ostwald ripening in SiO_2 structure. P136

(a) Disappearance and growth of ultra-small Sn nanodroplets formed after disappearance of Sn cores during in-situ TEM observation (strong electron beam condition, 37.3 pA·cm^{-2}) at 300°C in vacuum. The change in shape and size of the blue dash line triangle with vertices a, b and c located at the positions of three typical particles (t_0) indicates the shrinkage of SiO_2 structure during the observation. (b) Increase in mean diameter and (c) decrease in number of ultra-small Sn nanodroplets in the observation field throughout the time. The dash lines in (b) and (c) show the increase and decrease tendency, respectively.

Figure 4.5 Formation of yolk-shell and hollow NPs from Sn@SiO_2 with different shell thicknesses but same Sn core. P137

TEM images of (a) Sn nanoparticles used as the cores of Sn@SiO_2 core-shell nanoparticles and Sn@SiO_2 core-shell nanoparticles with the shell thickness of (b) 3.0 nm, (c) 6.8 nm and (d) 29.0 nm, respectively. (e) Size histogram of Sn nanoparticles and Sn@SiO_2 shown in (a-d). (f-k) TEM images of Sn@SiO_2 core-shell nanoparticles,

with various shell thickness ((f, i): 3.0 nm, (g, j): 6.8 nm, (h, k): 29.0 nm), after loading in a sealed Al pan and heating from 25°C to 300°C at a ramping rate of 10°C/min in a DSC. Scale bars for (a-d) are 20 nm, for (f-h) are 50 nm, and for (i-k) are 100 nm.

Figure 4.6 Formation of yolk-shell and hollow NPs from Sn@SiO_2 with the same thicknesses but different sizes of Sn core. P140

(a) After heating in a DSC (loaded in a sealed Al pan and heated from 25°C to 300°C at a ramping rate of 10°C/min), the Sn@SiO_2 core-shell nanoparticles are transformed into yolk-shell (1-15) and hollow nanoparticles (16), showing a gradual evolution from core-shell to yolk-shell and finally hollow nanoparticles. Sn@SiO_2 core-shell nanoparticles with the same shell thickness (29.0 nm) but various core diameters (shown in a-2 as "d") (20~59 nm) are used as starting materials. Scale bar is 40 nm. (b) Volume ratio between remained Sn core and the original Sn core obtained by measuring more than 200 particles with various diameters from 13.3 to 59.7 nm. The increasing ratio of remained Sn core with bigger original core diameter indicate that Sn@SiO_2 NPs with bigger Sn cores will keep more Sn remained after heating, showing controllable Sn diffusion based on size difference (c) Histogram of volume ratios between as-formed void and shell which is close to Gaussian distribution. The mean value of this ratio is 2.74 ± 0.58, indicating a possible containing capacity of SiO_2 structure for Sn.

Figure 4.7. Element distribution of as obtained hollow NPs. P142

(a) HAADF-STEM image and (b) EDS element mapping images of as-formed hollow structure in ex-situ TEM observation, showing the distribution of Sn, Si and O, respectively. (c) The XPS wide scan of Sn@SiO_2 core-shell nanoparticles before and after heating.

Abbreviations

CPU: Central processing unit

CHS: Chemical heat storage

CENG: Compressed expanded natural graphite

CSP: Concentrated solar power plant

CTAB: Hexadecyltrimethylammonium bromide

DSC: Differential scanning calorimeter

DIBAH: Diisobutylaluminium hydride

EDS: Energy dispersive spectroscopy

FFT: Fast Fourier transform

FIB-SEM: Focused ion beam scanning electron microscopy

HTF: Heat transfer fluid

HAADF-STEM: High-angle annular dark-field scanning transmission electron microscopy

HRTEM: High-resolution transmission electron microscopy

IEA: International Energy Agency

LHS: Latent heat storage

NPs: Nanoparticles

PCMs: Phase change materials

PEG: Polyethylene glycol

PI: Polyimide

PAO: Poly-α-olefin

SEM: Scanning electron microscopy

SAED: Selected area electron diffraction pattern

SHS: Sensible heat storage

SCA: Silane coupling agent

TEOS: Tetraethyl orthosilicate

TES: Thermal energy storage

TH66: Therminol 66

TGA: Thermogravimetric analysis

TG-DTA: Thermogravimetric differential thermal analysis

TEM: Transmission electron microscope

UF: Urea-formaldehyde

XRD: X-ray diffraction

XRF: X-ray fluorescence spectrometry

XPS: X-ray photoelectron spectroscopy

Chapter 1.
General Introduction

1.1 Thermal Energy Storage

When we see back to the history of humankind, the discovery of fire helped our ancestors end up with living the life of savages, thus start the fast development beyond the natural evolution, making us the dominant species in the earth and creating the fantastic civilizations. Using fire for cooking is one of the earliest applications for us to utilize thermal energy, in which the chemical energy contained in the wood is transformed to thermal energy by combustion, then transfer to food that behaves as the heating process, thus resulting the rise in temperature of the meat and rice.

Thermal energy participated in the evolution of natural species before the existence of human beings. The major source of thermal energy is solar radiation which helps to create the suitable biosphere for all the creatures on the earth, thus naturally makes them become dependent on the suitable living temperature. As for humans, until April 2019, the total number of the currently living humans was estimated to have reached 7.7 billion. This rapid growth of population results in the drastic demands in energy in the form like electricity, heat and mechanical work, which can be produced from the energy conversion of various types of resources, including fuel source, hydropower, nuclear power and emerging renewable energy resources like solar radiation, biomass, wind power, tide power, geothermal power, etc.

According to the International Energy Agency (IEA), the world power generation in 2016 was 24.973 TWh, in which the power from coal and natural gas occupied 38.4% and 23.2%, respectively, of total power generation. [1] According to this data, the dominant energy generation comes from burning fossil fuels, which has resulted in massive emissions of greenhouse gases like CO_2, thus contributing to the global warming. In consequence, it has been reported that melting of ice sheet in polar region, like Greenland, at an increasing rate are happening, potentially causing the global sea-level rise. [2, 3] On the other prospective, due to the limited reserves and non-renewable characteristics of fossil fuels, it is at risk for depending on the fossil fuel too much, learned from the lessons given by the energy crisis in 1970s.

Here, renewable energy resources refer to the resources which can be "renewed" in a human timescale like what as mentioned above. Among these renewable energies, the solar thermal power can be directly collected as thermal energy for further utilizations in a concentrated solar power plant (CSP), which is shown in Figure 1.1. However, the biggest problem lies in solar energy is the fluctuant availability based on time and space. On the one hand, big mismatch occurs between the peak hours of energy demand and consumption, for example, there is a big demand for air condition in a summer night in tropic area while no solar energy available after sunset. On the other hand, due to the geographical and climate issues, the distribution of solar energy varies across the planet. For example, the solar resource in Sahara Desert is much more abundant than that in Hokkaido island due to the difference in latitude, and much more abundant than that in Yangtze Plain with the same latitude due to the difference in

climate. In addition, the currently designed large-scale solar thermal power plants are set in the remote area while the densest consumption of energy is from urban area with a large number of populations. This time-space mismatch of demand and supply in solar thermal energy limits its utilization.

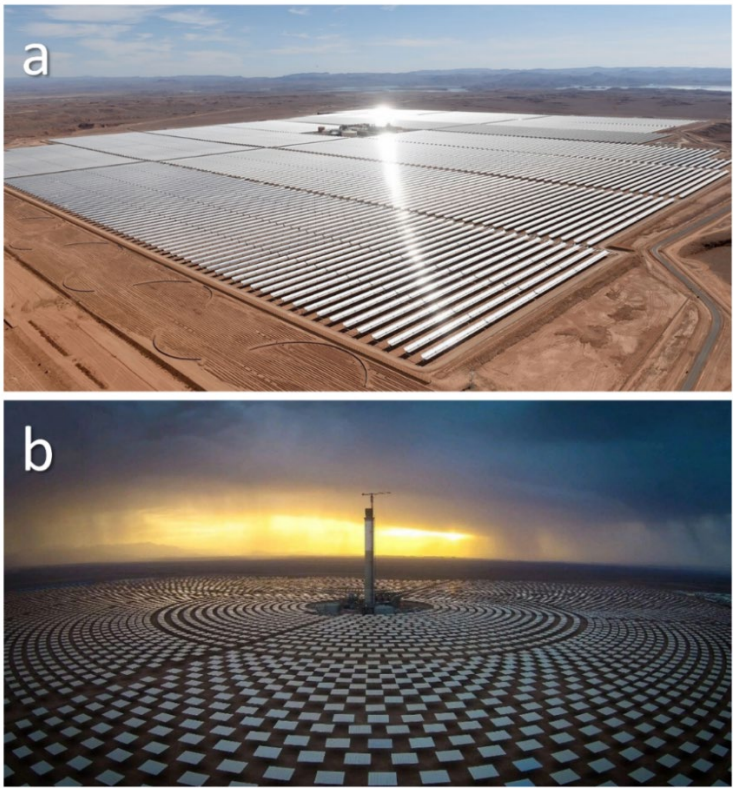

Figure 1.1 Solar thermal power plants in Morocco.

(a) Noor 1: a parabolic-trough type CSP plant made up of 500,000 arched mirrors, each about 40 feet off the ground; (b) Noor 3: a tower type CSP plant (in construction). [4, 5]

Thermal energy with high quality if not consumed, simply dissipates into the environment resulting in the degradation in quality, thus causing wastage. Based on the

Carnot's theory, the efficiency of a heat engine (Carnot's efficiency) is the theoretical or maximum fraction of the heat input at high temperature converted to work which can be calculated as:

$$\eta(\%) = 1 - \frac{T_{cold}}{T_{hot}} \times 100\%$$

where T_{cold} and T_{hot} refer to the temperatures at which the high temperature reservoir and cold temperature operate in a heat engine (K), respectively. According to equation 1, when the thermal energy dissipates into the environment, it means that the maximum T_{hot} are decreasing to the environment temperature T_{cold}, thus resulting in the decrease of Carnot efficiency η (%). That is to say, thermal energy that dissipates into environment will be no more useful for conversion to work. Not only for CSP plants, huge amount high-quality thermal energy is generating in our daily life, like industrial waste heat, heat from nuclear power plants, etc. Therefore, thermal energy storage (TES) is a good way for eliminating the mismatch between demand and production of energy.

Not only for storage, the proper management of thermal energy is another big issue in modern society. To take mobile phone as an example, heat dissipation is a problem that must be overcome for the safe operation of mobile phones. Also, good thermal management can prevent damage to the battery of the mobile phone, increase battery life, reduce the damage to the high central processing unit (CPU) from high temperature, and improve the comfort of use. Since the birth of first mobile phone, it kept being developed towards more compact and lighter device. With the development of the information and communications technology, the challenges of mobile phone

cooling are more severe, especially in the new 5G (5th generation wireless systems) era.

In general, the changes in cooling requirements of 5G mobile phones mainly come from two aspects: increase in power consumption and changes in mobile phone structure. In terms of power consumption, the 5G mobile phone will possess a more powerful processor and the data processing capability will be higher than that of the 4G mobile phone. As a result, the absolute value of the produced heat will increase sharply, giving great challenge to heat dissipation of devices. Besides, the structure changes of the mobile phone put forward higher requirements on the heat dissipation performance. As the number of 5G antennas increases and the penetration of electromagnetic waves becomes weaker, the material of the mobile phone body turns toward non-metallic, which requires an additional heat dissipation design. In addition, with the progress in chip manufacturing, the mobile phone has become more and more compact, this also increases the difficulty of thermal management. Therefore, due to feature of PCMs that latent heat can be stored at a constant temperature, suitable PCMs can be used as heat sinks that can absorb the heat produced from chips.

1.1.1 Classification of Thermal Energy Storage

In general, thermal energy storage can be achieved by sensible heat storage, latent heat storage, and chemical heat storage. [6] Sensible heat storage (SHS) is achieved by raising temperature of a liquid or solid, like water, thermal oils, molten salts, concrete blocks, etc. through conventional heat transfer, like radiation, conduction and

convection. The amount of stored thermal energy (sensible heat) is determined by the temperature change, mass and specific heat capacity (C_p) of the storage medium, which can be expressed as

$$Q = \int_{T_i}^{T_f} mC_p \, dT$$

where Q is the thermal energy stored (J), m is the mass (kg), C_p is the specific heat capacity ($J \cdot kg^{-1} \cdot K^{-1}$) and T_i and T_f are the initial and final temperature during heat charging process (K), respectively. When releasing thermal energy, the temperature of SHS materials decreases. Materials for SHS should be thermally stable within working temperature range, low cost (except for some special applications, like liquid metals, etc.) and low toxic. As an intrinsic characteristic of SHS, the temperature change during heat charge and discharge processes puts a big limitation for the applications. Also, compared to other techniques, SHS performs relatively low thermal energy storage density within a narrow temperature range, making the system hard to be compact in temperature-sensible conditions.

Latent heat storage (LHS) realizes the high-density thermal energy storage by absorbing energy at a constant temperature, which is used for contributing to the phase change of the thermal energy storage medium. Based on the type of phase change, LHS can be divided into solid-solid LHS and liquid-solid LHS. Due to the phase change characteristic, latent heat storage materials are also called phase change materials (PCMs), which will be introduced in the next part.

Chemical heat storage (CHS) uses reversible chemical reactions to achieve high-density thermal energy storage. [7] During charge and discharge process, the energy stored and released by breaking and forming chemical bonds. Thanks to the reversibility of designed chemical reactions, the stored heat can be released controllably through the chemical reactions. In general, the chemical reactions for CHS should have moderate reaction temperature and good reversibility without side reactions. In addition, materials for CHS should be non-toxic, non-corrosive, non-flammable, non-explosive and stable during the storage and transportation. Compared to other TES methods, CHS exhibits the highest energy storage density and good durability for transportation and long-time storage. Take MgH_2/Mg system as an example, this CHS system uses the reversible reaction below:

$$\mathrm{MgH_2} + \Delta H_r \leftrightarrow 3\mathrm{Mg} + \mathrm{H_2}$$

where ΔH_r refers to the thermal energy stored by conducting the reaction.

Nevertheless, main drawbacks of CHS lies in the chemical reactions involved. For MgH_2/Mg system, due to the necessity of H_2 storage and slow reaction kinetics, strict reaction conditions are required. Meanwhile, operating pressure should be controlled (50-100 bar). In addition, the sintering of Mg is also a big problem for this CHS system. [8] All these limitations make CHS methods a long way to practical applications.

1.2 Phase Change Materials

Phase change or phase transition, as one of the most common phenomena that occurs every second in our planet, was used to describe transitions between solid, liquid, gaseous states as well as plasma of matters. For example, the melting of the ice and the evaporation of water are the typical solid-liquid phase change and liquid-gas phase change, respectively. Also, the martensitic transformation, as a typical solid-solid phase transition, is important for the heat treatment of steel and the formation of shape memory alloys. When we come to the concept of "phase change materials", literally, they are recognized as the materials that use phase change to achieve certain designed functions, such as thermal energy storage (TES), data memory, etc.

Thermal energy that stored in PCMs system within a certain temperature range can be divided into two parts: sensible heat and latent heat. Sensible heat comes from the raise in temperature of the matter, which is the function of the temperature change, the mass, and the specific heat of the matter. Latent heat comes from the phase change process, which determines the storing or releasing of the thermal energy. The thermal energy storage process in PCMs is shown in Figure 1.2 (the C_p here is considered as a constant to the temperature). The TES capacity of the PCMs was given by:

$$Q = \int_{T_i}^{T_m} mC_p\, dT + ma_m \Delta H_m + \int_{T_m}^{T_f} mC_p\, dT$$

where Q – quantity of heat stored (J), T_i – initial temperature (°C), T_f – final temperature (°C), T_m – melting temperature (°C), m – mass of PCMs (kg), C_p – specific heat (J/kg·K), a_m – fraction of melted PCMs, ΔH – melting enthalpy (J/kg).

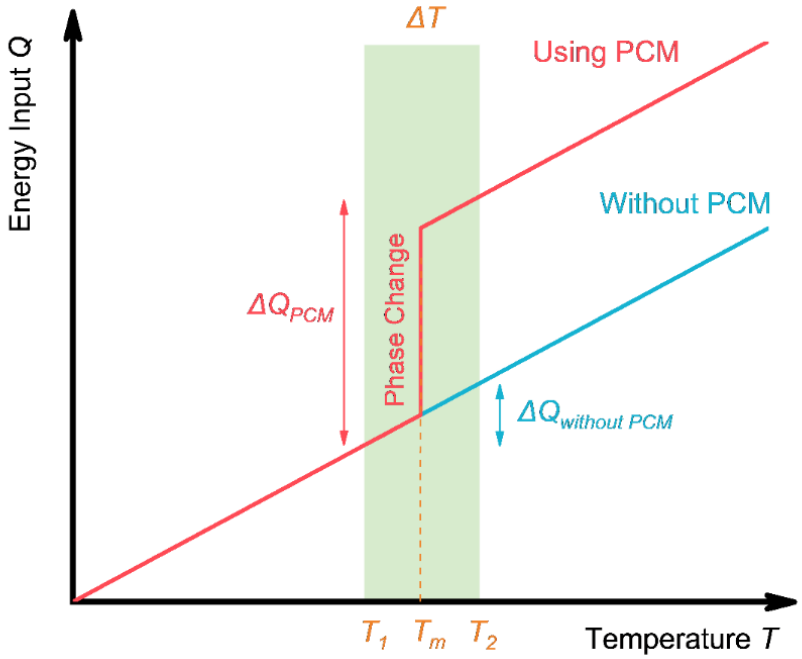

Figure 1.2 Process of thermal energy storage in PCMs.

In solid-liquid PCMs, thermal energy is stored without increasing the temperature of the system at the melting temperature (T_m). During a certain range of temperature (ΔT, shown as green area), the thermal energy storage capacity of PCM is much higher than that of sensible heat storage materials.

1.2.1 Selection Criteria of PCMs

The ideal PCM for a certain application should possess the desired thermal, physical, kinetic and chemical properties to meet the demand of specific situation. [9]

1.2.1.1 Thermal Properties

Generally, PCMs should exhibit high latent heat per volume or weight based on different applications. For example, for a steady TES system in CSP or waste heat recovery system, high latent heat per volume is important since the compact storage

unit is needed for lower cost. When the PCM is used in some occasions that light-weight system should be considered, high latent heat per weight is expected. The chosen PCM should have a phase change temperature which is well matched to the desired operating temperature in TES system. This can help the system run with high efficiency. Generally, the latent heat stored in solid-liquid phase change process is closely linked to the melting temperature. During solid-liquid phase change process, the pressure is constant. The change in molar entropy of the system (ΔS) is

$$\Delta S = \frac{\Delta H_{\mathrm{m}}}{T_{\mathrm{m}}}$$

where ΔH_{m} is the fusion enthalpy and T_{m} is melting temperature. The entropy of a solid increases when it melts to a liquid, due to the further dispersal of energy and matter. Therefore ΔS here is positive. Thus the ΔH_{m} will increase with the T_{m}.

Meanwhile, a high specific heat of PCM is also expected, so that to provide not only high LHS but also more significant additional SHS in the same temperature difference. Importantly, PCMs for TES are always expected to have a higher thermal conductivity which enable fast heat storage and release and can reduce the heat exchange surface.

1.2.1.2 Physical Properties

For PCM, volume change during phase change process should be as small as possible. A big volume expansion may permanently damage the PCM container and heat exchanger. Gaps and voids may also be dispersed in the PCMs, thus decreases thermal conductivity. Meanwhile, to avoid the evaporation and deterioration of PCM,

a low vapor pressure at the operating temperature is required. For long-term cyclic operation (charge and discharge), the phase change process should be completely reversible, and congruent melting is preferred. In addition, the density of PCMs should be concerned, PCMs with higher density may possibly be considered possessing higher thermal energy storage density.

1.2.1.3 Kinetic Properties

The supercooling effect should be as small as possible. Supercooling of liquid is the phenomenon that when lowering the temperature below the freezing point, the liquid does not turn to solid. This temperature difference between melting and freezing delays the heat release, making thermal energy storage less efficient. For another, fast crystallization is preferred. A high nucleation rate can raise the dynamic response ability of the whole TES system. [9]

1.2.1.4 Chemical Properties

For safety concern, the selected PCM should be non-toxic, non-flammable and non-explosive. When cycling, especially in high temperature TES, there should be no chemical decomposition or side reactions between each component, so that to ensure the long-term stability of the system. Moreover, PCMs should be non-corrosive to the container or construction materials.

1.2.2 Classification of PCMs

Phase change processes are classified into solid-solid, solid-liquid, liquid-liquid, liquid-gas and solid-gas phase transition based on the different physical states of substance before and after phase transition. For thermal energy storage, generally, liquid-gas and solid-gas transition are excluded due to drastic volume change. Solid-solid PCMs (e.g., polyalcohols, [10] polyurethanes, [11] etc.) generally show small latent heat of phase transition, which are limited in applications but worth developing due to the small volume change during phase change process.

Until now, solid-liquid PCMs are the most studied and used storage medium of thermal energy. In this part, various types of solid-liquid PCMs (refer to as "PCMs" below), from organic compound to inorganic salts, will be introduced.

1.2.2.1 Organics

Organic PCMs, including paraffins (alkanes), fatty acids, esters and other organic compounds, are widely studied in the past decades. [12]

Paraffins is a historical name of alkane which refer to saturated hydrocarbons with general chemical formula C_nH_{2n+2} with non-toxic and non-corrosive characteristics. As chemicals from petroleum, paraffins are distilled from cruel oil, often state as a mixture of several hydrocarbons. For TES applications, paraffins possess high latent heat storage capacities, which are determined by the molecular weight of paraffins with different carbon chains, in a relatively narrow temperature range. Generally, the longer average length of the carbon chains, the higher enthalpy of

fusion and phase change temperature the paraffins possess. The drawback of using paraffins as PCMs is their low thermal conductivity, which reduces the charge and discharge rate during thermal energy storage and release.

Fatty acids with chemical formula $CH_3(CH_2)_{2n}$-COOH are PCMs exhibit high latent heat, little supercooling and small phase change volume change, which are suitable for low temperature LHS. Like paraffins, fatty acid with longer carbon chains also shows higher phase change temperature and larger enthalpy of fusion. Moreover, the crystallization degree of fatty acid increases with its molar mass. Due to denser crystalline lattice formed by hydrogen bonding, consisted of carboxylic acid molecules with even number of carbon atoms, in particular, fatty acids with an even number of carbon atoms in molecule exhibit higher values of latent heat and phase change temperature than those with odd numbers of carbon atoms in molecules. For applications, fatty acids have some drawbacks. For example, fatty acids are more expensive than paraffins, corrosive to metal container and have unpleasant smell. These characteristics limited their applications.

Fatty acid esters are also PCM candidates for LHS, showing a solid–liquid phase transition in a narrow temperature range. In particular, mixture of fatty acid esters can form eutectics, which exhibit little or no supercooling. The formation of eutectics potentially expands the design for certain LHS applications.

Other organic compounds like polyethylene glycol (PEG) can also be used as PCMs. PEG possesses high melting enthalpy arrived form high crystallinity. Importantly, by controlling the molecular weight, the thermal properties of PEG can be

customized for TES applications (e.g., phase change temperature: ca. 4 to 70°C, enthalpy of fusion: 117–174 J/g). The increase of molecular weight leads the growth in phase change temperature and enthalpy of fusion.

1.2.2.2 Inorganics

Compared to organic compounds, inorganic substances, when used as PCMs, provide wider range of operating temperature in both low temperature and high temperature LHS. The intensely studied inorganic PCMs include salt hydrates, molten salts (and their eutectics), metals and alloys.

Salt hydrates are inorganic salts containing water of crystallization, like calcium chloride hexahydrate ($CaCl_2 \cdot 6H_2O$), manganese nitrate hexahydrate ($Mn(NO_3)_2 \cdot 6H_2O$), which possess high energy storage density, acceptable price, abundant reserve but low thermal conductivity (from ~0.6 to ~1.0 $W \cdot m^{-1} \cdot K^{-1}$). [13, 14] There is a big number of commercially available salt hydrates with congruently, semi-congruently or incongruently melting characteristics, in which congruently-melting salt hydrates are the most ideal ones for TES. [15] The phase change process that enable thermal energy storage and release is accompanied with the dehydration and hydration of the salts. [16] However, for a large number of salts hydrates, the biggest problem is incongruent melting. Incongruent melting means the salts are not able to dissolve in the water from dehydration at the melting temperature. This phenomenon causes serious problems like sedimentation and phase separation in practical applications. In addition, due to their poor nucleation abilities, supercooling also limits the applications of salt

hydrates. So far, much work has been done for overcoming these drawbacks. [16-18] Due to the abundant reserve and low cost, salt hydrates are still suitable PCMs for TES applications despite the drawbacks they have.

Except for salt hydrates, molten salts are also suitable PCMs with a wide operating temperature range (from ~100 to ~1000°C) in TES system. [19] Due to their high thermal energy storage density, abundant reserves and low price, molten salts have could be used as storage medium in different applications including thermal storage system in concentrated solar power plants. [20] The main drawbacks of molten salts for LHS are low thermal conductivity (below 1.0 $W \cdot m^{-1} \cdot K^{-1}$), high volume expansion ratio during phase transition and they are corrosive to the metallic container. [21-23]

Metals and alloys with high melting temperature (> 300°C) are usually used as PCMs in high temperature LHS system. The superior thermal conductivity is the biggest advantage of using metal alloys for TES, which eliminate the need for large surface of heat exchange. Moreover, their thermal energy storage densities are larger than molten salts due to the high density of metals and their alloys, and the good cycling stability makes them suitable in long time operation [24, 25]. Meanwhile, the volume expansion of metals during phase transition is low. Among the high temperature metallic PCMs, binary and ternary alloys with main compositions of elements Al, Cu, Mg and Zn, like Al-Si, Al–Si–Mg, Al–Si–Cu and Al–Mg–Zn alloys, exhibit the highest enthalpy of fusion based on the same volume [25, 26]. In previous research, metallic PCMs with high phase change temperature have been proposed for applications in solar power generation systems. [27, 28] However, in high temperature, metals can be highly corrosive

to the metallic container. Therefore, the encapsulation of metallic PCMs or the container should be considered.[23]

1.3 Low Melting Point Metals for PCMs

Like metals and alloys with high melting temperature as mentioned above, the low melting point metals we mentioned here refer to the metals and alloys that are easily meltable below 300°C. The physical properties of low melting point metals and alloys with various compositions are listed in Table 1.1. [7, 29-32]

Table 1.1 Physical properties of low melting point metals and alloys.

Metals	T_m °C	T_b °C	$C_{p,l}$ kJ·kg^{-1}·K^{-1}	ρ kg·m^{-3}	λ_l W·m^{-1}·K^{-1}	ΔH_m kJ·kg^{-1}	TES density MJ·m^{-3}	Ref.
$Ga_{73.5}In_{15.4}Sn_{11.1}$	10.6					69.03		29
$Ga_{78.4}In_{14.9}Sn_{6.7}$	10.9					71.2		29
$Ga_{83.5}In_{16.5}$	15					71.68		29
$Ga_{91.6}Sn_{8.4}$	19.8					78.29		29
$Ga_{95}Sn_{5}$	19.9					79.22		29
$Ga_{97.9}Al_{2.1}$	26.5					82.59		29
Cs	28.7	2023.8	0.236	1796	17.4	16.4	29.4544	7
Ga	29.8	2204.8	0.37	5907	29.4	80.12	473.26884	7
Rb	38.9	685.73	0.363	1470	29.3	25.74	37.8378	7
$Bi_{44.7}Pb_{22.6}In_{19.1}Sn_{8.3}Cd_{5.3}$	47		0.197	9160	15	36.8	337.088	7
$Bi_{35.5}In_{64.5}$	54.1					30.82		29
$Bi_{49}In_{21}Pb_{18}Sn_{12}$	58		0.201	9010	10	28.9	260.389	7
Cerrolow	58					90.9		30
$Bi_{38.7}Sn_{16.7}Pb_{14.4}In_{30.2}$	58.3					28.98		29
$Bi_{32}In_{51.2}Sn_{16.8}$	60.8					25.4		31
Bi-Cd-In eutectic	61					25		30
$Bi_{41.8}In_{58.2}$	61.4					29.88		29
K	63.2	756.5	0.78	664	54	59.59	39.56776	7
$Bi_{50}Pb_{26.7}Sn_{13.3}Cd_{10}$	70		0.184	9580	18	39.8	381.284	7
Cerrobend	70					32.6		30
Bi–Pb–In eutectic	70					29		30
$Bi_{41.6}Sn_{19.4}Pb_{23.2}Cd_{15.8}$	71.7					24.51		29
Bi-In eutectic	72					25		30
$Bi_{21.8}In_{78.2}$	73.1					22.46		29

$Bi_{38.5}Sn_{22.2}Pb_{25.3}In_{14}$	75					25.36		29
$Bi_{40.5}Sn_{28.5}Pb_{16.3}In_{14.7}$	75.7					21.71		29
$Bi_{53.8}In_{27}Sn_{19.2}$	76.6					32.6		31
$Bi_{42.5}In_{35.2}Sn_{22.3}$	79.2					36.91		29
$Sn_{9.5}Bi_{56}Pb_{34.5}$	90.8		0.161			19.54		32
$Bi_{71.2}Pb_{28.8}$	94.9					28.99		29
$Bi_{52}Pb_{30}Sn_{18}$	96		0.167	9600	24	34.7	333.12	7
Bi–Pb–Sn eutectic	96							30
Na	97.8	881.4	1.38	926.9	86.9	113.2	104.95289	7
Bi–Pb	125							30
$Bi_{55}Pb_{43}Zn_2$	127		0.154			20.44		32
$Sn_{48}Bi_{50}Zn_2$	135		0.198			47.62		32
$Bi_{58}Sn_{42}$	138		0.201	8560	19	44.8	383.488	7
In	157	2023.8	0.23	7030	36.4	28.59	200.9877	7
$Sn_{73.5}Pb_{22}Zn_{4.5}$	172		0.247			59.8		32
Li	186	1342.3	4.389	515	41.3	433.8	223.3967	7
$Sn_{91}Zn_9$	199		0.272	7270	61	32.5	236.275	7
Sn	232	2622.8	0.221	730	59.6	60.5	44.165	7
Bi	271	1560	0.122	979	8.1	53.3	52.1807	7

T_m: melting temperature; T_b: boiling temperature; $C_{p,l}$: specific heat capacity (in liquid); ρ: density; λ_l: thermal conductivity (liquid); ΔH_m: melting enthalpy.

Generally, as metals, due to the contributions of electron motions, low melting point metals exhibit high thermal conductivity that much higher than any other PCMs. Also, the strong metallic bonding results in high enthalpy of fusion, combined with high density, giving a high thermal energy density. Low melting point metals are widely available with the elements like bismuth (Bi), gallium (Ga), tin (Sn), indium (In), zinc (Zn), cadmium (Cd), tellurium (Te), antimony (Sb), thallium (Tl), mercury (Hg) and lead (Pb). With the consideration of reserves, toxicity, physical and chemical properties, the commonly used elements are Sn, Bi, In and Ga.

In terms of TES, Sn can be applied in solar power plant for heat storage medium due to its relatively high phase change temperature among low melting point metals. Lai *et al.* demonstrated enhanced solar-thermal storage by utilization of the latent heat

of Sn/SiO_x core–shell nanoparticles (NPs) embedded in a eutectic salt. The heat capacity of HITEC solar salt was increased by 30%. [33]

Except for TES, low melting point metals that melt near room temperature are also suitable PCMs in the thermal comfort applications. To take gallium as example, gallium possesses a melting temperature about 29.8°C, which is close to ambient temperature and body temperature. The TES density at phase change temperature of gallium is about 473.27 $MJ \cdot m^{-3}$ which is much larger than the TES density (174.27 $MJ \cdot m^{-3}$) of paraffin (n-Nonadecane) with a similar phase change temperature of 32.0°C. [34] More importantly, gallium possesses a large thermal conductivity at about 29.28 $W \cdot m^{-1} \cdot K^{-1}$ in liquid state, which enable the sensitive temperature control. Moreover, gallium is low toxic, non-flammable, non-explosive and stable in cyclic energy storage and release with small volume expansion.

Conventional PCMs, like organic compounds, have been investigated for heat dissipation of electronic devices. However, due to the low thermal conductivity and small volumetric TES density at phase change temperature, organic compounds exhibit low efficiency in thermal management. Ge *et al.* studied using Gallium for keeping smartphone cool during operation. Their experiments demonstrated that 3.4 ml gallium would maintain the module below 45°C for 16 min at 2.832 W, in which the holding time for maintaining operation temperature was longer than most of the conventional PCMs. [35] Yang *et al.* developed a finned heat pipe assisted passive heat sink based on low melting point metal PCM for thermal buffering of thermal shock with heat generation rate up to 1000 W (10 $W \cdot cm^{-2}$), showing longer operation time (1.4–2.4

times) of high power electronics compared to the case of using conventional organic PCM. [36]

However, as a high performance PCM in thermal energy storage and management, the low melting point metals or alloys still in demand of efforts to be modified for practical applications. First, due to the corrosive characteristics of metals in liquid state, the compatibility between low melting point metal PCM and its container should be guaranteed. Kondo et al. performed the corrosion test of steels in liquid Ga, Sn and Sn-20Li at 873 K up to 750 h. They found the corrosion of these steels in liquid Ga, Sn and Sn–20Li alloy was caused by the formation of a reaction layer and the dissolution of the steel elements into the melts. [37] The bad compatibility between liquid metals and container, seriously limited their applications. Moreover, the sintering of liquid metal particles in low melting point metal PCMs may lead to the changes in as-designed structure or morphology during operation, deteriorating their sustainable usage in the form of nanofluids or slurry.[38] Therefore, the encapsulation in marco, micro or nano scale of low melting point metals is one way to improve their utility.

1.4 Micro/Nano Encapsulation of PCMs

Compared to their bulk counterpart, PCMs in micro or nano size possess much larger surface area which great expands the heat transfer interface during charge and discharge of thermal energy. For example, when comparing the surface area between two samples with the same weight and density, and in spherical shape with two diameters: 1 cm and 100 nm. It is easy to calculate but hard to image that the surface

area of later one is 100000 times larger than that of the former one. Meanwhile, micro/nano-size PCMs are easier to be surface-modified and dispersed in heat transfer fluid (HTF), which greatly explore the wider applications of PCMs.

Despite the suitability of PCMs in many thermal applications, the practical use of all types of solid-liquid PCMs is still limited by several problems. PCMs in liquid state are facing the common problem of leakage during the heat storage process due to the flowability of liquids. The leakage of PCMs will the decrease the TES capacity thus deteriorate the cyclic stability. In particular, when using metals and molten salts as PCMs, corrosion may happen on the key parts of the devices or facilities, reducing the service life or even causing safety problems.

One solution to these issues is to encapsulate PCMs in micro or nano scale, which is also called microencapsulation or nanoencapsulation. The encapsulated PCMs are called micro-encapsulated PCMs (MEPCMs) or nano-encapsulated PCMs (NEPCMs), depending on the dimensions of PCMs (MEPCMs: 0.1–1000 μm; NEPCMs: 1–100 nm). Encapsulation means a process of embedding the PCM as cores (can be single-core or muti-core) into protection structure which can be a shell or layer, and also can be porous structure, thus isolates and protects them from the external environment. By micro/nano encapsulation, PCMs can be transformed to powder or paste form, and the volume expansion of PCMs can be eliminated. So far, much work has been focused on the preparation of MEPCMs and NEPCMs. [39-43] The materials for encapsulation (encapsulant) vary from organics (like polystyrene, urea formaldehyde, polymethyl methacrylate, etc.) to inorganics (like calcium carbonate, silica, sodium

silicate, metal oxides, etc.). [44] Herein, typical preparation methods of MEPCMs and NEPCMs are listed below. [45]

1.4.1 Approaches for Micro/Nano Encapsulation of PCMs

There are many approaches for achieving the micro and nano scale encapsulation of PCMs, which are suitable in different occasions and can be classified into three main categories: polymerization methods (sometimes also named as "chemical methods"), physico-chemical methods and physical methods.

1.4.1.1 Polymerization Methods

Emulsion polymerization. In emulsion polymerization, one phase with monomer is uniformly dispersed in the continuous phase with addition of surfactant, emulsifier under mechanical stirring condition to form the emulsion. The encapsulation shell is then grown on the surface of the PCM core. The droplet size of emulsion is at the range of 1–10 mm. The size of emulsion droplets can be further decreased to nanoscale (20–200 nm) by inputting higher external energy, which is also called miniemulsion. The microemulsion (droplets size range: 10–100 nm) can form by adding large amount of surfactant to overcome the interfacial energy, which has good thermodynamic stability. [46, 47]

Interfacial polymerization. In interfacial polymerization, the first reactive monomer in one phase is dispersed into an immiscible phase which contains a second monomer. The monomers react at the interface, forming a polymeric membrane for

encapsulation. [48] Usually, the interfacial polymerization has been used in production of MEPCMs. [49]

In situ polymerization. In *in situ* polymerization, two immiscible phases containing organic intermediates that will react with each other for polymeric encapsulation. [50] Compared to the interfacial polymerization, there are no reactants in the core material in *in situ* polymerization and all polymerization reactions occur in the continuous phase. [42] In addition, through *in situ* polymerization, particles with the size ranging between 5 and 100 μm can be obtained. [50]

1.4.1.2 Physico-Chemical Methods

Coacervation. In coacervation process, liquid–liquid phase separation (bottom: polymer-rich dense phase; top: transparent solution) of a homogeneous solution of charged macromolecules is induced by adding of natural salt or alcohol. [51-56]

Sol–gel encapsulation. Sol-gel method for encapsulation of PCMs often starts in suspension of PCM nanoparticles or microparticles in aqueous solution. The formation of the encapsulating shell (hydrated metal or semi-metal oxide like TiO_2, SiO_2, etc.) is induced by hydrolyzing shell precursors so that to produce soluble hydroxylated monomers, followed by polymerization and phase separation (e.g., SiO_2, TiO_2, etc.). [57]

Self-assembly method. Self-assembly method is sometimes also called “one-step method”. In the case of using this method for encapsulating PCMs, system components like molecules, polymers, colloids, or macroscopic particles are organized

into shell or other confinement structure which are the results of local interactions among these components, without external direction. [58-60]

Solvent evaporation. The encapsulation of PCMs by solvent evaporation generally consists four steps: (1) dissolution of the hydrophobic PCM in an organic solvent containing the coating polymer; (2) emulsification of the organic phase that contain PCM in a continuous aqueous phase; (3) extraction of the solvent from the organic phase that contains PCM by the continuous aqueous phase, with removing the solvent by evaporation, transforming the droplets into solid PCM particles with polymer encapsulation; (4) Removal of the residual solvent. [44, 61]

Supercritical CO_2-assisted methods. The easily accessible critical conditions of CO_2 are 73.8 bar and 31.1°C which is close to ambient temperatures. The non-toxic, non-flammable, gas-like viscosity, liquid-like density with enhanced solubility broaden their applications. The role of supercritical CO_2 for encapsulation can be a solvent, antisolvent, solute, drying medium, and foaming agent. [49, 62]

1.4.1.3 Physical Methods

Physical methods for encapsulation of PCMs are generally used in large-scale, industrial production. Although, these techniques are not capable of producing microcapsules smaller than 100 μm due to their inherent characteristics, they are still suitable for the mass production of MEPCMs. [49] Here, typical physical techniques are listed below: [44, 63-65]

- Spray-drying

- Fluid Bed Coating
- Electrostatic encapsulation

1.4.2 Micro/Nano Encapsulation of Metals and Alloys

So far, a large number of works on the micro and nano encapsulation of organic compounds have been reported. (why metals and alloys are difficult to be encapsulated?) Herein, a few studies that focus on micro or nano encapsulation of low melting point metals/alloys and high melting point metals/alloys are briefly introduced.

1.4.2.1 Micro/Nano Encapsulation of Low Melting Point Metals and Alloys

Metal oxide or semi-metal oxide. In general, stable metal oxide or semi-metal oxide, like SiO_2, TiO_2 and Al_2O_3, were used for encapsulating low melting point metals nanoparticles and microparticles. Hong et al. [66] used emulsion method to prepare indium nanoparticles by boiling commercial indium powder in poly-α-olefin (PAO). The indium nanoparticles were collected by centrifugation and encapsulated with silica through a sol-gel method. The obtained silica-encapsulated indium nanoparticles were suspended into PAO, which was for enhancing the heat-transfer property of PAO in a potential high-temperature application. The SiO_2 shell not only prevented the leakage and agglomeration of liquid state indium, but also enhanced the dielectric properties of indium nanoparticles, expand the application in cooling of electronic devices. The viscosity of PAO that containing silica encapsulated indium nanoparticles at 45°C (9.49 cP) is close to the viscosity of PAO (4.68 cP). Their result shows that the PAO that

contains 30 at% indium nanoparticles exhibit a 1.6 times higher heat-transfer coefficient than that of original PAO.

Cingarapu *et al.* synthesized Sn nanoparticles with a modified polyol reduction method followed by sol–gel SiO_2 encapsulation on the surface ($Sn@SiO_2$). [67] The SiO_2 shell provided protections for the chemical and structural stability of Sn nanoparticles during the melt-freeze cyclic process. By dispersing $Sn@SiO_2$ core-shell phase change nanoparticles into a synthetic heat transfer fluid (HTF), Therminol 66 (TH66), at the volume ratio of Sn nanoparticles to 5 vol%, the enhanced thermal properties were achieved. As for the thermal conductivity of the nanofluid, an increase of ~13% was achieved when loading 5 vol% Sn nanoparticles, which agrees with Maxwell's effective medium theory. The volumetric thermal energy storage of the nanofluid increased by ~11% when cycled between. This increase was contributed by the latent heat during melting of Sn cores, therefore, the value of the increase could be further improved if thermal cycling is conducted in a narrower temperature range between 100°C and 270°C. Viscosity of the modified nanofluid was measured between 25°C and 125°C, revealing that the viscosity of nanofluid and base fluid are quite similar at 125°C. In addition, no changes were observed in $Sn@SiO_2$ (5 vol%) in nanofluid during 20 heat-cool cycles, showing a good thermal stability of the $Sn@SiO_2$. These experimental results showed the enhancement of Sn nanoparticles on both thermal conductivity and thermal energy storage density of the base HTFs, exhibiting the potential for CSP systems.

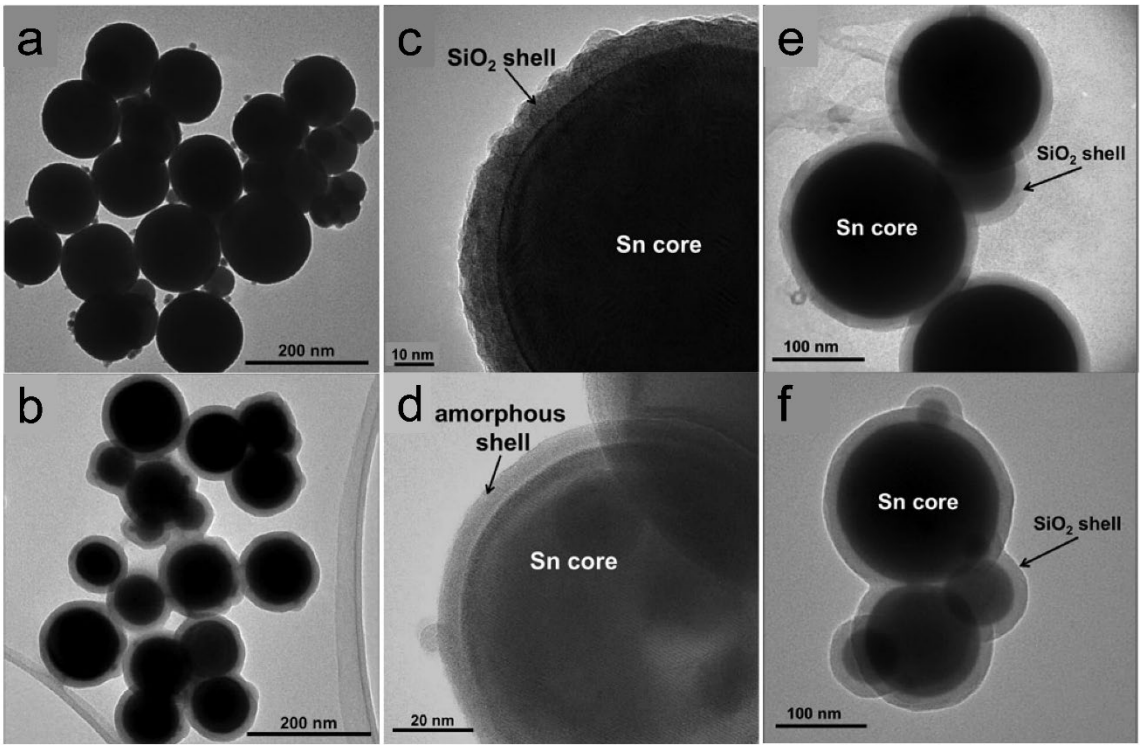

Figure 1.3 Encapsulated Sn nanoparticles that synthesized by modified polyol reduction method followed by sol–gel silica encapsulation for advanced heat transfer and thermal energy storage. [67]

TEM image of (a) as-prepared Sn nanoparticles and (b) Sn/SiO_2 nanoparticles; High-resolution TEM images of (c) Sn/SiO_2 phase change nanoparticles showing crystalline silica shell with a thick grain boundary between the shell and the Sn core. (d) Unencapsulated Sn nanoparticles showing amorphous SnO_x layer formed on the surface. TEM images of Sn/SiO_2 phase change nanoparticles (e) before and (f) after 20 heating and cooling cycles.

Hsu *et al.* prepared Zn@TiO_2, Zn@Al_2O_3 [68] and Zn@SiO_2 [33, 69] core-shell microparticles by hydrolysis reactions (Zn@TiO_2 and Zn@SiO_2) and thermal decomposition method (Zn@Al_2O_3), which are shown in Figure 1.4A. The Zn@Al_2O_3 microparticles were dispersed into the Hitec salt composed by 53 wt% KNO_3, 40 wt%

$NaNO_2$ and 7 wt% $NaNO_3$, which is designed as the heat transfer fluid in CSP plants. [70] The heat capacity of the salt can be enhanced by 6.7% by doping with 10 wt% Zn/Al_2O_3 microparticles while the viscosity increased from 1.3 to 3 cp in the temperature range from 350 to 550°C. In this study, thermal hysteresis (TH) of the phase change core-shell microparticles was defined as the difference between the melting and the crystallization temperatures, which was found increased with the increasing shell thickness and ramping rate from the DSC data. The discussion for TH is important since the latent heats of the PCMs cannot be released and restored during cycling if the TH is beyond the operation temperature range of a TES system. Moreover, among $Zn@TiO_2$, $Zn@Al_2O_3$ and $Zn@SiO_2$, the smallest TH was exhibited in $Zn@Al_2O_3$ due to the higher thermal conductivity of Al_2O_3 than that of TiO_2 and SiO_2.

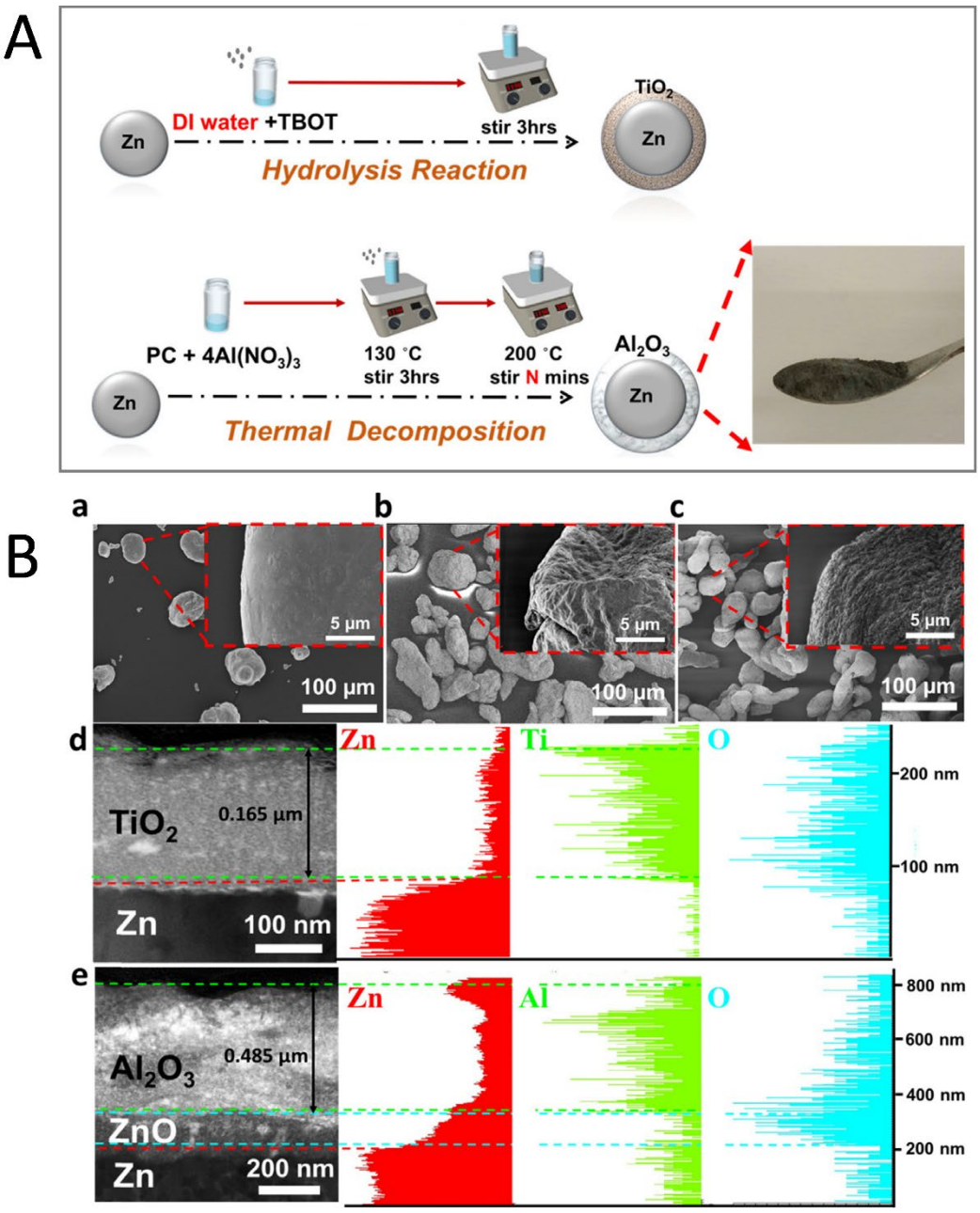

Figure 1.4 Synthesis and morphology of Zn@TiO_2 and Zn@Al_2O_3. [68]

(A) Experimental procedure for synthesizing Zn/TiO_2 microparticles and Zn/Al_2O_3 microparticles, and the insert is a picture showing the synthesized Zn/Al_2O_3 microparticles. (B) SEM images of (a) pure Zn, (b) Zn/TiO_2, and (c) Zn/Al_2O_3 microparticles. (d) and (e) TEM cross-sectional images and EDS analysis for Zn/TiO_2 and Zn/Al_2O_3 microparticles, respectively.

Self-encapsulation. For protecting low melting point metal PCMs, self-encapsulation is another tool. Navarrete *et al.* used $Sn@SnO_x$ nanoparticles as self-encapsulated NEPCM using the oxides shell that forms when exposed to air. [71] When dispersing $Sn@SiO_x$ into a commercial thermal oil (Therminol 66) to form nanofluids, the increase in both the thermal conductivity and heat capacity of the base fluid were achieved, which is contributed by the high thermal conductivity of Sn and the latent heat from the melting of Sn nanoparticles. The thermal stability of of $Sn@SiO_x$ in both powder form and nanofluid form was checked by performing melt-freeze cyclic test. In addition, to reduce supercooling, they used non-eutectic metal alloys (Sn/Pb) nanoparticles in which the co-exist solid and liquid phase during heating contributes to the heterogeneous crystallization that leading to the reduction of the supercooling, compared to the completely melted ones.

Polymer. Polymer shell can also be applied in the microencapsulation of low melting point metals and alloys. Blaiszik *et al.* prepared a liquid metal alloy of gallium-indium (Ga-In) microencapsulated with urea-formaldehyde (UF) by *in situ* polymerization. [72] The obtained microcapsules shown in Figure 1.5 exhibit an approximately 73-nm thick shell and ellipsoidal shape with major and minor diameter aspect ratios ranging from 1.64 to 1.08 and with major diameters ranging from 3 to 245 μm. The major and minor diameters decreased with aspect ratio by increasing agitation rate. Moreover, the aspect ratio decreased to 1.08 with further increasing shear rate by sonication. The thermal properties of the microencapsulated Ga-In alloy were investigated by TGA and DSC.

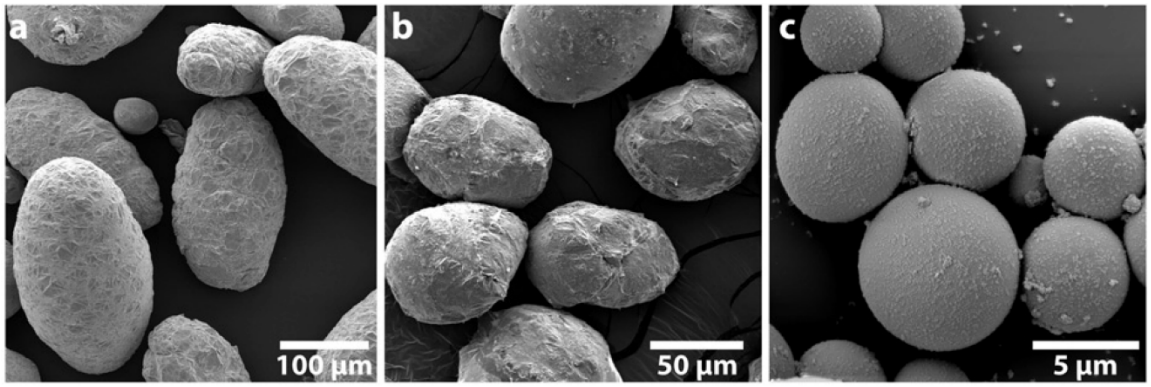

Figure 1.5 Microencapsulated gallium–indium (Ga–In) liquid metal. [72]

SEM images of Ga–In filled capsules at varying size scales. Capsules prepared (a) at an agitation rate of 1500 rpm (b) at an agitation rate of 2750 rpm and (c) via sonication.

Carbon encapsulation. Due to the superior thermal conductivity, carbon materials are good candidates for encapsulating low melting point metals and alloys.

Zhong et al. submerged the graphite foams into the melted Wood's alloy (a eutectic alloy of 50% Bi, 26.7% Pb, 13.3% Sn, and 10% Cd by weight [73]) to form the graphite foam/Wood's alloy composites. High thermal conductivity of the composites (193.74 $W \cdot m^{-1} \cdot K^{-1}$) was achieved which is 2 times higher when compared to the alloy and graphite foam. Also, significant reduction in coefficient of thermal expansion of the composite (7.82 $ppm \cdot K^{-1}$) was realized compared with that of the alloy (24.81 $ppm \cdot K^{-1}$), while the latent heat did not change too much. In addition, the composites show an enhanced mechanical properties compared to graphite foam when the alloy is in both solid phase and liquid phase. [74]

They also infiltrated Wood's alloy into the compressed expanded natural graphite (CENG) on the purpose of enhancing the thermal conductivity of the composites. In this study, thermal conductivity of the composites can be 2.8–5.8 times higher than that of the Wood's alloy (58.88 $W \cdot m^{-1} \cdot K^{-1}$). Combining with the latent heat of the composites (ranges from 29.27 to 34.20 J/g), the composites exhibit the potential for heat management in electronic devices. [75]

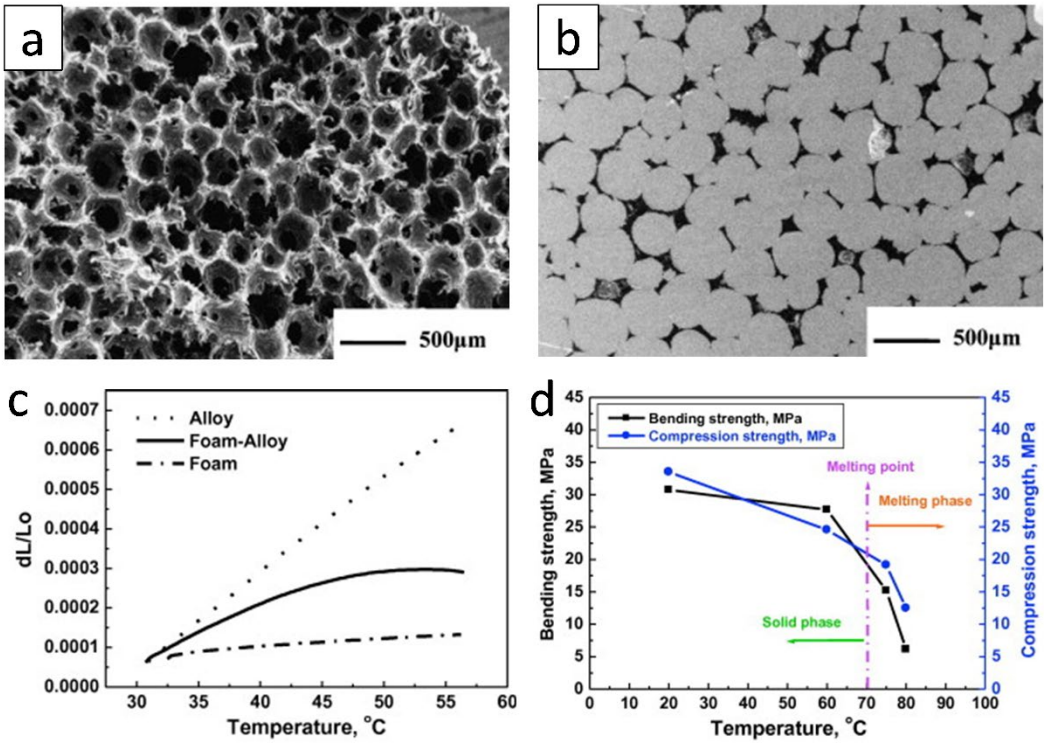

Figure 1.6 Thermal and mechanical properties of graphite foam/Wood's alloy composite for thermal energy storage. [74]

SEM image of (a) the unfilled graphite foam (b) the polished surface of the alloy filled graphite foam. (c) Thermal expansion of the Wood's alloy, graphite foam, and graphite foam/Wood's alloy composite. (d) The compression strength and bending strength of the composites as a function of the temperature.

Tran *et al.* synthesized the composites in which the mesoporous carbon matrix was distributed with ligand-free metal nanoparticles (Bi or Pb) on the purpose of forming form-stable PCMs. [76] The embedded metal nanoparticles possess the tunable melting temperatures which are controlled by changing the size of metal nanoparticles through tuning the amount of metal loaded inside the composites. The decrease of melting temperature of both Bi and Pb nanoparticles comparing to their bulk counterparts was observed. During 18 melt–freeze cycles, phase change temperatures are stable. As the encapsulating material for metal nanoparticles, the carbon matrix prevents aggregation of the NPs, accommodates volume change, and prevents leakage of liquid state PCMs. In addition, they also found that the porous channels in the carbon matrix serve as containers for the melted Pb nanoparticles.

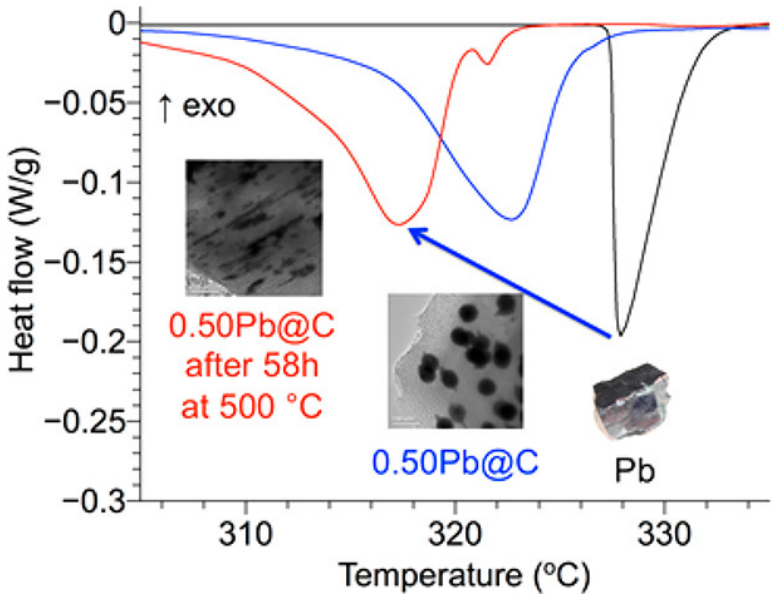

Figure 1.7 Metal nanoparticle–carbon matrix composites with tunable melting temperature as PCMs for TES. [74]

The different onset temperatures of the exothermic peaks show the tunable melting temperature of Pb@C composites.

1.4.2.2 Micro/Nano Encapsulation of High Melting Point Metals and Alloys

So far, the most studied material for mico/nano encapsulating high melting point metals and alloys is alumina due to its superior stability and facile encapsulation method.

Navarrete *et al.* encapsulated the commercial Al-Cu alloy nanoparticles with a naturally formed Al_2O_3 layer when exposed to oxygen. [77] The encapsulated Al-Cu nanoparticles were added to the so-called solar salt (60 wt% $NaNO_3$, 40 wt% KNO_3) to form nanofluids on the purpose of improving the TES performance. The Al-Cu NEPCM showed chemical compatibility with the solar salt by performing thermal cycling test. Although the specific heat that contributes to the sensible heat storage decreased with

the addition of solid content, the latent heat contributed by the enthalpy of fusion of Al-Cu NEPCM increased the total thermal energy storage up to 17.8% in the same volume. Moreover, the addition of Al-Cu NEPCM increased the thermal conductivity of the nanofluids which improved the heat transfer performance of solar salt based HTF.

Nomura *et al.* first developed Al-Si alloy microsphere MEPCMs covered by α-Al_2O_3 shells through a two-step procedure, in which the first step is using boehmite treatment to form an AlOOH shell on the Al-25 wt%Si alloy microparticles, and the second step is heat-oxidation treatment in an O_2 atmosphere to transform AlOOH shell into a more stable α-Al_2O_3 shell. [78] The spherical of Al-25 wt%Si microparticles (36.3 μm in diameter), used as raw materials, were produced by spinning disk atomization. This Al-Si-based MEPCM exhibited the phase change at 573°C with the latent heat of 247 $J \cdot g^{-1}$. In addition, the 10 melt-freeze cyclic test in air showed effective function of the encapsulation in cycling performance. In their another research, Nomura *et al.* reported that, in Al-Si alloy MEPCMs, the observed void inside the alloy core allowed for volume expansion of the PCMs during solid-liquid phase transitions. [79] In addition, the MEPCM exhibits excellent durability up to 300 heating and cooling cycles under oxygen atmosphere, which can potentially be used in the next-generation LHS-based high-temperature thermal energy storage and transportation systems.

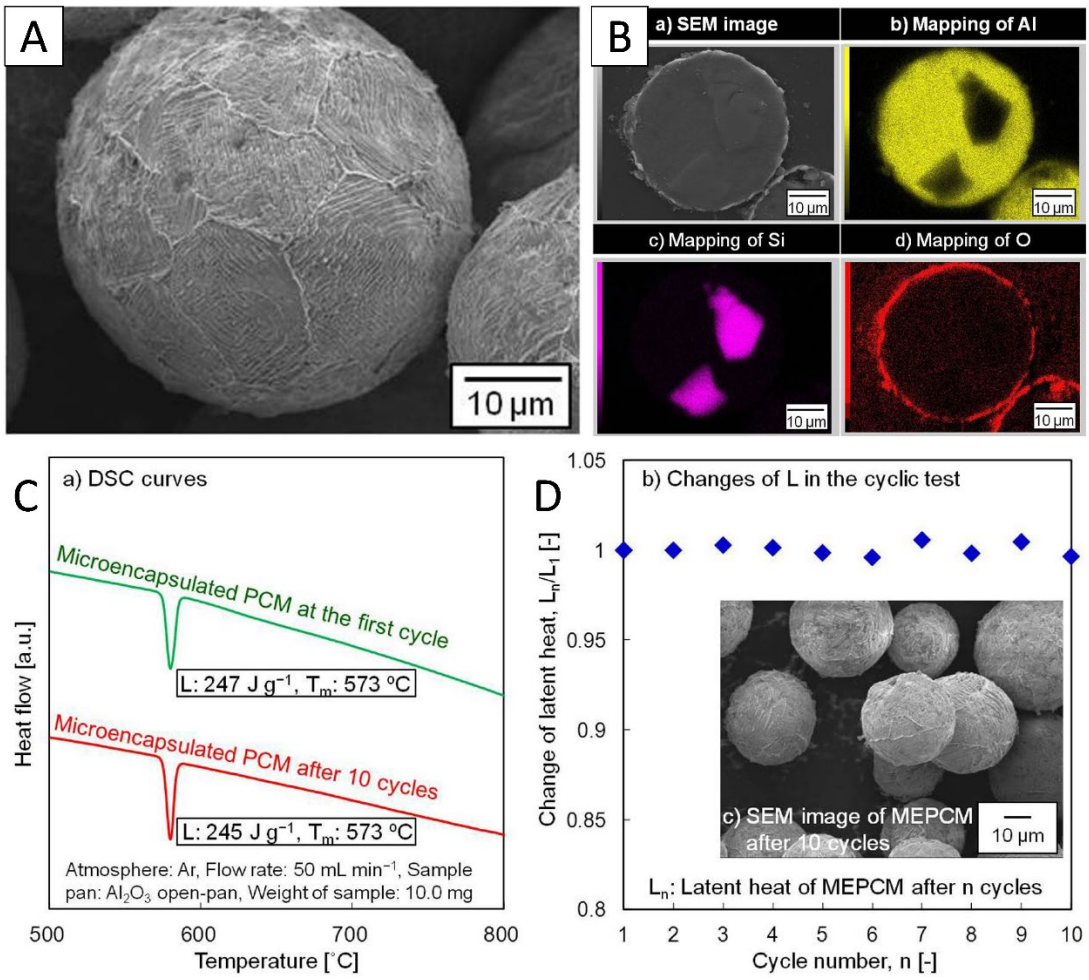

Figure 1.8 Microencapsulation of Al-Si-based PCM for high-temperature thermal energy storage. [78]

(A) SEM image of Al-Si MEPCM. (B) Cross-section EDS elemental mapping results of Al-Si MEPCM. (C) DSC curves of MEPCM at the first and after 10 melt-freeze cycles in air. (D) The changes in the latent heat of MEPCM during melt-freeze cyclic test. The inset SEM image shows the morphology of MEPCM after 10 melt-freeze cycles.

Furthermore, Nomura *et al.* developed MEPCMs from Al-Si alloys microparticles with four different Al-Si compositions (Al-12 wt%Si, Al-17 wt%Si, Al-20 wt%Si, and Al-30 wt%Si) on the purpose of investigating the effect of the Si content

in the PCM core on thermal storage ability of MEPCM. [80] Similar method was used for micro-encapsulation as shown in their previous studies. [78, 79] Their results revealed an increase in MEPCM thermal storage capacity with decreasing Si content and lowering the heat oxidation temperature. In addition, larger supercooling was observed in the samples with higher Si content.

It was found that leakage could occur after more than 300 cycles of melt-freeze cycles due to the incompact, non-uniform and crackable Al_2O_3 shell formed in their previous studies. [78-80] To improve the shell stability of MEPCMs in high temperature conditions, Nomura *et al.* developed the Al–Si alloy MEPCM microspheres with high-temperature stability and good cycling durability over 3000 cycles through a modified method (shown in Figure 1.9a) compared to that in their previous studies. The modified method contained three steps: (1) boehmite treatment at pH value of 8; (2) additional $Al(OH)_3$ precipitation on the surface of Al-Si microparticles; (3) heat-oxidation in an O_2 atmosphere. With modified method, the uniform and highly durable Al_2O_3 shell is formed which contributed to the good durability of the Al–Si alloy MEPCMs over 3000 melt-freeze cycles in air (Figure 1.9b). [81]

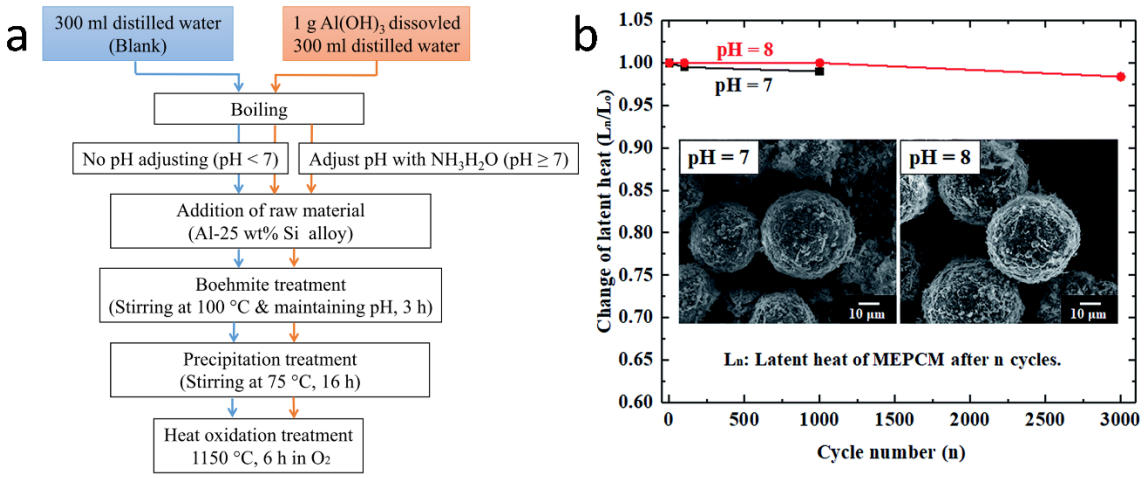

Figure 1.9 A microencapsulated Al–Si phase change material with high-temperature thermal stability and durability over 3000 cycles. [81]

(a) Procedures for the preparation of Al-Si/Al_2O_3 core/shell MEPCM particles. (b) Evolution of latent heat of MEPCMs with the number of melting–solidification cycles. Inset shows the SEM images of the MEPCMs after 1000 melting–solidification cycles.

Except for the NEPCM in Al-Si system, Nomura *et al.* also chose only Al (T_m = 660 °C) as the PCM to prepare core-shell MEPCMs that composed of a stable α-Al_2O_3 shell and an Al core through a two-step method which was like the method used for Al-Si alloy MEPCMs. The heat-storage capacity of the MEPCMs decreased (273–301 $J \cdot g^{-1}$) while the repetition durability improved with the increase of the heat oxidation temperature. [82]

He *et al.* used the sol–gel process with the modification of silane coupling agent (SCA) to prepare Al-Si/Al_2O_3 core-shell microparticles in which a dense α-Al_2O_3 shell layer with the thickness of 3–5 μm (Figure 1.10a). [83] During the synthesis procedure, first, the commercial Al-Si eutectic alloy microparticles were washed with ethanol and

then modified on surface with silane coupling agent. Finally, the modified Al-Si eutectic alloy microparticles was treated with alumina sols. The obtained Al-Si/Al_2O_3 core-shell microparticles have a latent heat of 307.21 $kJ \cdot kg^{-1}$. The silane coupling agent on the surface of Al-Si alloy microparticles plays a key role in microencapsulation, promoting the condensation between boehmite sols and silanol groups (Figure 1.10b).

They also studied the structural and phase change characteristics of Al-Si/Al_2O_3 core/shell during melt-freeze cycling from room temperature to 1000°C. [84] The latent heat of Al-Si/Al_2O_3 core-shell microparticles reduced to 271.90 $kJ \cdot kg^{-1}$ after 20 melt-freeze cycles. The ruptured structure after cycling was caused by the mismatch of thermal stress between the core and the shell. They demonstrated that the cracks at the core-shell interface can release the thermal stress during thermal cycling.

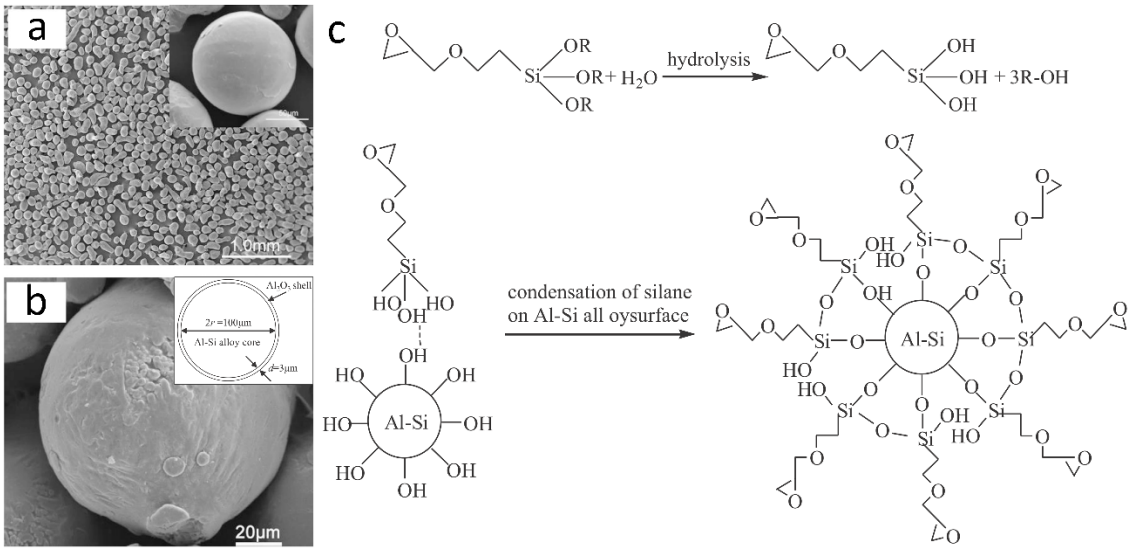

Figure 1.10 Inorganic microencapsulated core-shell structure of Al-Si alloy microparticles with silane coupling agent. [83]

SEM images of Al-Si alloy microparticles (a) after surface modification and (b) after surface modification and heating at 400°C. The inset figure in b shows the sketch of Al-Si/Al_2O_3 core/shell particles. (c) Reaction mechanism of silane coupling agent treatment to Al–Si alloy.

Furthermore, He *et al.* compared two methods for the synthesis of inorganic microencapsulated core-shell Al-Si alloy microparticles based on the sol-gel process: (1) pre-oxidation process; (2) modification with silane coupling agent of original Al-Si alloy microparticles. [85] It was found that both two methods can be used for microencapsulation and form stable dense α-Al_2O_3 shell. Pre-oxidation process prone to generate the nonuniform shell while the modification of SCA can realize more uniform microencapsulation. Moreover, according to the results of zeta potential measurement, both two methods change surface electric behaviors of Al–Si alloy

microparticles. The modification of SCA is more likely to absorb alumina sols on the surfaces, thus renders thicker and more uniform Al_2O_3 shell.

Li *et al.* reported the microencapsulation of Al microspheres via an induced oxidation method. [86] The nano Ni species loaded on the surface of Al microspheres act as catalyst to accelerate the oxidation of the surface Al layer during oxidation in air. The activation energy (149-156 $kJ \cdot mol^{-1}$) of the oxidation of Al is much lower than the previous reported ones due to the presence of Ni species. By monitoring the oxygen consumption and the exothermic changes during the oxidation process, it is found that the oxidation of surface Al layer contains three steps, which results in the formation of a layered Al_2O_3 shell. With the presence of voids in the core, the layered structure of the Al_2O_3 shell improves the elasticity of the core-shell structure thus improves the thermal stability during melt-freeze cycles.

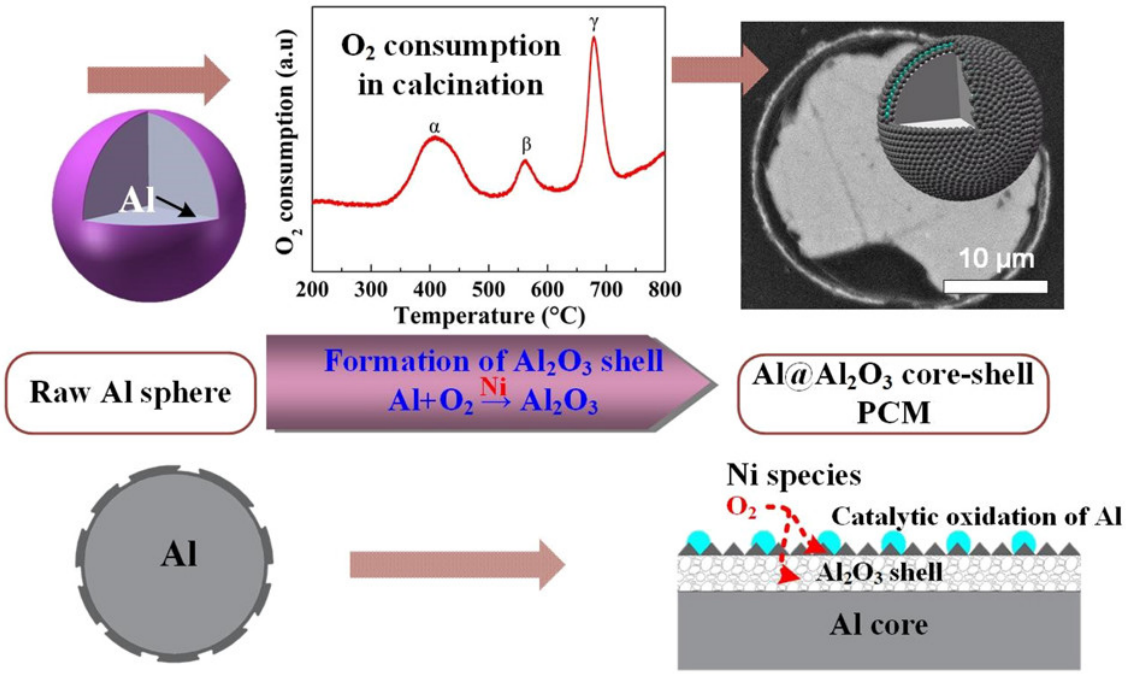

Figure 1.11 Facile synthesis of Al@Al_2O_3 microcapsule via a Ni modified method for high-temperature thermal energy storage. [86]

Metal microencapsulation. With the consideration of good ductility, high thermal conductivity and high melting temperature, some metals are also good candidates for the encapsulation materials for high melting point metal/alloy PCMs. Nomura *et al.* synthesized the MEPCM with spherical Al-25 wt% Si core (average diameter: 36 μm) and Al_2O_3@Cu multilayered shell as shown in Figure 1.12a. [87] The Al-25 wt%Si microparticles covered with Al_2O_3 shell were prepared by boehmite treatment and the further heating at 500 °C. Then, HCl solution was used to etch the Al_2O_3 covered microparticles, and electroless plating of Cu layer is carried out to form

the multilayered MEPCM (Figure 1.12b). The core-shell Al-25 wt%Si@Al_2O_3@Cu particles exhibit a low breakage ratio of about 1.7% after 100 melt-freeze cycles.

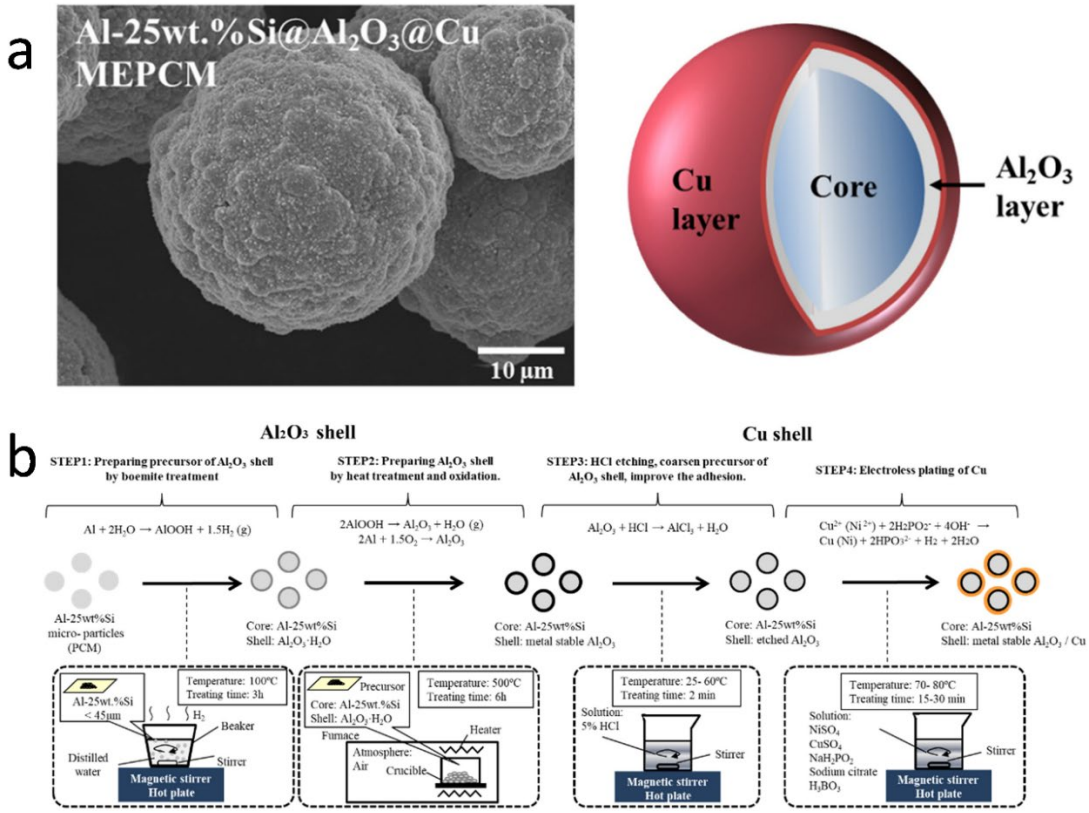

Figure 1.12 Synthesis of Al-25 wt% Si@Al_2O_3@Cu MEPCMs for high temperature thermal energy storage. [87]

(a) SEM view and schematic of core/shell Al-25 wt% Si@Al_2O_3@Cu MEPCM particle. (b) Experimental procedure for Synthesis of Al-25 wt% Si@Al_2O_3@Cu MEPCM.

1.5 The Objectives of This Study

The aims of this dissertation are to explore various synthetic methods, to create unique micro/nanostructures, thus, to make the best use of the high thermal conductivity of low melting point metal PCMs, isolate them from outside environment for protection and also seek the novel methods for the further morphology control of related PCMs. Silica (SiO_2) and alumina (Al_2O_3) were chosen as the encapsulation materials due to their good physical and chemical stability. [88] Until now, only a few examples have been reported to achieve using SiO_2 and Al_2O_3 to coat low-melting-point metal for thermal energy storage. [68] Compared to them, in this dissertation, more facile and more customized methods were used, and the PCMs with unique structures named Sn NPs@p-SiO_2 and Sn@Al_2O_3 with good thermal cyclic stability were fabricated. In the case of using SiO_2 to encapsulate Sn NPs, a novel transformation from Sn@SiO_2 core-shell NPs to Sn@SiO_2 yolk-shell NPs and SnO_2@SiO_2 hollow NPs were observed, based on which the nanostructure control via liquid metal diffusion was first time realized.

References

1. Agency, I. E. *Key World Energy Statistics (2018)*; 2018; p 14.
2. Golledge, N. R.; Keller, E. D.; Gomez, N.; Naughten, K. A.; Bernales, J.; Trusel, L. D.; Edwards, T. L., Global environmental consequences of twenty-first-century ice-sheet melt. *Nature* **2019,** *566* (7742), 65-72.
3. Trusel, L. D.; Das, S. B.; Osman, M. B.; Evans, M. J.; Smith, B. E.; Fettweis, X.; McConnell, J. R.; Noël, B. P. Y.; van den Broeke, M. R., Nonlinear rise in

Greenland runoff in response to post-industrial Arctic warming. *Nature* **2018,** *564* (7734), 104-108.
4. Morocco largest Concentrated Solar Power complex NOOR 1,2,3. http://helioscsp.com/morocco-largest-concentrated-solar-power-complex-noor-123/.
5. Massive Solar Power Plant Begins Operations in Morocco. https://www.architecturaldigest.com/story/massive-solar-power-plant-noor-opens-morocco-sahara-desert.
6. Cabeza, L. F., *Advances in thermal energy storage systems: Methods and applications*. Elsevier: 2014.
7. Yan, T.; Wang, R. Z.; Li, T. X.; Wang, L. W.; Fred, I. T., A review of promising candidate reactions for chemical heat storage. *Renewable and Sustainable Energy Reviews* **2015,** *43*, 13-31.
8. Pardo, P.; Deydier, A.; Anxionnaz-Minvielle, Z.; Rougé, S.; Cabassud, M.; Cognet, P., A review on high temperature thermochemical heat energy storage. *Renewable and Sustainable Energy Reviews* **2014,** *32*, 591-610.
9. Wei, G.; Wang, G.; Xu, C.; Ju, X.; Xing, L.; Du, X.; Yang, Y., Selection principles and thermophysical properties of high temperature phase change materials for thermal energy storage: A review. *Renewable and Sustainable Energy Reviews* **2018,** *81*, 1771-1786.
10. Chandra, D.; Chellappa, R.; Chien, W.-M., Thermodynamic assessment of binary solid-state thermal storage materials. *Journal of Physics and Chemistry of Solids* **2005,** *66* (2), 235-240.
11. Cao, Q.; Liu, P., Hyperbranched polyurethane as novel solid–solid phase change material for thermal energy storage. *European Polymer Journal* **2006,** *42* (11), 2931-2939.
12. Kenisarin, M. M., Thermophysical properties of some organic phase change materials for latent heat storage. A review. *Solar Energy* **2014,** *107*, 553-575.
13. Kleiner, F.; Posern, K.; Osburg, A., Thermal conductivity of selected salt hydrates for thermochemical solar heat storage applications measured by the light flash method. *Applied Thermal Engineering* **2017,** *113*, 1189-1193.
14. Xie, N.; Huang, Z.; Luo, Z.; Gao, X.; Fang, Y.; Zhang, Z., Inorganic Salt Hydrate for Thermal Energy Storage. *Applied Sciences* **2017,** *7* (12).
15. Kenisarin, M.; Mahkamov, K., Salt hydrates as latent heat storage materials:Thermophysical properties and costs. *Solar Energy Materials and Solar Cells* **2016,** *145*, 255-286.
16. Pielichowska, K.; Pielichowski, K., Phase change materials for thermal energy storage. *Progress in Materials Science* **2014,** *65*, 67-123.

17. Nagano, K.; Mochida, T.; Takeda, S.; Domański, R.; Rebow, M., Thermal characteristics of manganese (II) nitrate hexahydrate as a phase change material for cooling systems. *Applied Thermal Engineering* **2003,** *23* (2), 229-241.
18. Cabeza, L. F.; Svensson, G.; Hiebler, S.; Mehling, H., Thermal performance of sodium acetate trihydrate thickened with different materials as phase change energy storage material. *Applied Thermal Engineering* **2003,** *23* (13), 1697-1704.
19. Kenisarin, M. M., High-temperature phase change materials for thermal energy storage. *Renewable and Sustainable Energy Reviews* **2010,** *14* (3), 955-970.
20. Peng, Q.; Yang, X.; Ding, J.; Wei, X.; Yang, J., Design of new molten salt thermal energy storage material for solar thermal power plant. *Applied Energy* **2013,** *112*, 682-689.
21. Nagasaka, Y.; Nagashima, A., The thermal conductivity of molten NaNO3 and KNO3. *International Journal of Thermophysics* **1991,** *12* (5), 769-781.
22. Santini, R.; Tadrist, L.; Pantaloni, J.; Cerisier, P., Measurement of thermal conductivity of molten salts in the range 100–500°C. *International Journal of Heat and Mass Transfer* **1984,** *27* (4), 623-626.
23. Nomura, T.; Akiyama, T., High-temperature latent heat storage technology to utilize exergy of solar heat and industrial exhaust heat. *International Journal of Energy Research* **2017,** *41* (2), 240-251.
24. Nomura, T.; Sheng, N.; Zhu, C.; Saito, G.; Hanzaki, D.; Hiraki, T.; Akiyama, T., Microencapsulated phase change materials with high heat capacity and high cyclic durability for high-temperature thermal energy storage and transportation. *Applied Energy* **2017,** *188*, 9-18.
25. Sun, J. Q.; Zhang, R. Y.; Liu, Z. P.; Lu, G. H., Thermal reliability test of Al–34%Mg–6%Zn alloy as latent heat storage material and corrosion of metal with respect to thermal cycling. *Energy Conversion and Management* **2007,** *48* (2), 619-624.
26. Fukahori, R.; Nomura, T.; Zhu, C.; Sheng, N.; Okinaka, N.; Akiyama, T., Thermal analysis of Al–Si alloys as high-temperature phase-change material and their corrosion properties with ceramic materials. *Applied Energy* **2016,** *163*, 1-8.
27. Maruoka, N.; Akiyama, T., Exergy recovery from steelmaking off-gas by latent heat storage for methanol production. *Energy* **2006,** *31* (10), 1632-1642.
28. Wang, X.; Liu, J.; Zhang, Y.; Di, H.; Jiang, Y., Experimental research on a kind of novel high temperature phase change storage heater. *Energy Conversion and Management* **2006,** *47* (15), 2211-2222.
29. Pan, A.; Wang, J.; Zhang, X., Prediction of Melting Temperature and Latent Heat for Low-melting Metal PCMs. *Rare Metal Materials and Engineering* **2016,** *45* (4), 874-880.

30. Su, W.; Darkwa, J.; Kokogiannakis, G., Review of solid–liquid phase change materials and their encapsulation technologies. *Renewable and Sustainable Energy Reviews* **2015,** *48*, 373-391.
31. Manasijevic, I.; Balanovic, L.; Grguric, T. H.; Minic, D.; Gorgievski, M., Study of Microstructure and Thermal Properties of the Low Melting Bi-In-Sn Eutectic Alloys. *Materials Research-Ibero-American Journal of Materials* **2018,** *21* (6).
32. Wang, Q.-M.; Cheng, X.-M.; Li, Y.-Y.; Yu, G.-M.; Liu, Z., Microstructures and thermal properties of Sn–Bi–Pb–Zn alloys as heat storage and transfer materials. *Rare Metals* **2019,** *38* (4), 350-358.
33. Lai, C.-C.; Chang, W.-C.; Hu, W.-L.; Wang, Z. M.; Lu, M.-C.; Chueh, Y.-L., A solar-thermal energy harvesting scheme: enhanced heat capacity of molten HITEC salt mixed with Sn/SiO_x core–shell nanoparticles. *Nanoscale* **2014,** *6* (9), 4555-4559.
34. Paris, J.; Falardeau, M.; Villeneuve, C., Thermal Storage by Latent Heat: A Viable Option for Energy Conservation in Buildings. *Energy Sources* **1993,** *15* (1), 85-93.
35. Ge, H. S.; Liu, J., Keeping Smartphones Cool With Gallium Phase Change Material. *J Heat Trans-T Asme* **2013,** *135* (5).
36. Yang, X.-H.; Tan, S.-C.; He, Z.-Z.; Liu, J., Finned heat pipe assisted low melting point metal PCM heat sink against extremely high power thermal shock. *Energy Conversion and Management* **2018,** *160*, 467-476.
37. Kondo, M.; Ishii, M.; Muroga, T., Corrosion of steels in molten gallium (Ga), tin (Sn) and tin lithium alloy (Sn–20Li). *Fusion Engineering and Design* **2015,** *98-99*, 2003-2008.
38. Ghadimi, A.; Saidur, R.; Metselaar, H. S. C., A review of nanofluid stability properties and characterization in stationary conditions. *Int. J. Heat Mass Transfer* **2011,** *54* (17), 4051-4068.
39. Hawlader, M. N. A.; Uddin, M. S.; Khin, M. M., Microencapsulated PCM thermal-energy storage system. *Applied Energy* **2003,** *74* (1-2), 195-202.
40. Qiu, Z.; Ma, X.; Li, P.; Zhao, X.; Wright, A., Micro-encapsulated phase change material (MPCM) slurries: Characterization and building applications. *Renewable & Sustainable Energy Reviews* **2017,** *77*, 246-262.
41. Nomura, T.; Zhu, C.; Sheng, N.; Saito, G.; Akiyama, T., Microencapsulation of Metal-based Phase Change Material for High-temperature Thermal Energy Storage. *Scientific Reports* **2015,** *5*, 9117.
42. Aftab, W.; Huang, X.; Wu, W.; Liang, Z.; Mahmood, A.; Zou, R., Nanoconfined phase change materials for thermal energy applications. *Energy Environ. Sci.* **2018,** *11* (6), 1392-1424.

43. Shchukina, E. M.; Graham, M.; Zheng, Z.; Shchukin, D. G., Nanoencapsulation of phase change materials for advanced thermal energy storage systems. *Chemical Society Reviews* **2018,** *47* (11), 4156-4175.
44. Hassan, A.; Laghari, M. S.; Rashid, Y., Micro-Encapsulated Phase Change Materials: A Review of Encapsulation, Safety and Thermal Characteristics. *Sustainability-Basel* **2016,** *8* (10).
45. Wang, Y.; Liu, Z. M.; Niu, X. F.; Ling, X., Preparation, Characterization, and Thermal Properties of Microencapsulated Phase Change Material for Low-Temperature Thermal Energy Storage. *Energy & Fuels* **2019,** *33* (2), 1631-1636.
46. McClements, D. J., Nanoemulsions versus microemulsions: terminology, differences, and similarities. *Soft Matter* **2012,** *8* (6), 1719-1729.
47. Rao, J. P.; Geckeler, K. E., Polymer nanoparticles: Preparation techniques and size-control parameters. *Progress in Polymer Science* **2011,** *36* (7), 887-913.
48. Perignon, C.; Ongmayeb, G.; Neufeld, R.; Frere, Y.; Poncelet, D., Microencapsulation by interfacial polymerisation: membrane formation and structure. *J. Microencapsul.* **2015,** *32* (1), 1-15.
49. Giro-Paloma, J.; Martínez, M.; Cabeza, L. F.; Fernández, A. I., Types, methods, techniques, and applications for microencapsulated phase change materials (MPCM): A review. *Renewable and Sustainable Energy Reviews* **2016,** *53*, 1059-1075.
50. Zhao, C. Y.; Zhang, G. H., Review on microencapsulated phase change materials (MEPCMs): Fabrication, characterization and applications. *Renew. Sust. Energ. Rev.* **2011,** *15* (8), 3813-3832.
51. Sawant, S.; Shegokar, R., Chapter 5 - Bone scaffolds: What's new in nanoparticle drug delivery research? In *Nanobiomaterials in Hard Tissue Engineering*, Grumezescu, A. M., Ed. William Andrew Publishing: 2016; pp 155-187.
52. Deveci, S. S.; Basal, G., Preparation of PCM microcapsules by complex coacervation of silk fibroin and chitosan. *Colloid and Polymer Science* **2009,** *287* (12), 1455-1467.
53. Demirbag, S.; Aksoy, S. A., Encapsulation of Phase Change Materials by Complex Coacervation to Improve Thermal Performances and Flame Retardant Properties of the Cotton Fabrics. *Fibers and Polymers* **2016,** *17* (3), 408-417.
54. Malekipirbazari, M.; Sadrameli, S. M.; Dorkoosh, F.; Sharifi, H., Synthetic and physical characterization of phase change materials microencapsulated by complex coacervation for thermal energy storage applications. *International Journal of Energy Research* **2014,** *38* (11), 1492-1500.
55. Konuklu, Y.; Unal, M.; Paksoy, H. O., Microencapsulation of caprylic acid with different wall materials as phase change material for thermal energy storage. *Solar Energy Materials and Solar Cells* **2014,** *120*, 536-542.

56. Onder, E.; Sarier, N.; Cimen, E., Encapsulation of phase change materials by complex coacervation to improve thermal performances of woven fabrics. *Thermochimica Acta* **2008,** *467* (1-2), 63-72.
57. Brinker, C. J.; Scherer, G. W., CHAPTER 1 - Introduction. In *Sol-Gel Science*, Brinker, C. J.; Scherer, G. W., Eds. Academic Press: San Diego, 1990; pp xvi-18.
58. Geng, L.; Wang, S.; Wang, T.; Luo, R., Facile Synthesis and Thermal Properties of Nanoencapsulated n-Dodecanol with SiO2 Shell as Shape-Formed Thermal Energy Storage Material. *Energy & Fuels* **2016,** *30* (7), 6153-6160.
59. Varga, M., Chapter 3 - Self-assembly of nanobiomaterials. In *Fabrication and Self-Assembly of Nanobiomaterials*, Grumezescu, A. M., Ed. William Andrew Publishing: 2016; pp 57-90.
60. Akhiani, A. R.; Mehrali, M.; Tahan Latibari, S.; Mehrali, M.; Mahlia, T. M. I.; Sadeghinezhad, E.; Metselaar, H. S. C., One-Step Preparation of Form-Stable Phase Change Material through Self-Assembly of Fatty Acid and Graphene. *The Journal of Physical Chemistry C* **2015,** *119* (40), 22787-22796.
61. Li, M.; Rouaud, O.; Poncelet, D., Microencapsulation by solvent evaporation: State of the art for process engineering approaches. *International Journal of Pharmaceutics* **2008,** *363* (1), 26-39.
62. Soh, H. S.; Lee, Y. L., Microencapsulation and Nanoencapsulation Using Supercritical Fluid (SCF) Techniques. *Pharmaceutics* **2019,** *11* (1).
63. Gharsallaoui, A.; Roudaut, G.; Chambin, O.; Voilley, A.; Saurel, R., Applications of spray-drying in microencapsulation of food ingredients: An overview. *Food Research International* **2007,** *40* (9), 1107-1121.
64. Kim, J.-Y.; An, S.-H.; Rhee, Y.-S.; Park, C.-W.; Park, E.-S., A Comparative Study Between Spray-Drying and Fluidized Bed Coating Processes for the Preparation of Pramipexole Controlled-Release Microparticles for Orally Disintegrating Tablets. *Dry. Technol.* **2014,** *32* (8), 935-945.
65. Jaworek, A., Electrostatic micro- and nanoencapsulation and electroemulsification: A brief review. *J. Microencapsul.* **2008,** *25* (7), 443-468.
66. Hong, Y.; Ding, S.; Wu, W.; Hu, J.; Voevodin, A. A.; Gschwender, L.; Snyder, E.; Chow, L.; Su, M., Enhancing Heat Capacity of Colloidal Suspension Using Nanoscale Encapsulated Phase-Change Materials for Heat Transfer. *ACS Appl. Mater. Interfaces* **2010,** *2* (6), 1685-1691.
67. Cingarapu, S.; Singh, D.; Timofeeva, E. V.; Moravek, M. R., Nanofluids with encapsulated tin nanoparticles for advanced heat transfer and thermal energy storage. *International Journal of Energy Research* **2014,** *38* (1), 51-59.

68. Hsu, T.-H.; Chung, C.-H.; Chung, F.-J.; Chang, C.-C.; Lu, M.-C.; Chueh, Y.-L., Thermal hysteresis in phase-change materials: Encapsulated metal alloy core-shell microparticles. *Nano Energy* **2018,** *51*, 563-570.
69. Lai, C.-C.; Lin, S.-M.; Chu, Y.-D.; Chang, C.-C.; Chueh, Y.-L.; Lu, M.-C., Tunable endothermic plateau for enhancing thermal energy storage obtained using binary metal alloy particles. *Nano Energy* **2016,** *25*, 218-224.
70. Fernández, A. G.; Galleguillos, H.; Fuentealba, E.; Pérez, F. J., Thermal characterization of HITEC molten salt for energy storage in solar linear concentrated technology. *Journal of Thermal Analysis and Calorimetry* **2015,** *122* (1), 3-9.
71. Navarrete, N.; Gimeno-Furio, A.; Mondragon, R.; Hernandez, L.; Cabedo, L.; Cordoncillo, E.; Julia, J. E., Nanofluid based on self-nanoencapsulated metal/metal alloys phase change materials with tuneable crystallisation temperature. *Sci. Rep.* **2017,** *7* (1), 17580.
72. Blaiszik, B. J.; Jones, A. R.; Sottos, N. R.; White, S. R., Microencapsulation of gallium–indium (Ga–In) liquid metal for self-healing applications. *J. Microencapsul.* **2014,** *31* (4), 350-354.
73. Milne, G. W., *Gardner's commercially important chemicals: synonyms, trade names, and properties*. John Wiley & Sons: 2005.
74. Zhong, Y. J.; Guo, Q. G.; Li, S. Z.; Shi, J. L.; Liu, L., Thermal and mechanical properties of graphite foam/Wood's alloy composite for thermal energy storage. *Carbon* **2010,** *48* (5), 1689-1692.
75. Zhong, Y. J.; Guo, Q. G.; Li, L.; Wang, X. L.; Song, J. L.; Xiao, K. S.; Huang, F. Q., Heat transfer improvement of Wood's alloy using compressed expanded natural graphite for thermal energy storage. *Solar Energy Materials and Solar Cells* **2012,** *100*, 263-267.
76. Tran, N.; Zhao, W. Y.; Carlson, F.; Davidson, J. H.; Stein, A., Metal Nanoparticle-Carbon Matrix Composites with Tunable Melting Temperature as Phase-Change Materials for Thermal Energy Storage. *Acs Appl Nano Mater* **2018,** *1* (4), 1894-1903.
77. Navarrete, N.; Mondragon, R.; Wen, D. S.; Navarro, M. E.; Ding, Y.; Julia, J. E., Thermal energy storage of molten salt-based nanofluid containing nano-encapsulated metal alloy phase change materials. *Energy* **2019,** *167*, 912-920.
78. Nomura, T.; Zhu, C.; Sheng, N.; Saito, G.; Akiyama, T., Microencapsulation of Metal-based Phase Change Material for High-temperature Thermal Energy Storage. *Scientific Reports* **2015,** *5*.
79. Nomura, T.; Sheng, N.; Zhu, C. Y.; Saito, G.; Hanzaki, D.; Hiraki, T.; Akiyama, T., Microencapsulated phase change materials with high heat capacity and

high cyclic durability for high-temperature thermal energy storage and transportation. *Applied Energy* **2017,** *188*, 9-18.

80. Nomura, T.; Yoolerd, J.; Sheng, N.; Sakai, H.; Hasegawa, Y.; Haga, M.; Saito, G.; Akiyama, T., Microencapsulation of eutectic and hyper-eutectic Al-Si alloy as phase change materials for high-temperature thermal energy storage. *Solar Energy Materials and Solar Cells* **2018,** *187*, 255-262.

81. Sheng, N.; Zhu, C. Y.; Saito, G.; Hiraki, T.; Haka, M.; Hasegawa, Y.; Sakai, H.; Akiyama, T.; Nomura, T., Development of a microencapsulated Al-Si phase change material with high-temperature thermal stability and durability over 3000 cycles. *Journal of Materials Chemistry A* **2018,** *6* (37), 18143-18153.

82. Nomura, T.; Yoolerd, J.; Sheng, N.; Sakai, H.; Hasegawa, Y.; Haga, M.; Akiyama, T., Al/Al_2O_3 core/shell microencapsulated phase change material for high-temperature applications. *Solar Energy Materials and Solar Cells* **2019,** *193*, 281-286.

83. He, F.; Chao, S.; He, X. D.; Li, M. W., Inorganic microencapsulated core/shell structure of Al-Si alloy micro-particles with silane coupling agent. *Ceramics International* **2014,** *40* (5), 6865-6874.

84. He, F.; Song, G. P.; He, X. D.; Sui, C.; Li, M. W., Structural and phase change characteristics of inorganic microencapsulated core/shell Al-Si/Al_2O_3 micro-particles during thermal cycling. *Ceramics International* **2015,** *41* (9), 10689-10696.

85. He, F.; Sui, C.; He, X.; Li, M., Comparison of structure and phase change characteristic of microencapsulated core/shell Al–Si alloy microparticles synthesized by two methods. *Journal of Sol-Gel Science and Technology* **2015,** *76* (1), 1-10.

86. Li, K. Z.; Gu, Z. H.; Zhu, X.; Wei, Y. G.; Wang, H., Facile Synthesis of Al@Al_2O_3 Microcapsule for High-Temperature Thermal Energy Storage. *Acs Sustainable Chemistry & Engineering* **2018,** *6* (10), 13226-13236.

87. Sheng, N.; Zhu, C. Y.; Sakai, H.; Akiyama, T.; Nomura, T., Synthesis of Al-25 wt% Si@Al_2O_3@Cu microcapsules as phase change materials for high temperature thermal energy storage. *Solar Energy Materials and Solar Cells* **2019,** *191*, 141-147.

88. Muta, H.; Kurosaki, K.; Uno, M.; Yamanaka, S., Thermoelectric properties of constantan/spherical SiO_2 and Al_2O_3 particles composite. *J. Alloys Compd.* **2003,** *359* (1), 326-329.

Chapter 2.

Porous SiO_2 Spheres Encapsulated Sn Nanoparticles for Thermal Energy Storage

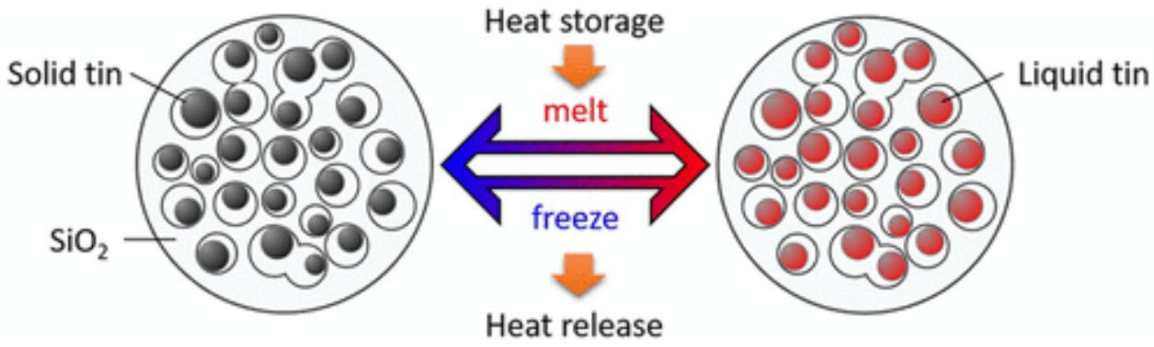

Abstract

We report a facile method for preparing a silica (SiO_2) based material containing Sn nanoparticles (NPs) distributed inside for enhancing the thermal cyclic stability of the inserted Sn NPs. Absorption of a Sn precursor, *i.e.*, an aqueous $SnCl_2$ solution into a mesoporous SiO_2 matrix resulted in confining the Sn precursor into a mesoporous SiO_2 matrix. Hydrogen thermal reduction of the above composite yielded Sn nanoparticles of *ca.* 30 nm uniformly distributed inside porous SiO_2 (p-SiO_2) spheres: Sn NPs@p-SiO_2. Our investigation of the transformation of the porous SiO_2 structure to hold Sn NPs revealed that the process was closely related to the transformation of the amorphous hydrolyzed Sn precursor into Sn oxides followed by, probably, the rearrangement of the SiO_2 matrix via its interaction with the melting Sn. This led to the formation of stable Sn NPs@p-SiO_2. The SiO_2 matrix effectively prevented the coalescence of the Sn NPs and the obtained product exhibited negligible changes in melting behavior during 2^{nd} -100^{th} cycle of freeze-melt cycle test.

2.1 Introduction

Low melting point metals are promising materials that can be used as phase change materials for heat storage and thermal management.[1] Rapid thermal energy transfer can be achieved due to the high thermal conductivity of the metallic heat storage media. The high density of the metal also contributes to the high-volume density of heat storage.[2-3] One way of applying low melting point metals for heat transfer in cooling systems of electronic devices, is to use metal nanoparticles (NPs) or convert

them into nanofluids by dispersing metal NPs into thermally stable liquids, to obtain good fluidity and thermal behavior for heat transfer.[4-8]

However, during the heat storage and release operation, phase change metal NPs are sintered causing difficulties regarding the colloidal stabilization of nanofluids, thus leading to bad cyclic stability of heat storage. The key to avoid metal NPs coalescence is to isolate them. There are several strategies to solve this problem: one method involves introducing an inert shell or layer outside the pre-synthesized metal NPs.[9-11] Cingarapu *et al.* synthesized and studied the thermal properties of silica (SiO_2) coated Sn NPs. Another method involves inserting metal NPs into an inert matrix.[12-13] Liu *et al.* used pre-synthesized Bi nanocrystals to prepare nanocomposites where Bi NPs were evenly embedded in an Ag matrix[14] and a polyimide (PI) resin matrix.[15] However, both methods require the complex pre-synthesis of metal NPs.

In our study, we chose metallic Sn NPs as the phase change material and mesoporous SiO_2 spheres as the matrix for isolating Sn NP. Sn NPs were often prepared by chemical reduction[16-18] but in our case, Sn NPs formed inside the matrix by thermal hydrogen reduction. There are several advantages using porous SiO_2 (p-SiO_2) spheres. First, p-SiO_2 spheres can easily undergo surface modifications for good dispersion in both polar and non-polar solvents, which allows to fabricate nanofluids. In addition, as matrix materials, mesoporous SiO_2 spheres have various useful characteristics including controllable morphology and uniform mesopores providing a low-cost permeable structure for loading metal precursors.[19] Moreover, our facile synthesis avoided the complex high-cost synthesis of metal NPs. We proposed encapsulating

isolated, individual Sn NPs in p-SiO_2, to protect them from sintering during melt-freeze cycles. Our strategy was based on impregnating a Sn salt into pre-prepared SiO_2 spheres followed by reducing the impregnated Sn precursor to metallic Sn. Our results indicated the successful confinement of Sn NPs into p-SiO_2 spheres, which resulted in a stable structure for multiple melting-cooling thermal cycles. In addition, we elucidated the formation of the Sn NPs in p-SiO_2 for the first time.

2.2 Experimental

2.2.1 Chemicals

Tetraethyl orthosilicate (TEOS, min. 98%), was purchased from Wako, Japan. Hexadecyltrimethylammonium bromide (CTAB, G.R.) was supplied from TCI, Japan. Anhydrous tin(II) chloride, $SnCl_2$ (min. 98%), ammonia solution (min. 28%), ethanol, and 1-propanol (99.5% purity) were purchased from Junsei, Japan. All chemicals were used without further purification. Water was purified using a PureLabo system (Organo/ELGA, > 18 MΩ).

2.2.2 Preparation of p-SiO_2 spheres.

We prepared p-SiO_2 spheres according to the method reported by Yu *et al*.[20] In brief, 4.8 g CTAB was dissolved in a mixture of 160 mL ethanol and 240 mL H_2O. Subsequently, 3.2 mL ammonia solution and 6.4 mL TEOS were added to the surfactant solution. The reaction mixture was stirred for 4 h. Furthermore, the p-SiO_2 spheres were

isolated by centrifugation at 8000 rpm (5800 ×g) for 10 min and washed with 1-propanol three times. Finally, the powder was vacuum dried overnight.

2.2.3 Synthesis of Sn NPs@p-SiO_2

In a typical synthesis, 0.1 g of the as prepared p-SiO_2 was used as SiO_2 matrix and dispersed in 4 mL H_2O. 3.04 g $SnCl_2$ was added to the dispersion and the dispersion was sonicated for 30 min, then stirred for 6 h. The obtained Sn precursor loaded p-SiO_2 was collected by centrifugation at 10 000 rpm (9100 × g) for 10 min and washed with 1-propanol for three times before being vacuum dried for 30 min. The white powder was transferred to an alumina boat and reduced in a 3% H_2/N_2 flow at 550°C for 6 h in a tube furnace (TMF-500N, As one, Japan). After cooling down to 25°C, the black Sn NPs@p-SiO_2 powder was collected. Reduction was conducted under various temperatures from 260 to 650°C to study the formation of Sn NPs@p-SiO_2. The largest quantity of Sn NPs from one pot synthesis at 550°C for 6 h was 9.2 mg and the yield was 63.6%.

2.2.4 Characterization

The morphology of the produced Sn confined inside mesoporous SiO_2 was examined using transmission electron microscope (TEM, JEOL JEM-2000FX, 200 kV). The crystal and phase structures of the products were characterized using X-ray diffraction (XRD, Rigaku Miniflex II X-ray diffractometer, Cu Kα radiation, $\lambda = 1.5418$ Å), while X-ray fluorescence spectrometry (XRF, JSX-3100RII, JEOL) was used to

estimate the element composition. The mean crystalline size was estimated using XRD peak broadening based on the Scherrer formula. The chemical states of Sn in the mesoporous SiO_2 matrix and depth profile were characterized using X-ray photoelectron spectroscopy (XPS, JEOL photoelectron spectrometer, JPS-9200, monochromatic Al-Kα). Thermogravimetric differential thermal analysis (TG-DTA) was performed using a Shimadzu DTG-60H instrument to study the melting point of Sn NPs as well as the amount of Sn inside the SiO_2 matrix. The gas used for TG-DTA was a mixture of 3% H_2 and N_2 at a flow rate of 100 $mL \cdot min^{-1}$ and heating rate was set as 5°C$\cdot min^{-1}$. The melt-freeze cyclic test was performed in a differential scanning calorimeter (DSC) (DSC 2500, TA Instrument). The gas used for DSC was N_2 (99.995%), and the flow rate was set as 50 $mL \cdot min^{-1}$.

2.3 Results and Discussions

2.3.1 Preparation strategy of Sn NPs@p-SiO_2

The preparation procedure for the Sn NPs@p-SiO_2 structure is illustrated in Scheme 1. Mesoporous SiO_2 spheres were synthesized first based on a well-established method.[20] Furthermore, $SnCl_2$ was impregnated into the newly prepared mesoporous SiO_2 spheres via ultrasonication and stirring. Washing the p-SiO_2 spheres with deionized water removed the extra Sn precursor from outside the spheres. Finally, reducing the Sn precursor encapsulated into the p-SiO_2 spheres using a 3% H_2/N_2

atmosphere converted the white solid into black powder, *i.e.*, the final product Sn NPs@p-SiO_2.

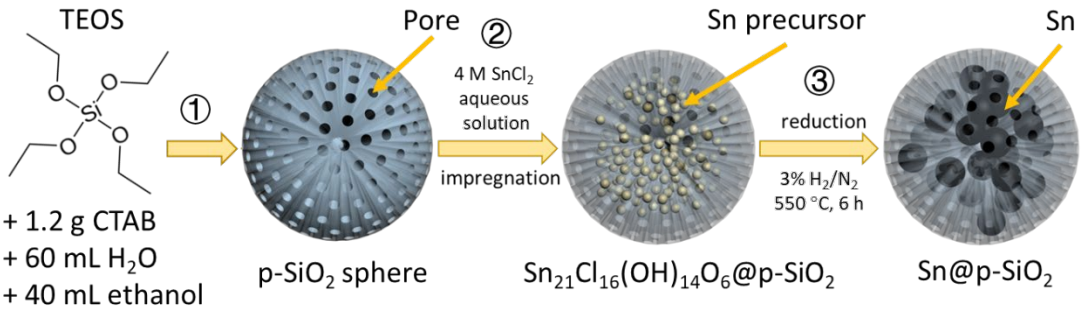

Scheme 2.1 Preparation of Sn NPs@p-SiO_2.

Step 1: Synthesis of p-SiO_2 spheres as structure matrix; Step 2: Impregnation of the Sn precursor; Step 3: Reduction of the Sn precursor inside the SiO_2 matrix to obtain Sn NPs embedded into p-SiO_2.

2.3.2 Confirmation of the obtained Sn NPs@*p*-SiO_2 structure

The XRD pattern of the as-prepared p-SiO_2 indicated an amorphous structure. The broad peak between 20 and 30° indicated the existence of amorphous SiO_2. After reducing the Sn precursor loaded p-SiO_2 spheres using 3% H_2/N_2, we were able to index all the diffraction peaks of the obtained sample (Figure 2.1) to tetragonal metallic Sn (JCPDS No. 04-0673). Based on the line broadening, Sn with a 36.5 nm mean crystalline size was obtained.

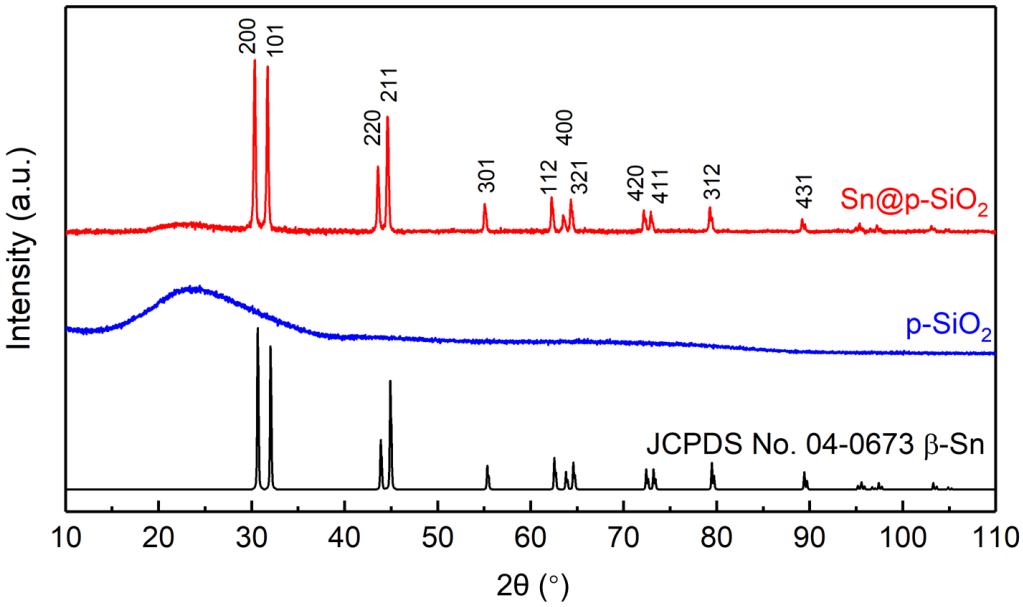

Figure 2.1 XRD patterns of Sn NPs@p-SiO_2.

Sn NPs@p-SiO_2 (red) and p-SiO_2 (blue).

As can be seen in Figure 2.2(a), TEM analysis showed that the as prepared monodispersed p-SiO_2 had a size of *ca.* 400 nm. The size of the SiO_2 spheres remained unchanged after reducing the Sn precursor loaded into p-SiO_2 using 3% H_2/N_2 (Figure 2.2(b)). The TEM image contrast in Figure 2.2(b) suggested that Sn NPs exist in the p-SiO_2 matrix, as Sn has a higher density compared with SiO_2. Figure 2.2(b) and (d) also reveals that the Sn NPs@p-SiO_2 sample contained Sn NPs with an average size of approximately 30 nm which is 6.5 nm smaller than the crystalline size estimated from

XRD line broadening. The difference between these two measurements can be caused by the stronger contribution of large size particle (as shown in TEM) to the diffraction signal even though they present in lower population. In addition, coalescence of unprotected Sn NPs reduced from free Sn precursor outside p-SiO_2 structure can contribute to the increase of the mean crystalline size from XRD data. The selected area electron diffraction pattern (SAED) (Figure 2.2(c)) shows diffraction spots attributed to the diffraction from (200), (211), (301), and (112) lattice planes of tetragonal metallic Sn, indicating the existence of crystallized Sn NPs. This was in good agreement with the XRD results. We tried to etch SiO_2 and observe Sn NPs themselves. However, the etching using HF or concentrated 10 M NaOH aqueous solution also harms the Sn NPs as Sn is reactive in water and the formed tin oxides and tin hydroxide can be subsequently dissolved in the etching solutions. When the p-SiO_2 in Sn NPs@p-SiO_2 was partially etched by using concentrated sodium hydroxide solution at 25°C for 10 h (Figures S2.1a-c), a decrease in average size of Sn NPs (21.1 nm, Figure S2.1d) was observed besides some big NPs (100 nm).

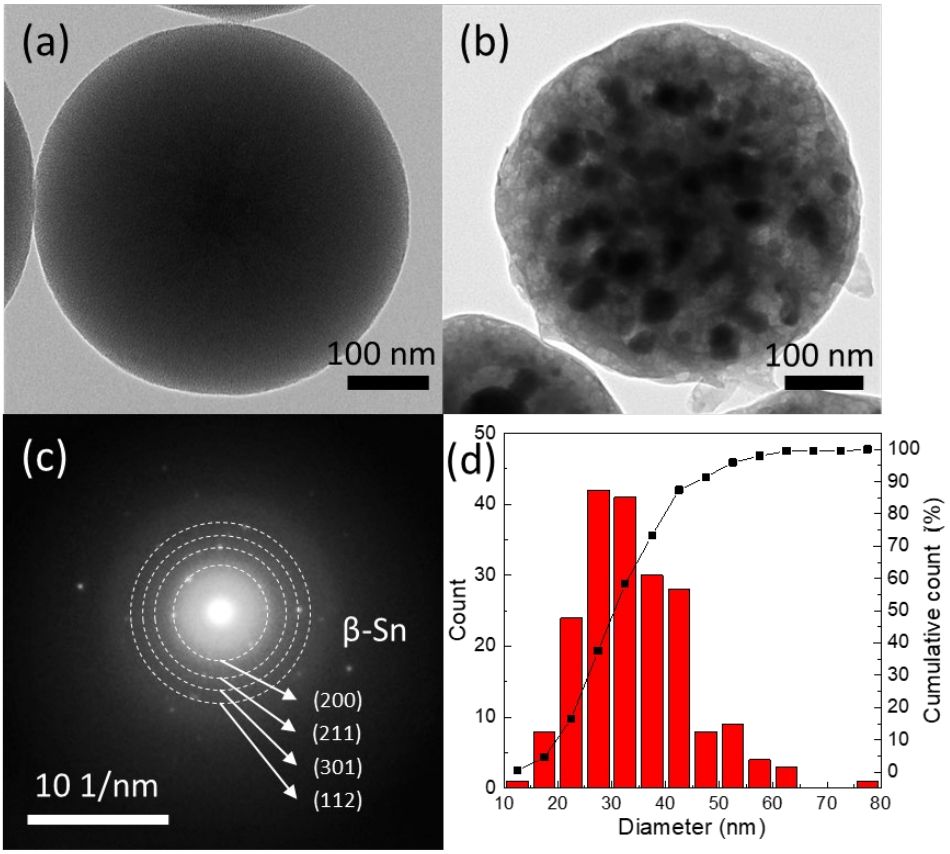

Figure 2.2 Morphology of as-synthesized p-SiO_2 spheres and Sn NPs@p-SiO_2

TEM images of (a) as-synthesized p-SiO_2 spheres and (b) Sn NPs@p-SiO_2, (c) SAED pattern of Sn NPs@p-SiO_2, and (d) size histogram of Sn NPs in p-SiO_2.

We performed XPS analyses to investigate the spatial relationship between the Sn NPs and porous SiO_2 spheres. Meanwhile, the valence state of Sn and composition of Sn NPs@p-SiO_2 were also studied. Figure 2.3(a) shows the wide scan spectrum of the sample, where only the peaks corresponding to Sn, O, C, and Si are clearly observed. The C peak was attributed to the carbon tape used for preparing the XPS sample and carbonization products formed during the 3% H_2/N_2 reduction at 550°C. Figure 2.3(b) and (d) show the high-resolution XPS spectra of Sn 3d at the surface (0

nm depth) and after Ar etching to 210 nm depth, respectively. The two separated peaks centered around 486.4 and 494.8 eV correspond to the binding energies of Sn $3d_{5/2}$ and Sn $3d_{3/2}$ are respectively deconvoluted into four peaks centered at 485.3 and 487.2 eV for metallic Sn and at 493.6 and 495.3 eV for SnO_2. The weaker SnO_2 peak shown in the narrow scan after Ar etching to a 210 nm depth indicates less oxidation for Sn inside the SiO_2 structure than compared to the Sn near the surface. This result was further confirmed by the peak shift from SnO_2 to metallic Sn as the depth of the Ar etching increased as shown in Figure 2.3(c).

The depth profile in Figure 2.4(a) shows the atomic percentage ratio between Si and Sn in the Sn NPs@p-SiO_2 sample. The Si and Sn contents were stable as the depth increased indicating the uniform distribution of the Sn precursor inside the SiO_2 matrix except for a slight decrease in the Sn content near the surface. This was probably due to the loss of precursor during purification before reduction. Our data indicated a 12.2 at% Sn. Figure 2.4(b) shows the atomic ratio of Sn and SnO_2 calculated from the XPS narrow scan. The lowest amount of metallic Sn content: 28.4 at%, was obtained near the surface of the SiO_2 matrix (before etching), whereas we recorded the maximum percentage of metallic Sn: 54.9 at% toward the center of the p-SiO_2 sphere. As the etching depth increased, the content of SnO_2 decreased, indicating that the Sn near the surface of the SiO_2 matrix was more severely oxidized than that located near the center of the SiO_2 matrix. Using the TGA results for Sn NPs@p-SiO_2 (Figure S2.2), the molar ratio of Sn:Si in the Sn NPs@p-SiO_2 sample was calculated to be 17.1:82.9 (weight

ratio Sn:SiO_2 = 29.0:71.0) (see Supporting Information (SI)). This was close to the molar ratio of Sn:Si based on the XPS results in Figure 2.4(a).

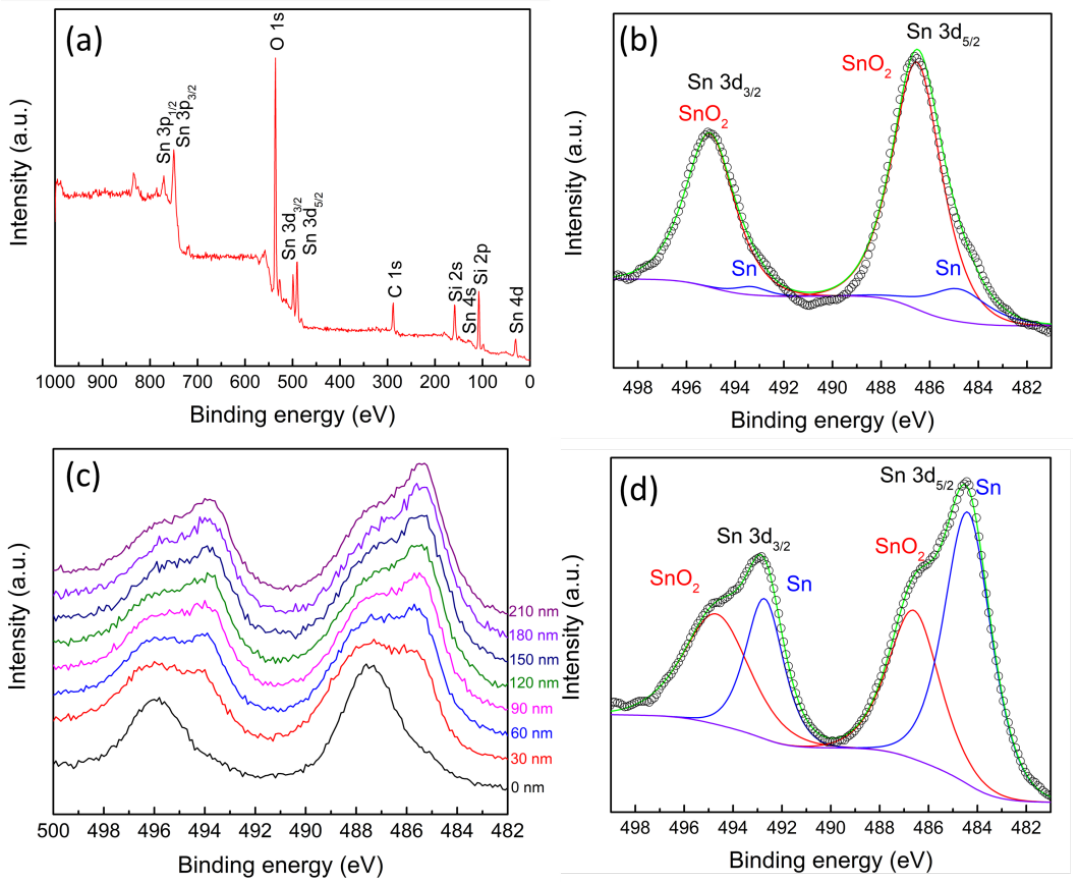

Figure 2.3 XPS image of Sn NPs@p-SiO_2.

(a) wide scan, (b) and (d) narrow scan of Sn 3d at the particle surface and after Ar etching to a depth up to 210 nm, respectively, and (c) depth profile for the Sn 3d region.

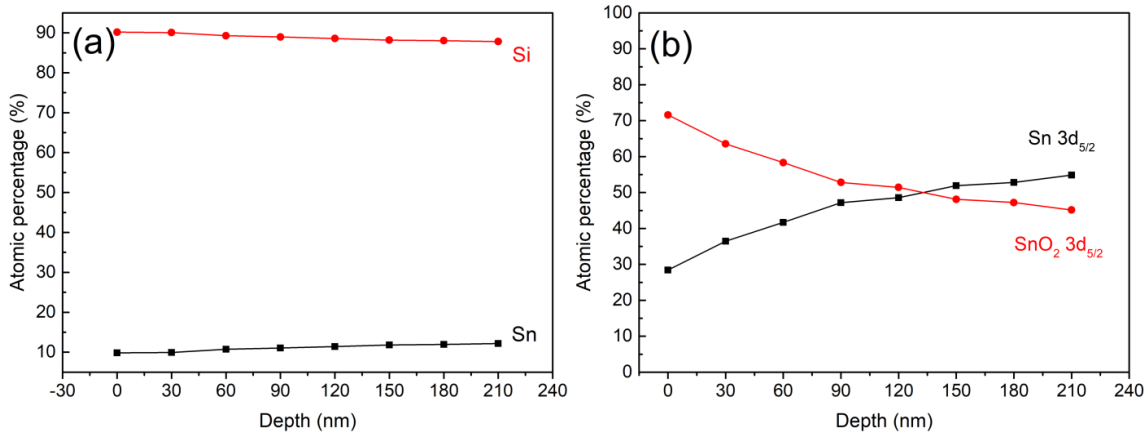

Figure 2.4 XPS composition depth profile of Sn@p-SiO_2.

Composition depth profile: (a) Si and Sn, (b) Sn and SnO_2.

2.3.3 Formation mechanism of the Sn NPs@p-SiO_2 structure

Our XRD, TEM, SAED, and XPS depth profiles data demonstrated that Sn NPs were successfully embedded into p-SiO_2. We also observed that when 30 nm Sn NPs formed inside p-SiO_2, the pore structure of the mesoporous SiO_2 likely changed to larger voids to hold the Sn NPs whereas the SiO_2 particles were not broken (Figure 2.2(a) and (b)). To find out the reason for the changes in the morphology of p-SiO_2, we first investigated the changes underwent by SiO_2 during thermal annealing. The as-prepared mesoporous SiO_2 spheres were annealed under the same condition used for the synthesis of Sn NPs@p-SiO_2: 550°C, 6 h, and 3% H_2/N_2 gas flow. From the TEM images in Figure S2.3, no morphology change (big voids) was observed compared to the as prepared p-SiO_2 shown in Figure 2.2(a). Thus, we excluded the thermal

instability of the mesoporous SiO_2 itself during the H_2/N_2 thermal reduction as the reason for the changes in the p-SiO_2 structure.

The XRD patterns and TEM images of the samples obtained after loading the Sn precursor into p-SiO_2 are shown in Figures S2.4 and S2.5, respectively. All the clear peaks in the XRD pattern (Figure S2.4) can be indexed to $Sn_{21}Cl_{16}(OH)_{14}O_6$. This was attributed to the hydrolysis of $SnCl_2$ in H_2O and the embedding of the hydrolysis product into p-SiO_2. No morphological change was observed for p-SiO_2 containing Sn precursor compared with the as-prepared p-SiO_2. Therefore, it was reasonable to believe that the change in pore structure did not happen during the precursor loading step. During impregnation, we observed the formation of white floc upon mixing the $SnCl_2$ and mesoporous SiO_2 spheres suspension. The reason for the floc formation can be directly attributed to the change in the pH value of the solution. The hydrolysis of $SnCl_2$ resulted into a solution with a low pH of approximately 0.8. After adding p-SiO_2, the pH increased to 3.4. This pH was close to the pH point of zero charge (pzc) of the hydroxylated surface of SiO_2,[22] which caused the flocculation of SiO_2 to occur. Furthermore, Sn^{2+} was adsorbed onto the surface of the SiO_2 mesopores due to the negative charge of SiO_2 attracting and trapping Sn^{2+} inside the SiO_2 matrix. In addition, covalent bonds could also form between Sn^{2+} and the silanol groups on the hydroxylated SiO_2 surface.[23] Such interactions are important for the impregnation of the Sn precursor into p-SiO_2. By comparison, we used ethanol as solvent to impregnate $SnCl_2$ into p-SiO_2. There were no obvious differences in the pore structure of p-SiO_2 before (Figure 2.2(a)) and after the reduction of $SnCl_2$ (Figure S2.6). However, it was

difficult to keep $SnCl_2$ inside the SiO_2 matrix when ethanol was used. Moreover, $SnCl_2$ was easily washed away during the purification step.

From the above results, we concluded that the change in the pore structure of p-SiO_2 containing Sn NPs occurred during the reduction of the Sn precursor inside p-SiO_2 under 3% H_2/N_2 at high temperature (step 3 in Scheme 1). To understand the reduction of the Sn precursor in p-SiO_2, TG-DTA measurements in a 3% H_2/N_2 atmosphere were performed on the Sn precursor loaded p-SiO_2 spheres using a 100 $mL \cdot min^{-1}$ gas flow rate. The endothermal valleys (Figure 2.5) centered at 165 and 190°C indicated the evaporation of the absorbed water and decomposition of $Sn_{21}Cl_{16}(OH)_{14}O_6$ by losing crystal water (Eq. 1), respectively. The endothermal valley centered at 295°C may represent the further decomposition of $Sn_{21}Cl_{16}(OH)_{14}O_6$.[24] A significant mass loss (35 %) was detected from 25 to 630°C. The decomposition and reduction of the Sn precursor, *i.e.*, $Sn_{21}Cl_{16}(OH)_{14}O_6$, can result in a 26.5 % mass loss ($Sn_{21}Cl_{16}(OH)_{14}O_6 \rightarrow Sn$) after reduction. Beside the Sn precursor, our sample also contained SiO_2. Therefore, a 35% mass loss during the reduction of Sn in SiO_2, implied the presence of other amorphous Sn precursors in the sample beside $Sn_{21}Cl_{16}(OH)_{14}O_6$ after impregnation. We detected a significant mass loss at the same temperature (300°C) in the TG-DTA results for the anhydrous $SnCl_2$ powder in N_2 (Figure S2.7). We believe that the initial impregnated amorphous Sn precursors may be lost when increasing the temperature from 300 to 400°C for the TG-DTA measurements. The Sn:Si atomic ratio determined using the XRF results also became smaller after hydrogen reduction. Sn reduction occurred in the 300 – 400°C range as indicated by the endothermic peak

centered at 340°C. We noticed that in equations **1–3**, which describe the decomposition of the Sn precursor in N_2 atmosphere, the chemical valence of Sn, *i.e.*, 2, did not change. Therefore, we concluded that when a H_2/N_2 mixture was used, the decomposition (Eq. **3**) and reduction of Sn could occur simultaneously (300 – 400°C).

$$Sn_{21}Cl_{16}(OH)_{14}O_6 \xrightarrow[200\ ^\circ C]{-\ 7\ H_2O} [Sn_{21}Cl_{16}O_{13}], \quad (1)$$

$$[Sn_{21}Cl_{16}O_{13}] \xrightarrow[232\ ^\circ C]{-\ 4.3\ (\pm\ 0.1)\ SnCl_2} 1.86\ Sn_9Cl_4O_7, \quad (2)$$

$$1.86\ Sn_9Cl_4O_7 \xrightarrow[452\ ^\circ C]{-\ 3.7\ (\pm\ 0.1)\ SnCl_2} 13\ SnO, \quad (3)$$

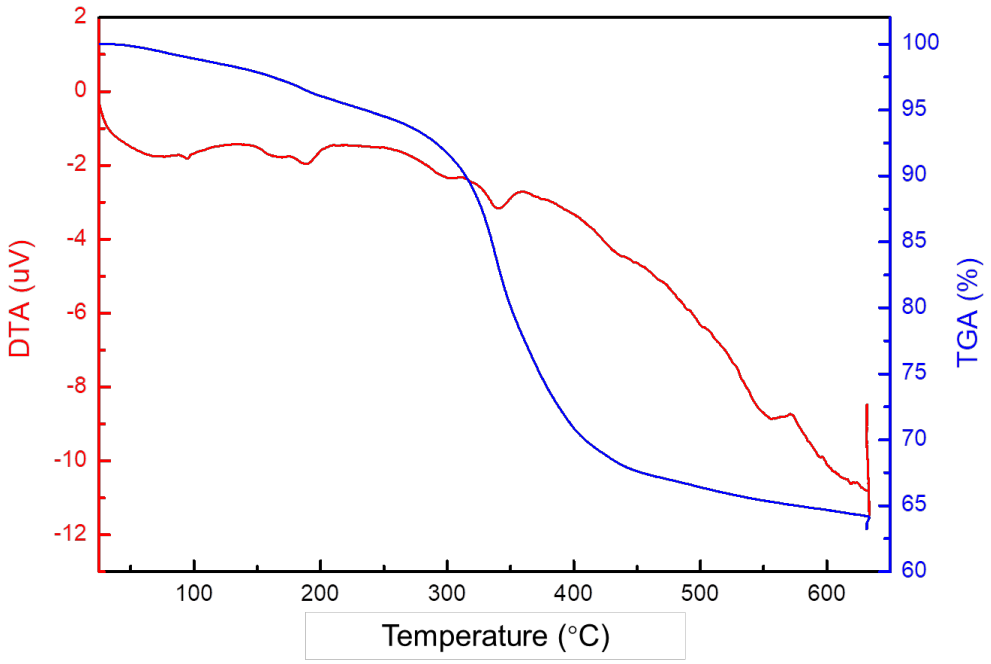

Figure 2.5 TG-DTA results of the annealing of the Sn precursor loaded p-SiO_2 under 3% H_2/N_2 gas flow.

The mass percentage at 25°C was set as 100%.

Based on the TG-DTA results, the reduction of the Sn precursor embedded into p-SiO_2 at different reduction temperatures, *i.e.*, 260 and 330°C (no reduction of Sn precursor can occur), 360°C (reduction can occur), and 400 – 630°C (reduction must occur), was performed for 6 h. The XRD results and TEM images of the products with different reduction temperatures are shown in Figures 2.6 and 2.7, respectively. We found that after annealing at 260°C, all the XRD peaks that were indexed to $Sn_{21}Cl_{16}(OH)_{14}O_6$ disappeared and no peaks indicating the amorphous intermediate materials phase were observed. The transition from crystalline $Sn_{21}Cl_{16}(OH)_{14}O_6$ (as-prepared at 25°C) to amorphous materials (260°C) was due to the decomposition of the precursor, *i.e.*, losing water, HCl, etc., as was indicated by the DTA and TG results. When the reduction temperature was increased to 330°C, peaks that were indexed to SnO_2 were observed, indicating the formation of crystalline SnO_2. Combining the TGA results (Figure 2.5), we concluded that when the reduction temperature was lower than 330°C, the hydrogen thermal reduction of Sn could not have happened or was just in the very beginning stages. Thus, the formation of SnO_2 (crystalline phase at different annealing temperatures as showed in Table S1) may be related to the crystallization of the amorphous oxides formed at lower temperatures or the further decomposition of the amorphous Sn precursor materials mentioned above. When performing the reduction at 360°C, the XRD peaks that were indexed to SnO_2, SnO, and tetragonal metallic Sn overlapped. When the reduction temperature was ≥ 460°C, all the XRD peaks were indexed to tetragonal metallic Sn. We calculated the crystal size of metallic Sn prepared at different reduction temperatures (360 – 630°C) using Scherrer equation. The results

showed that the crystal size of Sn increased with the increase in the reduction temperature (Figure S2.8).

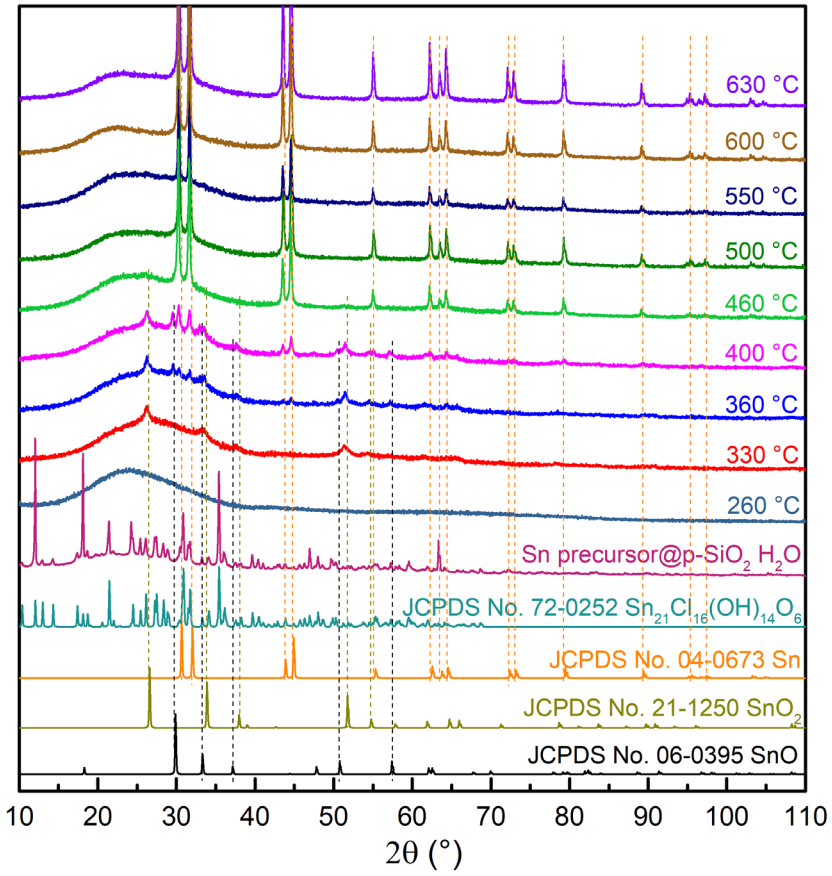

Figure 2.6 XRD results of products at different reduction temperatures.

We observed that at 260°C (amorphous Sn precursor materials) there was no change in the morphology of the product (Figures 2.7(a)) compared with p-SiO_2 containing Sn precursors at 25°C (Figure S2.5). However, when the reduction temperature was set at 330 ºC, significant morphology changes occurred as showed in

the TEM image (Figure 2.7(b)). At this state, only SnO_2 peaks appeared in the XRD pattern. This indicated that the decomposition of the amorphous Sn precursor materials to form crystalline SnO_2 was related to the changes in the pore structure of p-SiO_2. Further increasing the reduction temperature resulted in the formation of metallic Sn and the increase in its particle size (Figures 2.6 and 2.7). Simultaneously, the pores became likely bigger as observed in the TEM images in Figures 2.7(c) – (f). Based on these results, we considered that the reduction of SnO and SnO_2 and the melting and growth of metallic Sn in p-SiO_2 further influenced the mesopore structure and widened the pores in p-SiO_2. It is possible that during the formation of Sn oxides and Sn, the condensation and re-arrangement of SiO_2 inside the p-SiO_2 occurred and voids formed to hold Sn NPs, while the p-SiO_2 spheres were not broken. We considered that the re-arrangement of SiO_2 in p-SiO_2 was possible and important for the formation of Sn NPs in p-SiO_2 and the modification of the pore structure. We observed that after calcinating the as-prepared p-SiO_2 at 550°C for 6 h in air to remove the hydroxyl on the SiO_2 surface and remained ammonia inside the pore, there were no changes in the morphology of the p-SiO_2 (Figure 2.8(a)). However, after loading the Sn precursor into the annealed p-SiO_2 follow by reduction at 550°C for 6 h in 3% H_2/N_2, the TEM images of the product (Figure 2.8(b) and (c)) showed no obvious morphology (pore structure) changes for the p-SiO_2 sphere whereas Sn NPs of *ca.* 100 nm (darker contrast, as confirmed by SAED Figure 2.8d) formed and distributed outside the SiO_2 spheres. These results suggest that the SiO_2 and the pore structure in the as-prepared p-SiO_2 were strengthened and became rigid/fixed after annealing. The rigid SiO_2 pore-structure

could not be further modified during the decomposition and reduction of the Sn precursors.[25,26] As a result, at high temperature, Sn formed in the pores just melts, exits the pore and grows into bigger Sn NPs leaving the p-SiO_2 particles unchanged. In addition, this may suggest that there could be some interaction between the Sn precursor and as-prepared p-SiO_2 when the temperature increased, which can modify the structure of SiO_2 pores. So far, we did not find any direct evidence for such interaction. The results of our study indicated that the formation of Sn NPs in p-SiO_2 and the change in pore structure of SiO_2 to hold formed Sn NPs with larger size could occur during the decomposition of the amorphous Sn precursor at 330°C, formation and reduction of crystalline SnO_2 and SnO, and interaction of the Sn precursor with SiO_2 which could have led to the re-arrangement of the SiO_2 structure. This mechanism is illustrated in Figure 2.9.

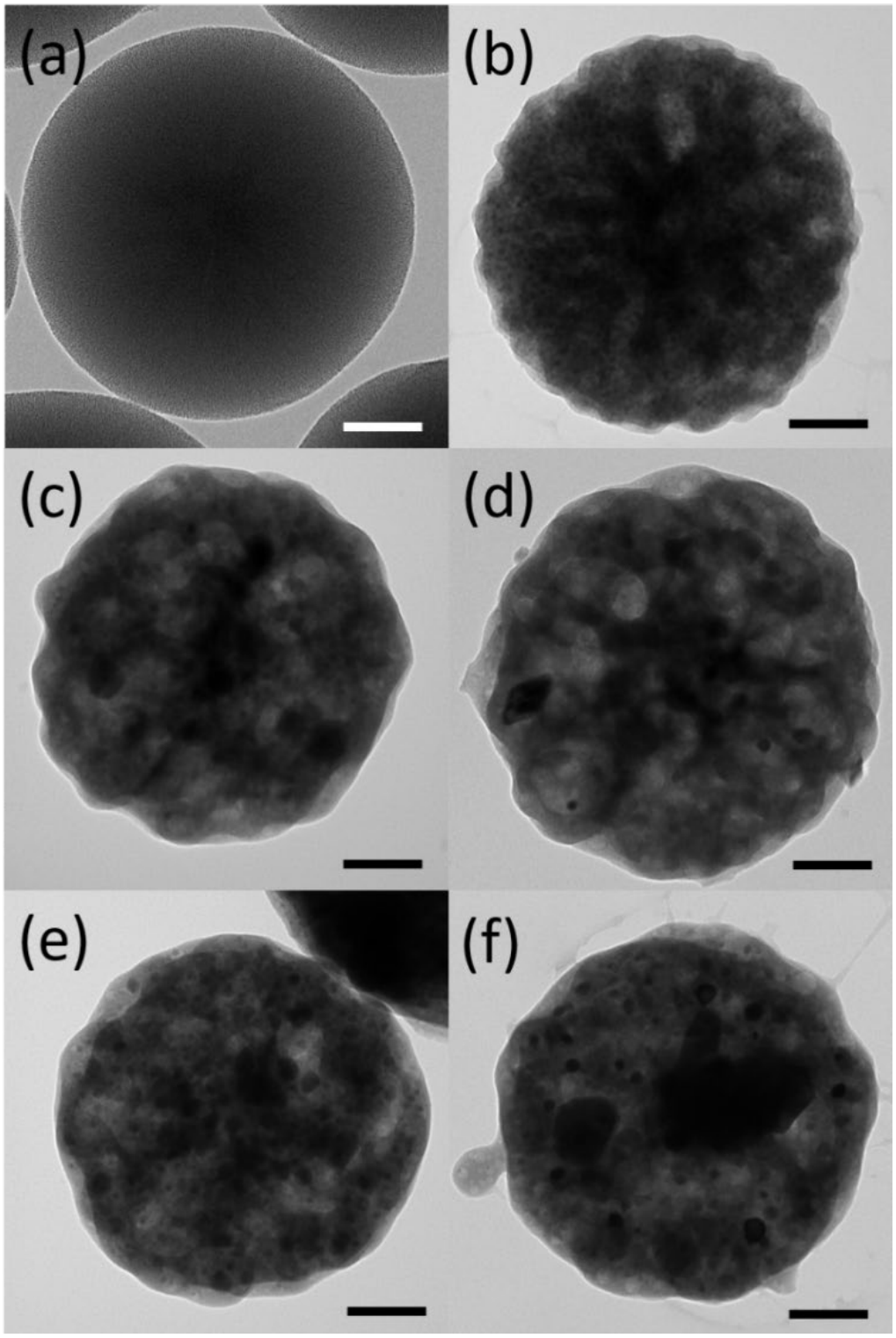

Figure 2.7 TEM images of products obtained at different reduction temperatures.

(a) 260°C, (b) 330°C, (c) 360°C, (d) 400°C, (e) 460°C, and (f) 600°C. All inset scale bars indicate 100 nm.

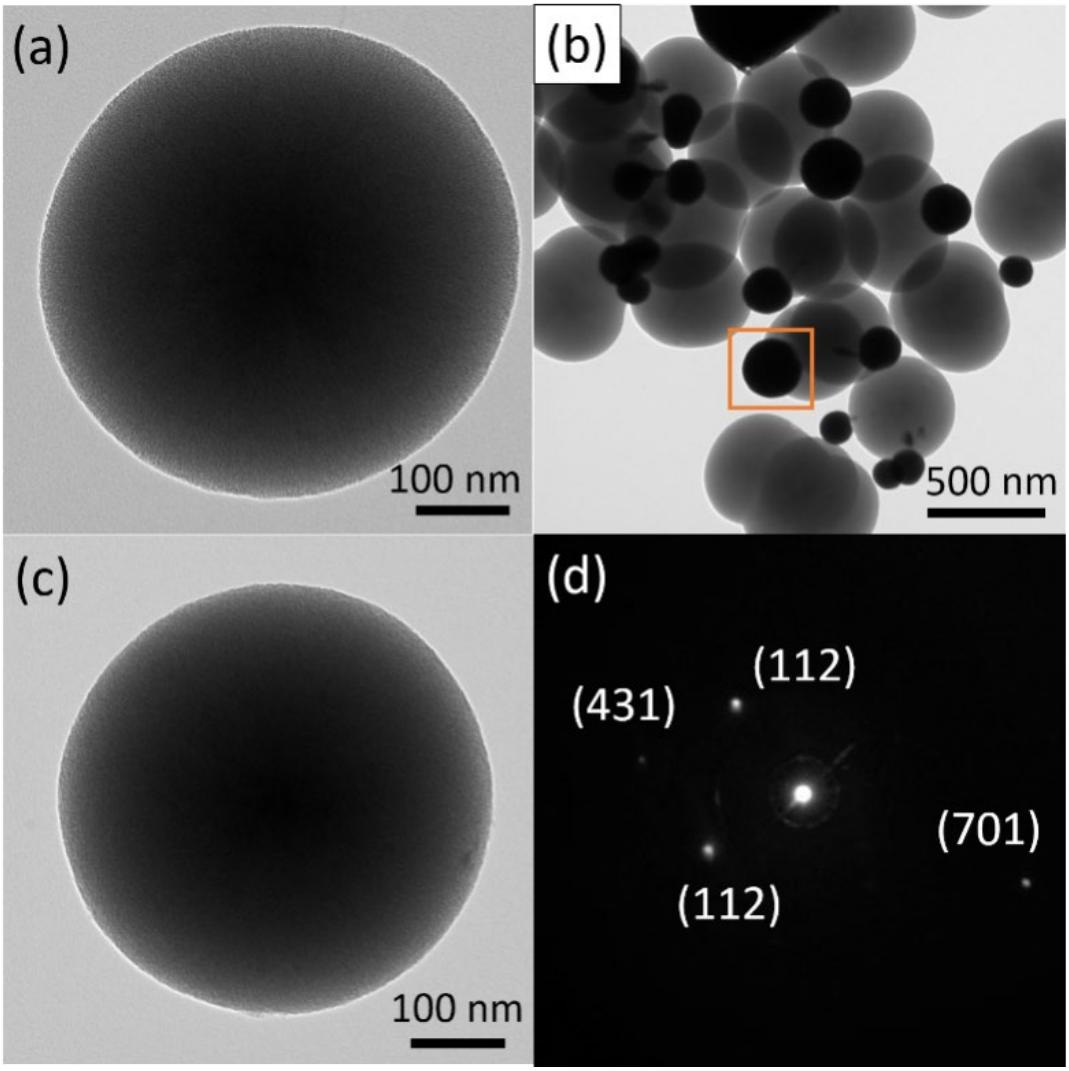

Figure 2.8 Morphology of calcined p-SiO_2 and the products obtained by loading the Sn precursor into calcined p-SiO_2 spheres followed by reduction using 3% H_2/N_2 gas for 6 h.

(a) TEM image of calcined p-SiO_2, (b, c) TEM images of the products obtained by loading the Sn precursor into calcined p-SiO_2 spheres followed by reduction using 3% H_2/N_2 gas for 6 h, and (d) SAED pattern of the black NP shown in the orange rectangle in (b), which was assigned to metallic Sn.

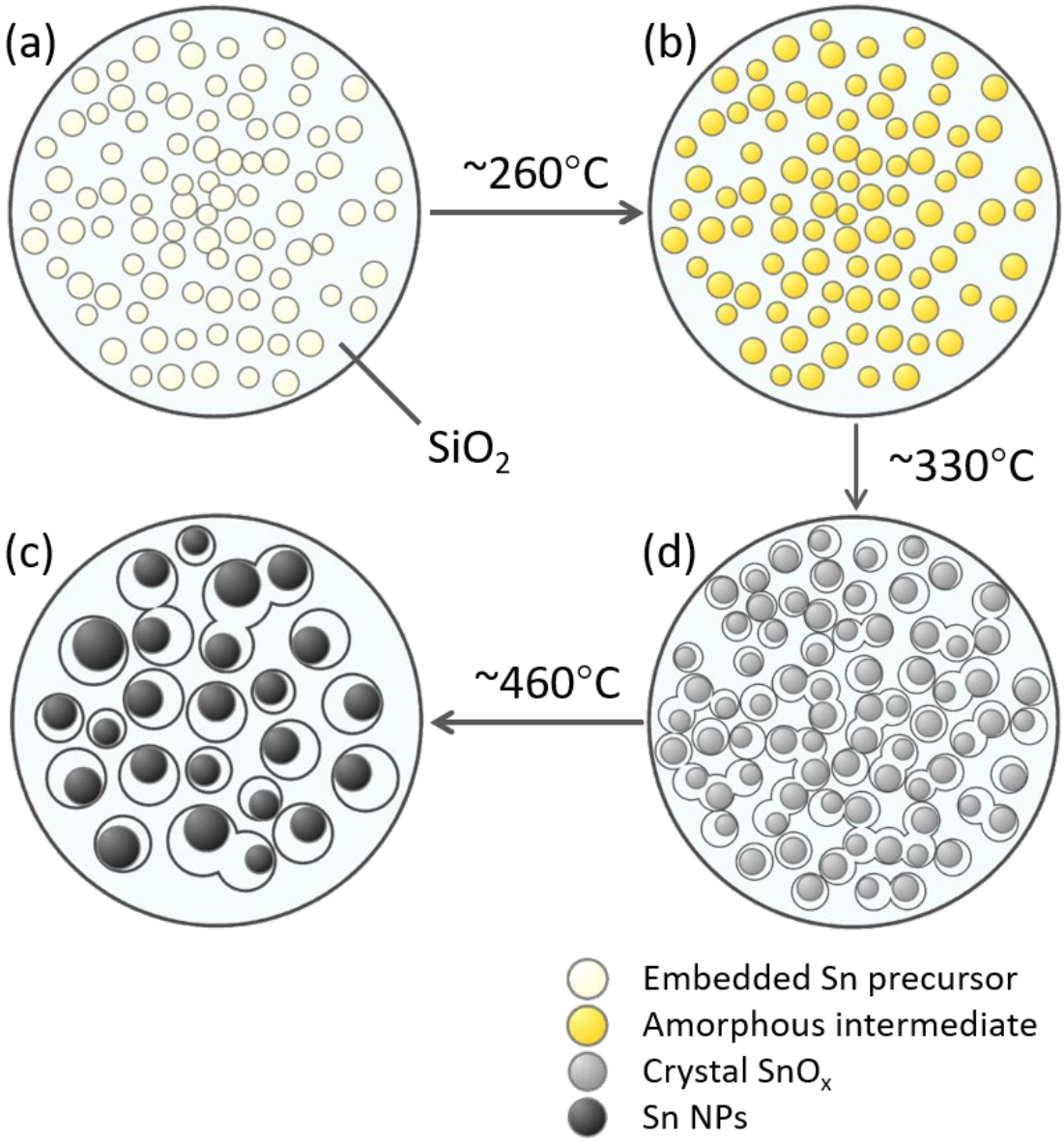

Figure 2.9 Illustration of the formation mechanism of Sn NPs@p-SiO_2.

(a) $Sn_{21}Cl_{16}(OH)_{14}O_6$ and other amorphous Sn precursors were absorbed into p-SiO_2 spheres after the impregnation of the $SnCl_2$ precursor; (b) amorphous Sn precursor was formed after annealing at a temperature below 260°C; (c) crystal Sn oxides, SnO_x where x = 1, 2, formed at ca. 330°C with the change in the pore structure of the p-SiO_2 spheres; (d) SnO_x were reduced and Sn NPs formed inside the p-SiO_2 spheres with the ability to further expand the pore inside the p-SiO_2 spheres.

2.3.4 Thermal Stability

The typical DSC measurement of Sn NPs@p-SiO_2 (synthesized at 550°C, in 3% H_2/N_2) is shown in Figure 2.10. An endothermic peak is observed at approximately 230°C during heating indicating the melting of Sn NPs. The melting temperature was measured as 229.1°C. An exothermic peak ranges from 105 to 140°C during the cooling of Sn NPs in p-SiO_2 were observed. By contrast, peaks centered at 130.5, 142.7 and 160.9°C were observed in the cooling curve for bulk Sn (Figure S2.9). These results indicated the supercooling and the large number of freezing events associated with different temperatures and spatial conditions for Sn NPs in p-SiO_2.[27] Sn NPs confined in p-SiO_2 spheres had different location inside the SiO_2 spheres and a relatively broad size distribution from 10 to 80 nm. This may have resulted into various degrees of supercooling during the freezing period of the thermal cycles. We believe this out of sync cooling could result in a wide slope in the DTA curve.

To investigate the stability of the separated distribution of Sn NPs inside p-SiO_2, 100 melt-freeze thermal cycles were performed in the 100 – 250°C range (Figure 2.10a). The existence of an endothermic peak at the same temperature for all the 100 cycles showed the stability of the Sn NPs@p-SiO_2 structure during melt-freeze cycles (Figure 2.10c). The enthalpy of melting for Sn NPs@p-SiO_2 (Figure 2.10b) was calculated based on the integral of the endothermic peak area as shown in Figure 2.10c, i.e. the enthalpy of melting of the 5th cycle was 7.24 J/g. The drop of the enthalpy from the first cycle (8.46 J/g) to the 2nd one (7.20 J/g) was due to the oxidation by the absorbed air and moisture in the p-SiO_2. From the 2nd cycle, the enthalpy of melting

showed slightly change and ended up at 6.62 J/g after the 100th cycle (Figure 2.10b). The change in enthalpy melting indicated that after 100 cycles there was approximately 8% of Sn was further oxidized compared with that in the 2nd cycle. The enthalpy of melting for only Sn is 55.30 J/g for the first cycle is smaller than that of the bulk Sn (60.6 J/g). This is caused the increase in ratio of number of surface Sn atoms to that in volume of Sn NPs compared with bulk Sn. Thus, the melting enthalpy and the melting temperature of Sn NPs lower than that of the bulk counterpart. Compared with the melting temperature of commercial bulk metallic Sn (230.7°C) (Figure S2.9), the melting temperature calculated using the DSC curve for Sn NPs inside the p-SiO_2 was approximately 229.1°C as shown in Figure 2.10(d). This was consistent with the melting point depression of the NPs. According to the model proposed by S. L. Lai *et al.*, 229.1°C corresponded to the melting temperature of 57.3 nm Sn NPs[28] (see SI), which agrees with the results of the TEM analysis (Figure 2.11(a)). The TEM images of the Sn NPs inside the p-SiO_2 spheres after 20 melt-freeze cycles indicated that Sn NPs with sizes of *ca.* 50 nm still existed (Figure 2.11). These results emphasized that the Sn NPs were stabilized inside the SiO_2 matrix during the thermal cycles. It is better to have a more stable embedded Sn without oxidation. This can be achieved by further coating of the produced Sn@p-SiO_2. However, this is not the focus of this study wherein we address the problem of Sn sintering and coalescence during the operation by using p-SiO_2 as matrix to disperse and stabilize Sn NPs from sintering to certain extend for thermal cyclic stability. Besides, our samples are intended to be used in an

air-free condition like heat transfer fluids and other nanofluids with organic based fluids.

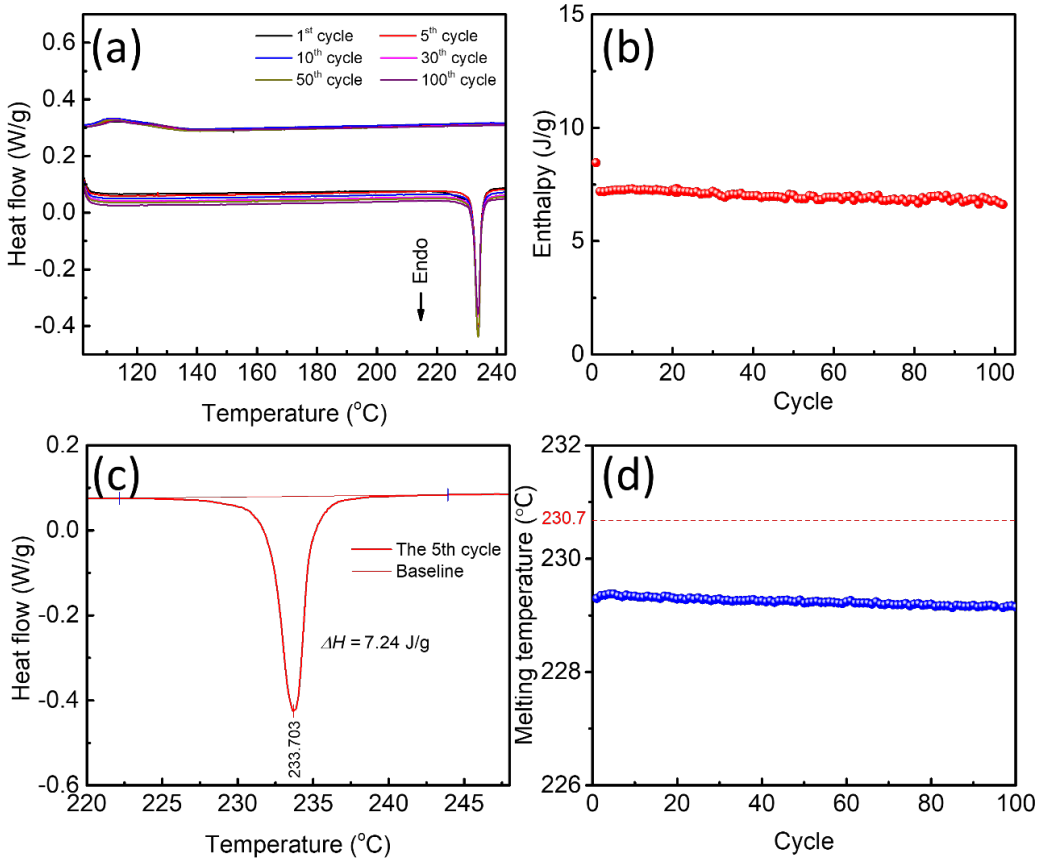

Figure 2.10 Thermal properties of Sn NPs@p-SiO_2.

(a) DSC results of 100 melt-freeze cycles for Sn NPs@p-SiO_2. (b) The enthalpy of melting vs cycle number. (c) Example of the DSC curve for the 5th cycle in the 220 – 245°C range for calculating the enthalpy of melting. (d) Melting temperature of Sn NPs confined into p-SiO_2 (blue empty circles) at each cycle compared to the melting temperature of bulk Sn (red dashed line).

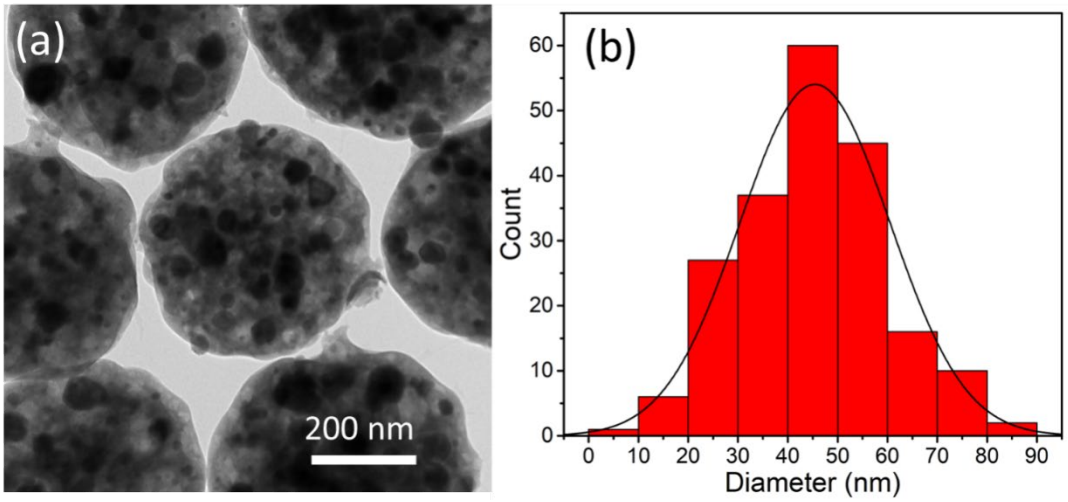

Figure 2.11 Morphology of Sn NPs@p-SiO_2 after 20 melt-freeze cycles$_2$.

(a) TEM image of Sn NPs@p-SiO_2 after 20 melt-freeze cycles and (b) particle size distribution of Sn NPs embedded in p-SiO_2 shown in (a).

2.4 Conclusions

In this work, we synthesized a nanostructure where phase change Sn NPs were confined inside p-SiO_2 spheres, by using a facile method utilizing common starting chemicals. The p-SiO_2 spheres we used effectively stabilized the embedded Sn NPs during cyclic melting-cooling. The melting depression phenomenon of the Sn NPs expands the application window of phase change thermal energy storage by using low melting temperature metals.

The formation of voids inside Sn NPs@p-SiO_2 was investigated for the first time. The transformation of the Sn precursor occurred and included the formation and decomposition of the amorphous Sn precursor, formation and reduction of crystal Sn oxides and interactions between Sn NPs and SiO_2 during annealing in a 3% H_2/N_2

atmosphere. We believe that the transformation of the Sn precursor during annealing accompanied by the modification of the formed Sn NPs led to the formation of big voids inside p-SiO_2 spheres, which gives inspiration for new strategies for the synthesis of hollow SiO_2 spheres and yolk-shell SiO_2 structures.

References

1. Hyun, D. C.; Levinson, N. S.; Jeong, U.; Xia, Y., Emerging Applications of Phase-Change Materials (PCMs): Teaching an Old Dog New Tricks. *Angew. Chem. Int. Ed.* **2014**, *53*, 3780-3795.
2. Pielichowska, K.; Pielichowski, K., Phase change materials for thermal energy storage. *Prog. Mater. Sci.* **2014**, *65* (Supplement C), 67-123.
3. Nomura, T.; Zhu, C.; Sheng, N.; Saito, G.; Akiyama, T., Microencapsulation of Metal-based Phase Change Material for High-temperature Thermal Energy Storage. *Sci. Rep.* **2015**, *5*, 9117.
4. Xuan, Y.; Li, Q., Heat transfer enhancement of nanofluids. *Int. J. Heat Fluid Flow* **2000**, *21*, 58-64.
5. Keblinski, P.; Eastman, J. A.; Cahill, D. G., Nanofluids for thermal transport. *Mater. Today* **2005**, *8*, 36-44.
6. Shin, D.; Banerjee, D., Enhanced Thermal Properties of PCM Based Nanofluid for Solar Thermal Energy Storage. *ASME 2010 4th International Conference on Energy Sustainability* **2010**, (43949), 841-845. (Conference paper)
7. Chieruzzi, M.; Cerritelli, G. F.; Miliozzi, A.; Kenny, J. M., Effect of nanoparticles on heat capacity of nanofluids based on molten salts as PCM for thermal energy storage. *Nanoscale Res. Lett.* **2013**, *8*, 448.
8. Shin, D.; Banerjee, D., Enhanced specific heat of silica nanofluid. *J. Heat Transfer* **2011**, *133*, 024501.
9. Gawande, M. B.; Goswami, A.; Asefa, T.; Guo, H.; Biradar, A. V.; Peng, D.-L.; Zboril, R.; Varma, R. S., Core-shell nanoparticles: synthesis and applications in catalysis and electrocatalysis. *Chem. Soc. Rev.* **2015**, *44*, 7540-7590.
10. Ghosh Chaudhuri, R.; Paria, S., Core/Shell Nanoparticles: Classes, Properties, Synthesis Mechanisms, Characterization, and Applications. *Chem. Rev.* **2012**, *112*, 2373-2433.
11. Cingarapu, S.; Singh, D.; Timofeeva, E. V.; Moravek, M. R., Nanofluids with encapsulated tin nanoparticles for advanced heat transfer and thermal energy storage. *Int. J. Energy Res.* **2014**, *38*, 51-59.
12. Smith, G. D.; Bedrov, D., Dispersing Nanoparticles in a Polymer Matrix: Are Long, Dense Polymer Tethers Really Necessary? *Langmuir* **2009**, *25*, 11239-11243.
13. Yeshchenko, O. A.; Dmitruk, I. M.; Alexeenko, A. A.; Dmytruk, A. M., Size-dependent melting of spherical copper nanoparticles embedded in a silica matrix. *Phys. Rev. B* **2007**, *75*, 085434.

14. Liu, M.; Ma, Y.; Wu, H.; Wang, R. Y., Metal Matrix–Metal Nanoparticle Composites with Tunable Melting Temperature and High Thermal Conductivity for Phase-Change Thermal Storage. *ACS Nano* **2015**, *9*, 1341-1351.
15. Liu, M.; Wang, R. Y., Phase change nanocomposites with tunable melting temperature and thermal energy storage density. *Nanoscale* **2013**, *5*, 7234-7237.
16. De Juan, L. M. Z.; Maggay, I. V. B.; Nguyen, M. T.; Liu, W.-R.; Yonezawa, T. "β-Sn nanorods with Active (001) Tip Induced LiF-Rich SEI Layer for Stable Anode Material in Lithium-ion Battery, *ACS Appl. Nano Mater.*, in press. DOI: 10.1021/acsanm.8b00664
17. De Juan, L. M. Z.; Nguyen, M. T.; Yonezawa, T.; Tokunaga, T.; Tsukamoto, H.; Ishida, Y. Structural Control Parameters for Formation of Single-Crystalline β-Sn Nanorods in Organic Phase. *Crst. Growth Des.*, **2017**, *17*, 4554-4562.
18. Shirai, H.; Nguyen, M. T.; Ishida, Y.; Yonezawa, T. A New Approach for Additive-free Room Temperature Sintering of Conductive Patterns Using Polymer-stabilized Sn Nanoparticles. *J. Mater. Chem. C*, **2016**, *4*, 2228-2234.
19. Chen, Y.; Chen, H.-R.; Shi, J.-L., Construction of Homogenous/Heterogeneous Hollow Mesoporous Silica Nanostructures by Silica-Etching Chemistry: Principles, Synthesis, and Applications. *Acc. Chem. Res.* **2014**, *47*, 125-137.
20. Yu, Q.; Wang, P.; Hu, S.; Hui, J.; Zhuang, J.; Wang, X., Hydrothermal Synthesis of Hollow Silica Spheres under Acidic Conditions. *Langmuir* **2011**, *27*, 7185-7191.
21. Deng, Y.; Qi, D.; Deng, C.; Zhang, X.; Zhao, D., Superparamagnetic High-Magnetization Microspheres with an Fe_3O_4@SiO_2 Core and Perpendicularly Aligned Mesoporous SiO_2 Shell for Removal of Microcystins. *J. Am. Chem. Soc.* **2008**, *130*, 28-29.
22. de Bussetti, S. G.; Tschapek, M.; Helmy, A. K., Calorimetric determination of the point of zero charge. *J. Electroanal. Chem.* **1972**, *36*, 507-511.
23. Tadros, T. F.; Lyklema, J., The operative mechanism of glass electrodes and the structure of the electrical double layer on glass. *J. Electroanal. Chem. Interface. Electrochem.* **1969**, *22(1)*, 9–17
24. Von Schnering, H. G.; Nesper, R.; Pelshenke, H., $Sn_{21}Cl_{16}(OH)_{14}O_6$ das sogenannte basische Zinn (II)-chlorid. *Z. Naturforsch. B* **1981**, *36*, 1551-1560.
25. Joo, S. H.; Park, J. Y.; Tsung, C.-K.; Yamada, Y.; Yang, P.; Somorjai, G. A., Thermally stable Pt/mesoporous silica core–shell nanocatalysts for high-temperature reactions. *Nat. Mater.* **2009**, *8*, 126-131.
26. Ruckdeschel, P.; Kemnitzer, T. W.; Nutz, F. A.; Senker, J.; Retsch, M., Hollow silica sphere colloidal crystals: insights into calcination dependent thermal transport. *Nanoscale* **2015**, *7*, 10059-10070.

27. Liu, M.; Wang, R. Y., Size-Dependent Melting Behavior of Colloidal In, Sn, and Bi Nanocrystals. *Sci. Rep.* **2015**, *5*, 16353.
28. Lai, S. L.; Guo, J. Y.; Petrova, V.; Ramanath, G.; Allen, L. H., Size-Dependent Melting Properties of Small Tin Particles: Nanocalorimetric Measurements. *Phys. Rev. Lett.* **1996**, *77*, 99-102.

Chapter 3.

Al_2O_3 Encapsulated Sn Microparticles for Thermal Energy Storage

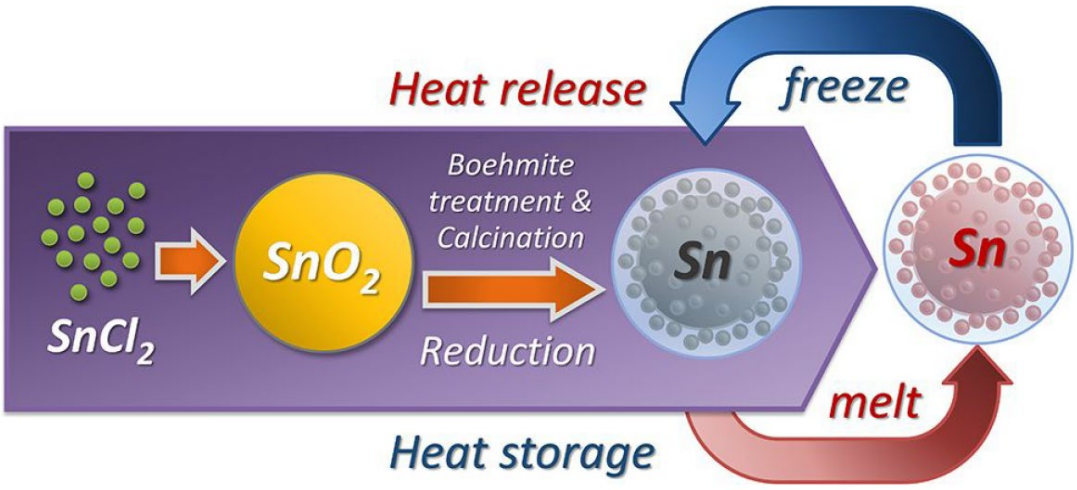

Abstract

The most commonly used phase change materials (PCMs), like organic compounds and inorganic salts, were limited in application by their low thermal conductivity. Herein, for the first time, alumina-encapsulated metallic Sn-based PCMs, named Sn@Al_2O_3, were successfully fabricated with tunable size (60–2000 nm) by a facile process from low-cost chemicals. The robust fabrication process consists of a surfactant-free solvothermal synthesis of SnO_2 spheres, boehmite treatment on SnO_2 spheres, calcination in the air, and the final hydrogen reduction to transform SnO_2 to metallic Sn, endowing the PCMs with high potential for mass production. The as-obtained Sn@Al_2O_3 showed a core–shell structure, in which a main metallic Sn core located in the center covered with an Al_2O_3shell with small Sn nanoparticles distributed inside. The boehmite treatment, in which the penetration of aluminum species into SnO_2 spheres played an important role, was found to be responsible for the unique structure formation of final Sn@Al_2O_3. The understanding of structure formation mechanism gives the possibilities of a new facile way for the synthesis of metal nanoparticles and particle-distributed nanostructures. The obtained Sn@Al_2O_3 particles not only have high PCM content (92.37 wt %) but also show a stable thermal behavior and morphology during 100 melt–freeze cycles in the air atmosphere. Furthermore, the low melting temperature of the PCM core, combined with high thermal conductivity of both core material (Sn, 66.8 W m^{-1} K^{-1}) and shell material (Al_2O_3, 35 W m^{-1} K^{-1}), makes Sn@Al_2O_3 potentially suitable for rapid thermal energy storage in the range 100–300°C.

3.1 Introduction

Using latent heat in phase change materials (PCM) is one of the most efficient ways of storing thermal energy and it has received wide attention in decades. However, the biggest historical drawback of using conventional PCM, such as organic materials and inorganic salt, etc. is their low thermal conductivity.[1-5] In addition, for organic PCMs, the phase change temperature (solid to liquid) is generally below 200°C; for inorganic salts, the large volume changes during melting and high corrosion may occur. Those give limitations for their wider applications.[3, 6]

Metals and their alloys can overcome these problems existing in organic compounds and inorganic salts as mentioned above. Low-melting-point metals are promising materials that can be used as PCM for heat storage and thermal management in wider working conditions.[4, 6, 7] Due to the high thermal conductivity, the metallic heat storage media shows rapid thermal energy transfer.[8] In addition, the high density of the metals also contributes to the high-volume density of heat storage.[3] Based on these advantages, the low-melting point metals can be applied in the thermal energy storage system in concentrated solar power (CSP) station.[9, 10] It also could be used for chip cooling in USB flash memory,[11] smartphones[12] and other high-power-density devices.[13, 14]

However, the leakage and sintering of liquid metal particles in low-melting-point metal PCM may lead to the changes in as-designed structure or morphology during operation, deteriorating their sustainable usage in the form of nanofluids or slurry.[15] The widely used solution to these problems is to create isolation on each

individual PCM particles. Based on this solution, there were several strategies. One method involves introducing an inert shell or layer outside the pre-synthesized low-melting-point metal particles. Cingarapu *et al.*[16] synthesized and studied the thermal properties of silica (SiO_2) coated Sn nanoparticles. Hsu *et al.*[17] prepared Zn@TiO_2, Zn@Al_2O_3, and Zn@SiO_2 core-shell microparticles with commercial Zn powder. Another method involves inserting metal nanoparticles into an inert matrix. Liu et al. used pre-synthesized Bi nanocrystals to prepare nanocomposites where Bi nanoparticles were evenly embedded in an Ag matrix and a polyimide (PI) resin matrix. However, both methods require the complex pre-synthesis of metal nanoparticles or microparticles. In our previous work, metallic Sn nanoparticles as the PCM that confined in a porous SiO_2 spherical matrix were prepared through a facile method by thermal hydrogen reduction which can be potentially used for mass production.[20] While the content of PCM was relatively low and the encapsulated matrix has low thermal conductivity (1.3 W m^{-1} K^{-1}), which set a limitation for their application as thermal energy storage materials.

In this study, to make the best use of the high thermal conductivity and thermal energy storage of low-melting-point metal PCM, alumina (Al_2O_3) was chosen as the encapsulation material[21] instead of SiO_2 due to high thermal conductivity (35 W m^{-1} K^{-1}). Until now, a few examples have been reported to achieve using Al_2O_3 to coat low-melting-point metal for thermal energy storage[17]. Here, Sn@Al_2O_3 PCM particles with high PCM content (92.37 wt%) were successfully synthesized through a facile 3-step method from low-cost common chemicals which is suitable for up-scale synthesis for

mass production. The size and structure of $Sn@Al_2O_3$ can be easily tuned by modifying the synthesis process. Furthermore, PCM content, thermal energy storage properties were carefully examined. Finally, the structure and thermal stability during melting was also investigated by performing a melt-freeze 100-cycles test in the air.

3.2 Materials and Methods

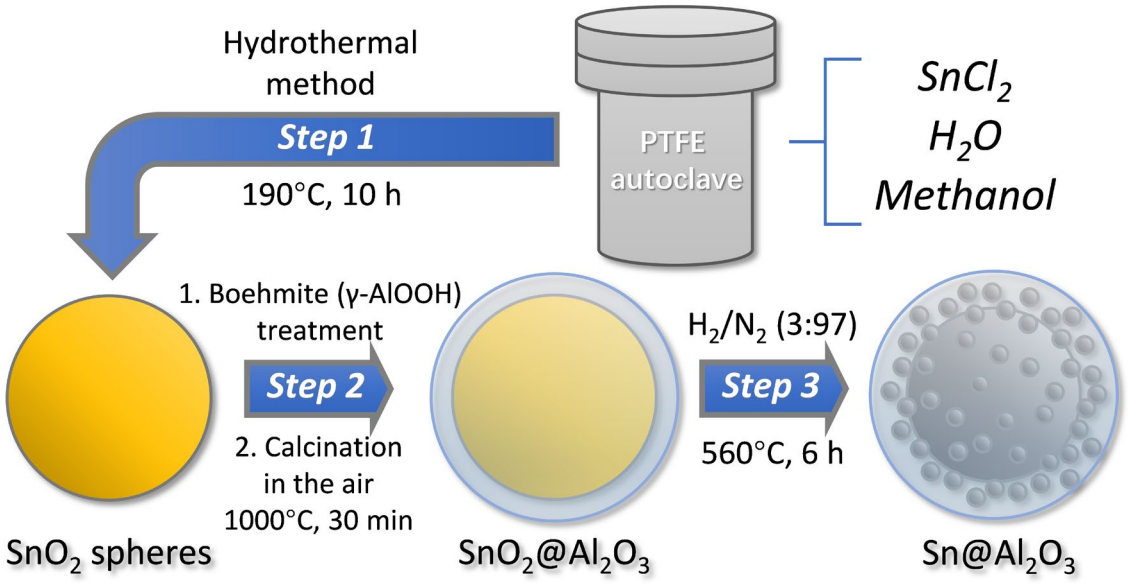

Scheme 3.1 Synthesis process of $Sn@Al_2O_3$ spheres.

Step 1: Synthesis of SnO_2 spheres through hydrothermal method; Step 2: Boehmite treatment and calcination in the air; Step 3: Reduction of the Sn precursor $SnO_2@Al_2O_3$ to obtain $Sn@Al_2O_3$.

3.2.1 Chemicals

Aluminum nitrate nonahydrate ($Al(NO_3)_3$ $9H_2O$) was purchased from Wako (Osaka, Japan). Anhydrous tin (II) chloride ($SnCl_2$) (min. 98%), methanol (99.5% purity), 1-propanol (99.5% purity), ammonia solution (min. 28%) were purchased from Junsei (Tokyo, Japan). All the chemicals were used without further purification. Water was purified using a PureLabo system (Organo/ELGA, >18 MΩ).

2.2.2 Synthesis of SnO_2 Spheres

0.1 g $SnCl_2$ was added into a mixture solvent of methanol (40 mL) and deionized water (1 mL). After sonication for 5 min and stirred for 30 min, 15 mL of this salt solution was transferred to a Teflon-lined stainless-steel autoclave (20 mL) and kept in a muffle furnace at 190°C for 10 h. Afterward, the autoclave was taken out to cool down naturally. The white precipitate was collected by centrifugation (6000 rpm, 5 minutes) and washed with 1-propanol before vacuum dried at 25°C for 6 h.

3.2.3 Synthesis of $Sn@Al_2O_3$

A boehmite sol for boehmite treatment was synthesized by adding 30 mL $Al(NO_3)_3$ aqueous solution (0.3 M) and 10 mL ammonia solution (50%) dropwise into 10 mL deionized water by using syringe pump followed by stirring and refluxing the solution for 24 h. Then 0.05 g as-prepared SnO_2 spheres were well dispersed into 1 mL of the boehmite sol with an addition of 5 mL deionized water and refluxed for 12 h. Afterwards, SnO_2 spheres treated with boehmite were collected by centrifugation (6000

rpm, 5 min) and washed twice with deionized water and 1-propanol. After drying in vacuum, the powder was calcined at 1000°C in the air in a tube furnace for 30 min, and finally, the calcined product was reduced in a tube furnace by a mixed H_2/N_2 (3:97) gas flow (1 $L \cdot min^{-1}$) at 560°C for 6 h. The final product, $Sn@Al_2O_3$, was obtained as a black powder. The whole preparation process was illustrated in Scheme 1.

3.2.4 Characterization

The morphology of the produced $Sn@Al_2O_3$ was examined using scanning electron microscopy (SEM) (Hitachi TM3030Plus, 15 kV and JEOL JSM-6701F, 15kV) and transmission electron microscopy (TEM) (JEOL JEM-2000FX, 200 kV). The high-resolution transmission electron microscopy (HRTEM) images were taken by using JEM-1000K RS TEM (JEOL) operated at 1000 kV. The cross-section images were taken by using a focused ion beam scanning electron microscopy (FIB-SEM) (Hitachi, MI-4000L and JEOL, JIB-4601F). The crystal and phase structures of the products were characterized using X-ray diffraction (XRD) (Rigaku Miniflex II X-ray diffractometer with Cu Kα radiation, λ = 1.5418 Å. The element distribution and depth profile were characterized using X-ray photoelectron spectroscopy (XPS) (JEOL JPS-9200 photoelectron spectrometer with monochromatic Al-Kα radiation). The melt-freeze cycle test was performed using a differential scanning calorimetry (DSC) (Rigaku, DSC 8270) to evaluate the operation durability. In these measurements, a 5 mg specimen in an Al crucible was repeatedly heated to 250°C at a ramping rate of 20°C min^{-1} and then cooled to 100°C naturally in the air atmosphere.

3.3 Results and Discussions

3.3.1 Morphology and Structure Characterizations of $Sn@Al_2O_3$

The structure of $Sn@Al_2O_3$ was checked by TEM (Figure 3.1a) and SEM (Figure 3.1b). It was found that a big spherical core (1~2 μm) and many small spheres (50~250 nm) with higher contrast were encapsulated by a thick shell (100~700 nm) with lower contrast. No sintered Sn particle was found in the SEM images, indicating a good encapsulation of Sn spheres (Figure 3.1b, Figure S3.1a). Selected area electron diffraction (SAED) was used to examine the crystal structure of core and shell materials. The SAED pattern of the cores in the shell (Figure 3.1c) and the shell (Figure 3.1d) were indexed to tetragonal metallic Sn (beta-Sn) and alumina (Al_2O_3, JCPDS No. 01-075-0921), respectively. All peaks of XRD pattern of $Sn@Al_2O_3$ can be indexed to tetragonal metallic Sn (Figure 3.1e). The absence of peaks from Al_2O_3 indicates that the Al_2O_3 shell presents an amorphous state.

The EDS was also used to provide composition information from different parts of the $Sn@Al_2O_3$ (Figure S3.1). The position of center core (position 1) contained mainly Sn element (95.64 at%) while the Al (30.17 at%) and O (66.20 at%) are the main elements of the shell without small black particles (position 3). The small particles embedded inside the shell contained all Sn (29.53 at%), Al (22.99 at%) and O (47.47 at%) elements due to the combination of Al and Sn signals from Al_2O_3 shell and Sn particles.

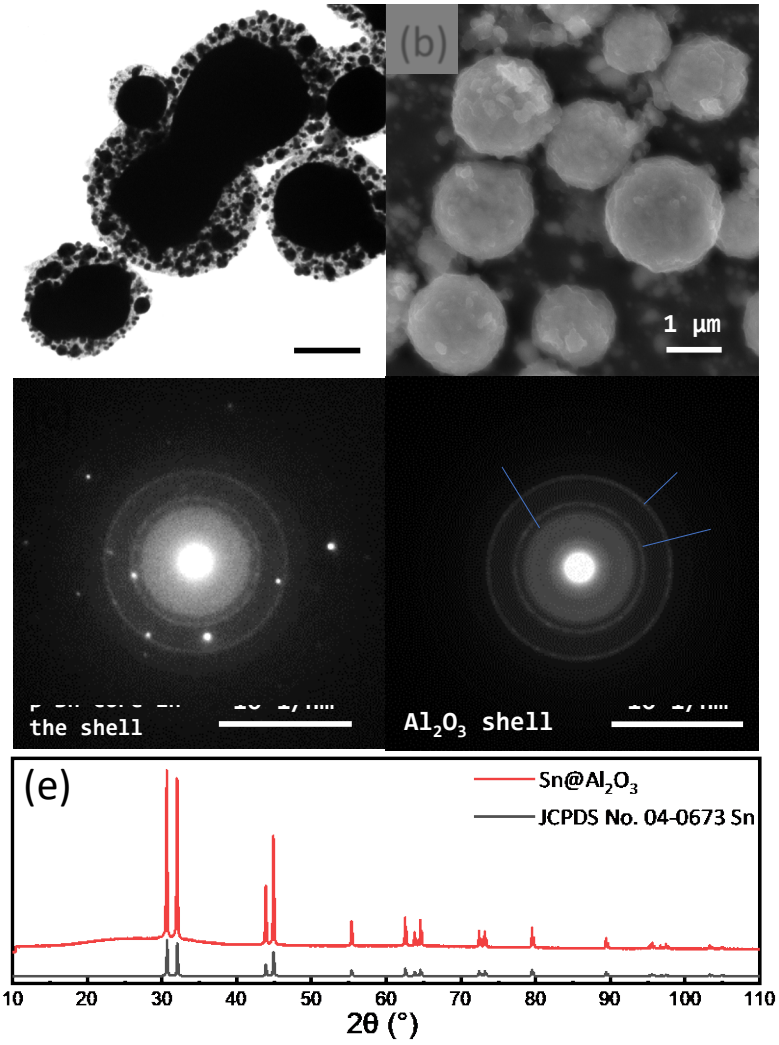

Figure 3.1 Morphology of as-synthesized $Sn@Al_2O_3$ spheres.

TEM (a) and SEM (b) images of $Sn@Al_2O_3$ particles. SAED patterns of black cores inside shell of $Sn@Al_2O_3$ (c) and shell with light contrast (d). (e) XRD pattern of as-prepared $Sn@Al_2O_3$ particle powder.

3.3.2 Structure Formation Mechanism

To investigate the structure formation mechanism of $Sn@Al_2O_3$, the intermediates of the final product at each step of the synthesis were investigated. As

mentioned in the experiment part, the SnO_2 spheres (Sn precursor) were treated in boehmite sol and then calcined at 1000°C in the air to form $SnO_2@Al_2O_3$ (intermediate of $Sn@Al_2O_3$).

TEM and SEM were used to investigate the morphology change of $SnO_2@Al_2O_3$ from SnO_2 spheres. No change in size of SnO_2 spheres was observed after boehmite treatment according to the TEM and SEM images (Figure 3.2a, c and Figure S3.2). From TEM observation, it was found that $SnO_2@Al_2O_3$ did not show the structure of big core with thick shell as we expected. Instead, a solid sphere, surrounded with small number of fragments, was observed. There is no doubt that the fragments outside the spherical particle were not able to build the ~400 nm-thick shell of the final product $Sn@Al_2O_3$ (Figure 3.1a). These surrounding fragments also can be observed in the SEM image (Figure 3.2c) as the rough surface of particles compared to the surface of the calcined SnO_2 spheres without boehmite treatment (Figure S3.2). The SAED pattern of the surrounding fragments shown in Figure 3.2a (area shown in the red circle) was indexed to SnO_2 (JCPDS No. 01-077-0452) (Figure 3.2b). The significant morphology difference between $SnO_2@Al_2O_3$ and $Sn@Al_2O_3$ inspired us to investigate the formation mechanism of $Sn@Al_2O_3$.

By comparing the morphologies of $Sn@Al_2O_3$ (Figure 3.2f) with SnO_2 sphere (Figure 3.2e) and $SnO_2@Al_2O_3$ (Figure 3.2a), it was found that the thick shell appeared after $SnO_2@Al_2O_3$ was reduced to $Sn@Al_2O_3$, while no obvious difference in overall size was observed. It was believed that the penetration of boehmite sol (AlOOH) into

the SnO_2 spheres may occur due to the interaction between boehmite and SnO_2. This may contribute to the formation of thick Al_2O_3 shell of $Sn@Al_2O_3$. In addition, the Sn particles embedded in the shell of $Sn@Al_2O_3$ were formed via reduction of SnO_2, which were believed to be separated by the Al species diffused in SnO_2 during boehmite treatment. To investigate the effects of boehmite treatment on the structure of SnO_2 spheres, FIB was used to create a cross-section surface on a single $SnO_2@Al_2O_3$ particle. The cross-section SEM image of $SnO_2@Al_2O_3$ was shown in Figure 3.2d. Porous structure was found inside the $SnO_2@Al_2O_3$ spheres. This structure showed a great difference from the dense structure inside air calcined SnO_2 spheres without boehmite treatment (Figure 3.2e), which is further investigated by HRTEM. As shown in Figure S3.3, the lattice space 0.310 nm of $SnO_2@Al_2O_3$ was not able to be indexed to Al_2O_3 or SnO_x, but (0004) plane of $AlSnO_3$,[22] indicating the reactions may occur between SnO_2 and boehmite. Figure 3.2g shows the XRD pattern of SnO_2 spheres just after boehmite treatment and calcination at 1000°C in the air, in which the main peaks can be indexed to SnO_2 (JCPDS No. 01-077-0452) and some small peaks (*e.g.* 46° (200)) can be indexed to Al_2O_3 (JCPDS No. 01-075-0921). Different from the sharp SnO_2 peaks in the XRD pattern of SnO_2 spheres (Figure 3.2g, green), XRD pattern of $SnO_2@Al_2O_3$ showed the broadening of SnO_2 peaks (Figure 3.2g, red), indicating the smaller crystalline size (6.4 nm) of SnO_2 in $SnO_2@Al_2O_3$ compared to that of SnO_2 spheres (87.6 nm). This decrease in crystalline size may be a result of the penetration of Al species into SnO_2 spheres and reaction with SnO_2, leading to the formation of the porous structure inside the $SnO_2@Al_2O_3$ shown in the cross-section SEM image. In

addition, both as synthesized boehmite and calcined boehmite were checked by XRD, which is shown in Figure S3.4. After calcination in air, the absence of peaks of boehmite and the appearance of Al_2O_3 indicate the transformation from boehmite to Al_2O_3.

To confirm the distribution of Al element inside the intermediates (SnO_2@Al_2O_3), we checked the elemental composition inside SnO_2@Al_2O_3 through XPS depth profile. The wide scan on the surface of SnO_2@Al_2O_3 showed the existence of Sn, Al, O, and C (Figure 3.3a). Carbon peak C1s came from the carbon tape for loading SnO_2@Al_2O_3 powder sample, and it was also used for charge correction in each scan. Afterwards, narrow scans were performed on SnO_2@Al_2O_3 at certain depths (25 nm, 50 nm, and 300 nm) to obtain the chemical states information at different depths inside SnO_2@Al_2O_3. Figure 3.3c and d showed the narrow scan of Al 2p peak and Sn 3d peaks at the position of different Ar etching depths in SnO_2@Al_2O_3 spheres. The narrow scan of Al 2p without Ar etching (on the surface, 0 nm) is shown in Figure 3.3b, in which Al 2p peak was deconvoluted to two separated peaks located at 72.0 eV (blue) and 74.2 eV (red), representing tetrahedral Al^{3+} and octahedral Al^{3+} respectively.[23] The formation of these two different Al^{3+} species may be caused by the different local oxygen abundance in the SnO_2@Al_2O_3 and the effect of Sn atoms. This phenomenon was also found previously in some Al related spinel structures. In addition, reactions occurred between SnO_2 and Al species possibly caused the formation of tetrahedral Al^{3+} and octahedral Al^{3+} according to the former discussion on Figure S3.3.

As we used deeper Ar etching, it was found that Al species still existed inside the SnO_2@Al_2O_3 spheres at 25 nm, 50 nm, and even 300 nm depths. These results are in good agreement with the Al_2O_3 shell thickness of Sn@Al_2O_3 spheres shown in Figure 3.1a. Moreover, as the Ar etching depth increased, the peak for octahedral Al^{3+} (74.2 eV) decreased while the peak for tetrahedral Al^{3+} (72.0 eV) increased. The ratio change of these two Al species indicates the existence of different Al-O structure at different depths inside the SnO_2@Al_2O_3 spheres.

In Sn 3d narrow scans, higher intensity of Sn 3d peaks was observed at the deeper position, indicating that more Sn was detected in the central area of SnO_2@Al_2O_3, thus less Al species were distributed near the center of SnO_2@Al_2O_3. Therefore, at the deeper position, big Sn core formed during the reduction process due to the enrichment of Sn element and the absence of the separation provided from Al_2O_3. In addition, the peak of Sn 3d5/2 was found shifted from 486.7 eV (SnO_2) to 486.3 eV (SnO) as etching depth increased from 0 to 300 nm. The shift of Sn 3d peak to the smaller binding energy indicates the existence of Sn(II) inside the SnO_2@Al_2O_3 spheres due to a lower abundance of oxygen in deeper depth. This also affected the Al^{3+} structure inside the SnO_2@Al_2O_3 spheres, which behaves as the shift of Al 2p peak shown in Figure 3.3c.

To test our findings above, the Sn@Al_2O_3 samples with different sizes from ~600 nm to ~60 nm were synthesized for comparison with Sn@Al_2O_3 (Figure 3.4e) obtained from the standard synthesis. Considering the particle size, our samples were

named as $Sn@Al_2O_3$-XX and $SnO_2@Al_2O_3$-XX, in which "XX" represents the overall diameter of the particles in nm. For example, $Sn@Al_2O_3$-1600 is $Sn@Al_2O_3$ of 1600 nm prepared from standard synthesis. The formation of the big Sn core located in the center of $Sn@Al_2O_3$-1600 may be the result of absence or very low amount of Al species in the deep positions inside of the $SnO_2@Al_2O_3$ spheres due to the partial penetration of Al species. Figure 3.4b and 3.4f show the morphologies of $SnO_2@Al_2O_3$-600 and $Sn@Al_2O_3$-600 respectively. It was found that when the smaller SnO_2 spheres were used for boehmite treatment and further reduction, the corresponding product $Sn@Al_2O_3$-600 had a relatively smaller Sn core located in the central position with many small Sn particles distributed around (Figure 3.4f). The size of these small Sn particles was close to the size of Sn particles distributed in the shell of $Sn@Al_2O_3$-1600 (Figure 3.4e). The decrease in size of the central Sn core shown in Figure 3.4f may result from the deeper penetration of Al species into SnO_2 spheres, leading to the formation of Al oxides in deeper position that isolate the Sn particles from aggregation or sintering during the high-temperature reduction. The deeper Al penetration resulted in the smaller size of Sn core in the central position (Figure 3.4j), which was further confirmed by the structure formation process of smaller particles. Figure 3.4c shows $SnO_2@Al_2O_3$-350 particles when using ~350 nm SnO_2 spheres as Sn precursor. The corresponding $Sn@Al_2O_3$-350 particles obtained after reduction had only small Sn particles distributed inside Al_2O_3 (Figure 3.4g), no obvious central Sn core was observed. The absence of central Sn core may be caused by the nearly full penetration or full penetration of Al species into small SnO_2 spheres (350 nm), which separated

SnO_2 in the whole particle. As a result, the formation of small Sn particles distributed inside the Sn@Al_2O_3-350 was observed (Figure 3.4k). Interestingly, when the SnO_2 particles with even smaller size (~60 nm) were chosen for boehmite treatment and reduction, it was found that the Sn nanoparticles were obtained and uniformly distributed in Al_2O_3 after reduction (Sn@Al_2O_3-60, Figure 3.4h). In this case, only single Sn nanoparticle as the core in Al_2O_3 was observed. The detail TEM images and SAED patterns of as-synthesized Sn@Al_2O_3-60 and SnO_2@Al_2O_3-60 were shown in the Figure S3.5. The results reveal that the synthesis method is good in terms of size control for Sn@Al_2O_3 from nanoscale to microscale. Besides, this approach is potential for the facile synthesis of other types of metal nanoparticles with low-cost and non-toxic chemicals.

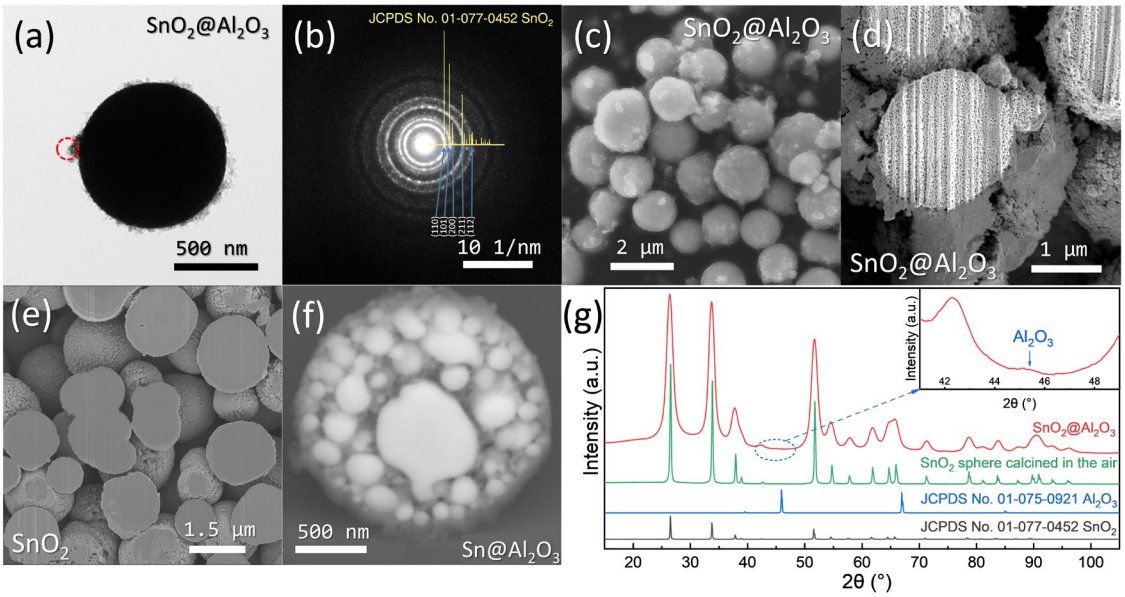

Figure 3.2 Morphology of the intermediate $SnO_2@Al_2O_3$

(a) TEM and (c) SEM image of SnO_2 spheres after boehmite treatment and calcination ($SnO_2@Al_2O_3$). (b) SAED pattern of the shatter at the surface of SnO_2 spheres (area shown in the red circle in (a)). Cross-section SEM images of (d) $SnO_2@Al_2O_3$ spheres, (e) SnO_2 spheres and (f) $Sn@Al_2O_3$ sphere. (g) XRD patterns of the as obtained $SnO_2@Al_2O_3$ (red curve) and SnO_2 sphere after calcined in the air (green).

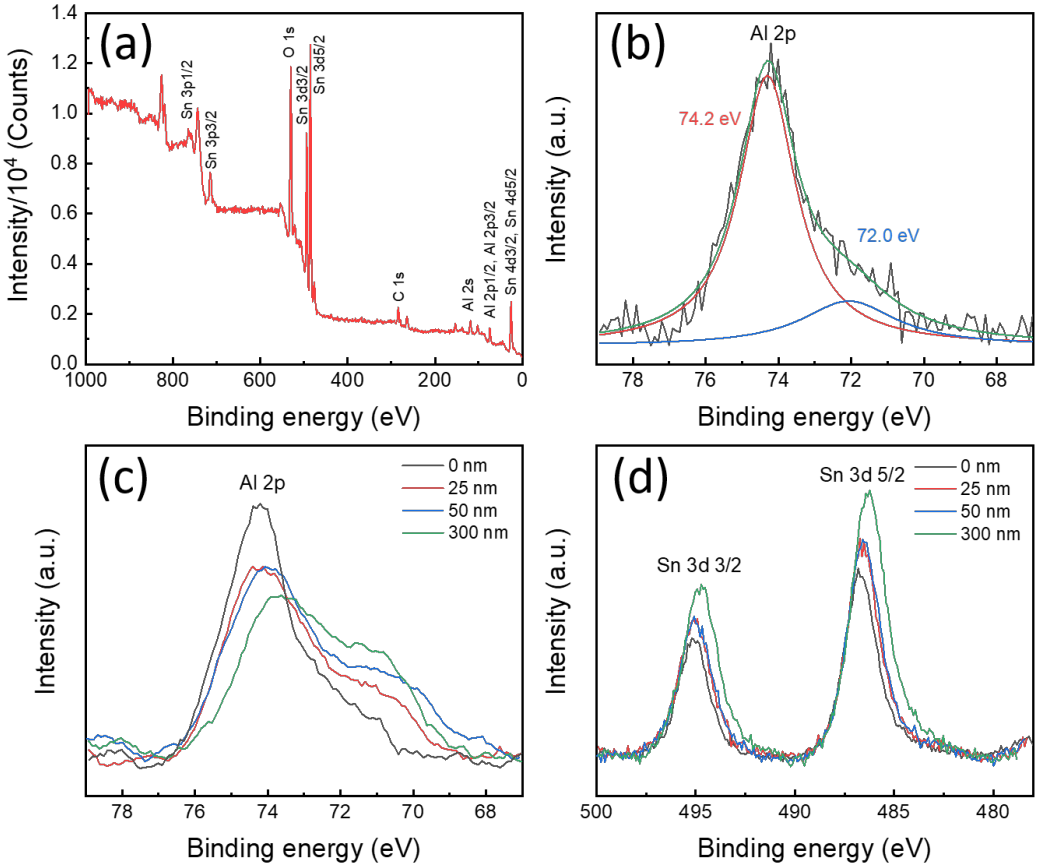

Figure 3.3 XPS investigation of SnO_2@Al_2O_3.

(a) XPS wide scan of as synthesized SnO_2@Al_2O_3. (b) XPS narrow scan of as synthesized SnO_2@Al_2O_3 on Al 2p which can be deconvoluted into two components. Narrow scan on (c) Al 2p and (d) Sn 3d after Ar etching with different etching depths.

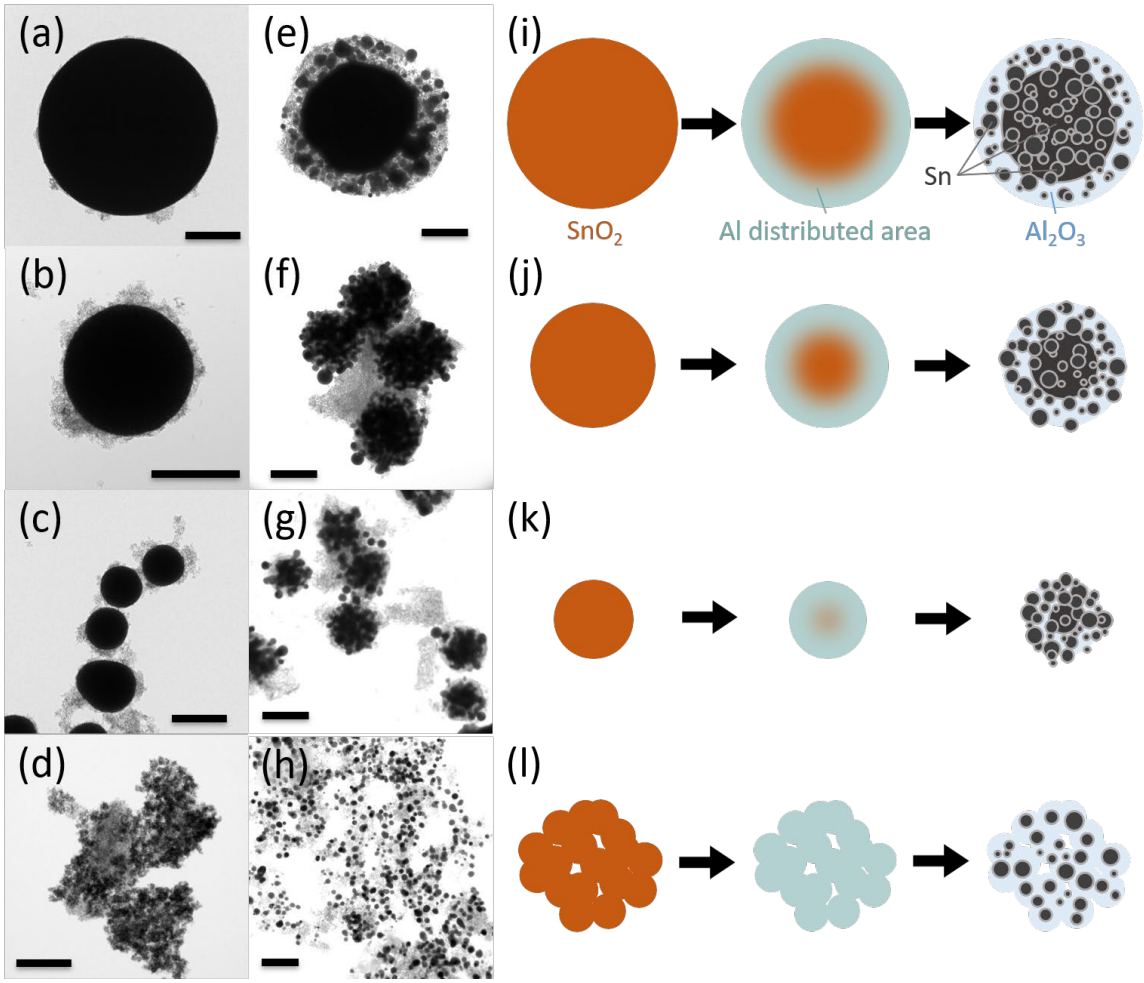

Figure 3.4 Size tunable SnO_2@Al_2O_3 and Sn@Al_2O_3.

TEM images of (e-h) Sn@Al_2O_3 with different morphologies (e: Sn@Al_2O_3-1600, f: Sn@Al_2O_3-600, g: Sn@Al_2O_3-350, h: Sn@Al_2O_3-60) reduced from corresponding (a-d) SnO_2@Al_2O_3 (a: SnO_2@Al_2O_3-1600, b: SnO_2@Al_2O_3-600, c: SnO_2@Al_2O_3-350, h: SnO_2@Al_2O_3-60) prepared using SnO_2 with various sizes, i.e. (a) ~1.6 µm, (b) ~600 nm, (c) ~350 nm; (d) ~60 nm. (i-l) The corresponding scheme for the formation of Sn@Al_2O_3. All scale bars are 500 nm.

3.3.3 Thermal Storage Stability

The typical melt-freeze cycle curve of Sn@Al_2O_3-1600 obtained by DSC is shown in Figure S3.6a. An endothermic valley is observed at 233.6°C during heating,

indicating the melting of Sn particles. The melting temperature was measured as 229.1°C. An exothermic peak centered at 137.1°C during the cooling indicates that melted Sn solidified and embedded in Sn@Al_2O_3. For comparison, commercial Sn powder with the measured size of 7.15 ± 5.09 μm (Figure S3.7) was experienced the same thermal process. As shown in Figure S3.6b, an endothermic valley at 235.7°C during heating indicates the melting. Freezing peaks centered at 130.5, 142.7 and 160.9°C were observed in the cooling curve. Compared with the melting temperature of commercial Sn powder (231.6°C), the decrease of melting temperature of Sn@Al_2O_3 possibly originated from size effect of the existence of small Sn nanoparticles dispersed in the shell. According to the model proposed by S. L. Lai *et al.*,[24] 229.1°C corresponded to the melting temperature of Sn nanoparticles with the size of 57.6 nm (Figure S3.8), which is consistent with the size range of some small Sn nanoparticles distributed in the alumina shell (around 40-80 nm shown in Figure S3.9).

To investigate the operation stability during heat storage and release of Sn@Al_2O_3-1600, 100 melt-freeze thermal cycles were performed in the air at the 100–250°C range. The enthalpy of melting for Sn@Al_2O_3-1600 (Figure 3.5a) was calculated based on the integral of the endothermic peak area over time as shown in Figure S3.10, *i.e.*, the enthalpy of melting of the 5th cycle was 46.01 J g^{-1}. Figure 3.5a showed the relative melting enthalpy of Sn@Al_2O_3 (red spheres), which is calculated by using measured latent heat (ΔH) divided by the latent heat of commercial Sn powder (ΔH_0 = 59 J g^{-1}). This value ($\Delta H/\Delta H_0$) can be used to determine the weight percentage of PCM (Sn) embedded inside the Sn@Al_2O_3.

The 12% drop of the enthalpy from the first cycle (92.37%, 54.49 J g^{-1}) to the second one (80.67%, 47.60 J g^{-1}) was due to the oxidation of the surface Sn nanoparticles (Figure S3.9). From the second cycle, the enthalpy of melting showed a slight decrease and ended up at 43.19 J g^{-1} (73.22%) after the 100th cycle (Figure 3.5a). The change in enthalpy melting indicated that after 100 cycles there was approximately 7% of Sn was further oxidized compared with that in the 2nd cycle. The typical melting curves of Sn@Al_2O_3-1600 during the melt-freeze cycles were shown in the Figure S3.12. When the Sn@Al_2O_3-60 was tested at the same experiment conditions (Figure 3.5a), it shows different thermal storage properties. It was found that the latent heat dropped drastically from 36.68 J g^{-1} (62.17% of bulk Sn) to 12.68 J g^{-1} (21.42% of bulk Sn) after cycling in the air for the first 20 cycles. The poor thermal storage stability possibly because the thinner shell of Sn@Al_2O_3-60 has a weaker protection during cycling test. In addition, the size decrease in Sn particles makes oxidation easier to happen when they were exposed in the air due to the increased surface area compared to the bigger particles with the same amount. In order to confirm above statement, the SiO_2-encapsulated Sn PCM prepared in our previous study was selected for the cycle test with the same conditions (Figure 3.5a). The SiO_2-encapsulated Sn PCM, named as Sn NPs@p-SiO_2, also has a core-shell structure, where the size of Sn NPs core was around 30 nm and the size of porous silica shell is around 400 nm[20]. Similar to Sn@Al_2O_3-1600 prepared from the standard synthesis, the Sn NPs@p-SiO_2 also show high thermal storage stability due to the good protection of the thick shell, indicating the thick shell plays a key role for the thermal storage stability. Compared to Sn

NPs@p-SiO_2, it should be noted that the Sn@Al_2O_3-1600 prepared from the standard synthesis has a big enhancement in thermal energy storage density, which is caused by the increase of metallic Sn content (~6.5 times) in Sn@Al_2O_3-1600.

Furthermore, the onset temperature, peak temperature and offset temperature of Sn@Al_2O_3 for each melting endothermic peak were investigated and shown in Figure 3.5b. The definition of these three values was shown in Figure S3.11. Generally, the onset temperature is the designed intersection point of the extrapolated baseline and the inflectional tangent at the beginning of the melting, thus, in the metal Sn, the onset temperature can be indicated as melting temperature.[25, 26] As shown in Figure 3.5b the onset, peak and offset temperatures of Sn@Al_2O_3 were lower than that of commercial Sn powder (Figure S3.6b), indicating the existence of small Sn particles inside the sample. The linear fitting of onset and offset temperature showed a visible growth tendency with the increase of cycle number, while the linear fitting of peak temperature kept stable at 233.4°C. The growth of onset temperature of melting peak indicates the beginning temperature for melting increased, which is a result of gradual disappearance of small Sn nanoparticles due to the oxidation in the air. The oxide peaks (SnO and SnO_2) after 100 melt-freeze cycles in the air were shown in the XRD pattern (Figure 3.5c). Also, the SAED pattern of small particles located near the surface after cycle test showed the existence of Sn oxides (Figure S3.13). The stable peak temperature during the cycle test can be explained by the existence of stable big Sn core located at the center of Sn@Al_2O_3-1600.

The TEM and SEM images comparison of Sn@Al_2O_3-1600 spheres before and after 100 melt-freeze cycles in the air were shown in the Figures 3.6a, b, d and e. By comparison, morphology changes, especially sintering and breakage of the shell were not found in Sn@Al_2O_3. No significant change in size was observed according to the size histogram (Figure S3.14). SEM images of Sn@Al_2O_3-1600 with low magnifications before and after melt-freeze cycle test were given in Figure S3.15. These results emphasized that the Sn particles were well stabilized inside the Al_2O_3 shell during the thermal cycles. The volume changes of metallic Sn due to the solid-liquid transformation were possibly absorbed by the Al_2O_3 shell structure. We also took the commercial Sn powder to experience the same melt-freeze cycles. Figures 3.6c and 3.6f show that the size of commercial Sn powder largely increased after the cycles (size histogram is in Figure S3.16). This is caused by the melting and sintering between Sn particles in the absence of the Al_2O_3 shell. In addition, the supercooling was investigated by checking the temperature difference between the melting points and crystallization temperatures of PCM measured in the DSC curve. In the common sense, the smaller the particles, the higher the supercooling[27]. In contrast, as shown in Figure 3.7, the supercooling (ΔT) of Sn@Al_2O_3-1600 was slightly reduced (104.06°C) compared to commercial Sn powder with a much bigger size (107.27°C). In classical nucleation theory, supercooling is explained as the result from the energy barrier associated with the formation of a solid-liquid interface. Heterogeneous nucleation caused by the pre-exist interface or impurity can lower the energy barrier for cooling and hence can reduce supercooling.[28] In our study, the Al_2O_3 shell of Sn@Al_2O_3

possibly can providing sites[29] for heterogeneous nucleation, which weaken the subcooling.

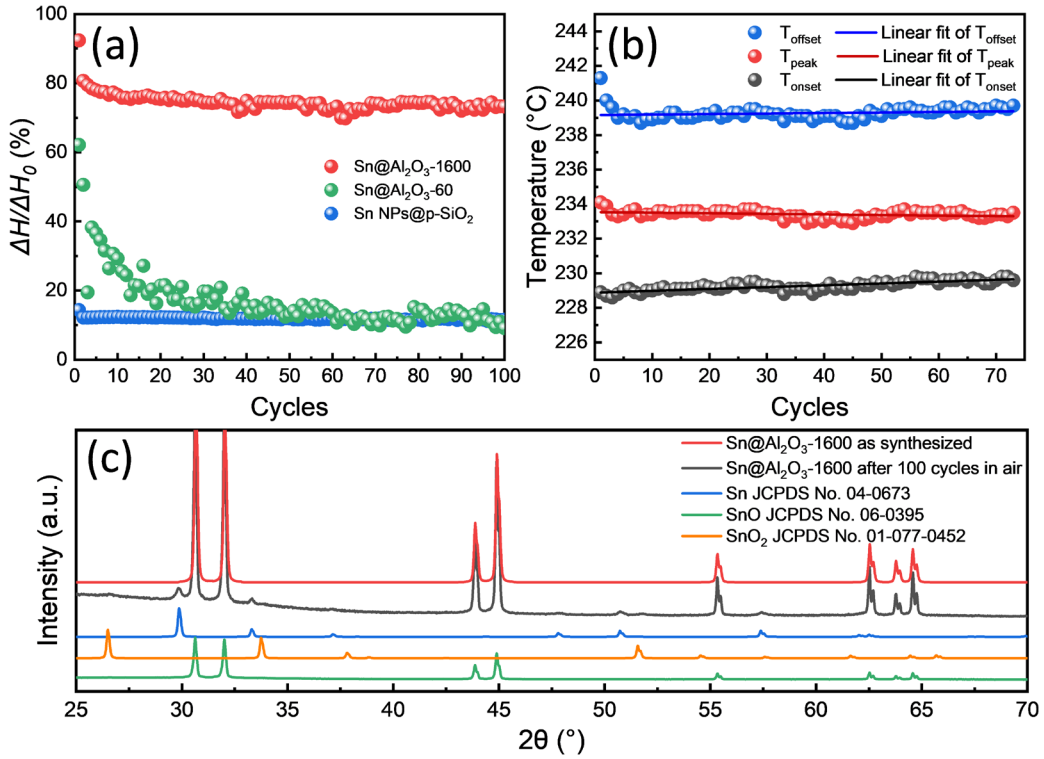

Figure 3.5 Thermal Stability of $Sn@Al_2O_3$.

(a) Relative melting enthalpy in 100 melt-freeze cycles of $Sn@Al_2O_3$-1600 compared with bulk Sn ($\Delta H/\Delta H_0$) during melt-freeze cycles (red spheres) where ΔH and ΔH_0 are enthalpy of melting of $Sn@Al_2O_3$-1600 and that of bulk Sn respectively. Relative melting enthalpy of $Sn@Al_2O_3$-60 and Sn NPs@p-SiO_2 are labeled with green and blue spheres respectively. (b) Onset temperature (T_{onset}), peak temperature (T_{peak}), offset temperature (T_{offset}) of the endothermic peak for each melt-freeze cycle in air atmosphere in a DSC machine. (c) XRD patterns of $Sn@Al_2O_3$-1600 before and after 100 melt-freeze cycles in the air.

The fabricated $Sn@Al_2O_3$ PCM possesses excellent thermal storage properties and stability due to its high PCM content and core-shell structure. To compare our PCM

to other encapsulated low-melting-point metal PCM, we summarized the thermal storage properties for a wide range of materials in Table 1. Sn@Al_2O_3-1600 presented here has a much higher PCM content and better thermal storage stability than the best reported PCM in the Table 3.1, giving them strong potential as thermal storage materials.

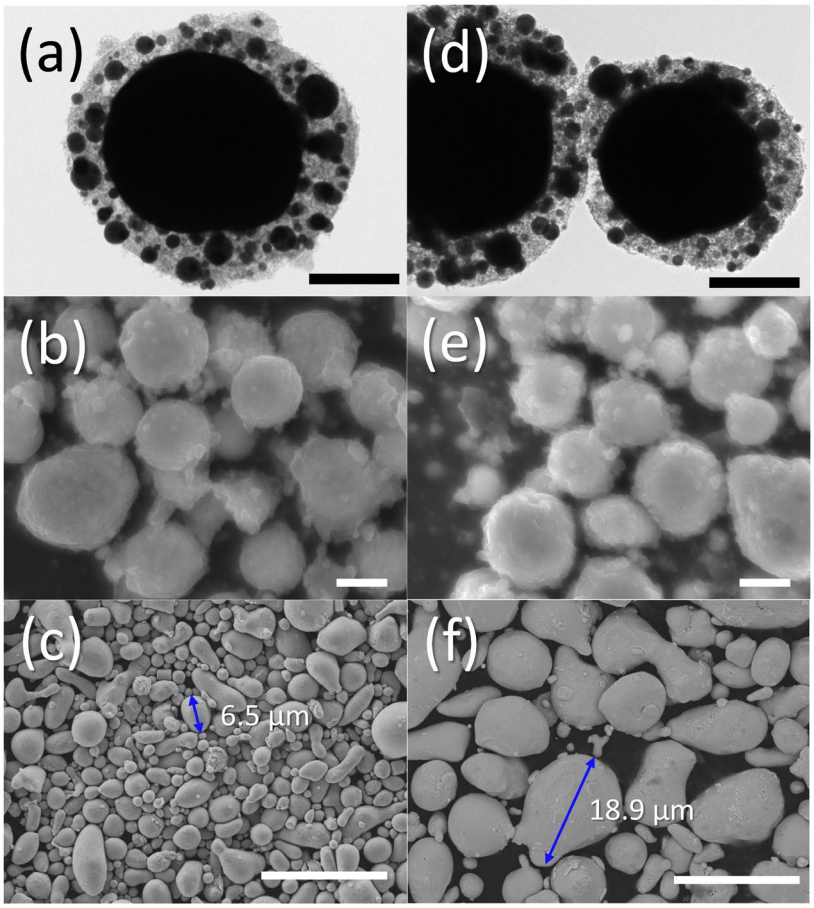

Figure 3.6 Morphology comparison of Sn@Al_2O_3-1600 before and after cyclic test.

Morphology comparison of Sn@Al_2O_3-1600 in TEM and SEM images before (a, b) and after (d, e) 100 melt-freeze cycles in the air. (c, f) The SEM images of commercial Sn powder before and after melt-freeze cycles in the same condition. The scale bar in (a, d) is 500 nm, in (b, e) is 1 µm and that in (c, f) is 20 µm.

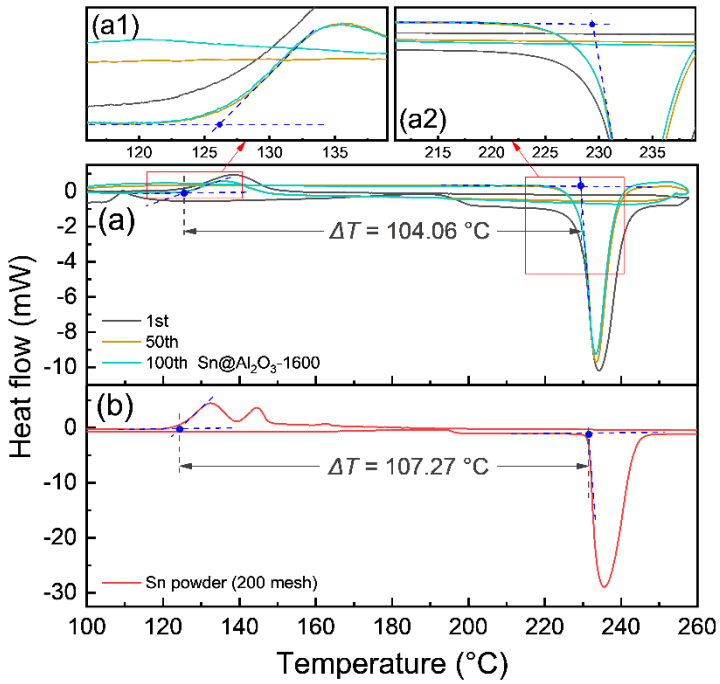

Figure 3.7 Supercooling of $Sn@Al_2O_3$.

DSC curves for melt-freeze cycle of (a) $Sn@Al_2O_3$-1600, (b) commercial Sn powder, showing the existence of supercooling. (a1) and (a2) are the enlarged areas shown by red squares in (a).

Table 3.1 Summary of core-shell encapsulated low-melting-point metal PCMs

Core (PCM)	Shell	Encapsulation Method	T_m (°C)	LH (J g^{-1})	PCM Ratio (wt%)	Cyclic Stability	Ref.
Sn	Al_2O_3	Boehmite treatment	229.1	54.49	92.37	7% decrease between the 2nd and the 100th cycle (in the air, powder form)	This study
Sn	SnO_x	Oxidation	225.5	18	30	15% decrease in the first 50 cycles (powder form)	30
Sn	SnO_x	Oxidation	232.1	48	80	9% decrease in the first 50 cycles (powder form)	30
Sn	SiO_2	Sol-gel	225	29	-	-	31
Sn	SiO_2	Stöber method	228.3	48	80	20 heat/cool cycles test in the nanofluid	32
In	SiO_2	Sol-gel	155.3	19.6	68.8	-	33

T_m = melting temperature; LH = latent heat of melting.

3.4 Conclusions

Alumina-encapsulated Sn particles ($Sn@Al_2O_3$) were successfully prepared and used as the PCM. The fabrication process consisted of a surfactant-free solvothermal synthesis of SnO_2 spheres, boehmite treatment on SnO_2 spheres, calcination in the air, and the final hydrogen reduction to transform SnO_2 to metallic Sn. All the steps of fabrication are facile and low-cost which can be simply applied to the mass production. The as obtained $Sn@Al_2O_3$ particles with a high PCM content (92.37 wt%) showed a stable thermal behavior and morphology during 100 melt-freeze cycles in the air atmosphere.

The $Sn@Al_2O_3$ show a core-shell structure with small Sn nanoparticles dispersed in the shell. The formation of $Sn@Al_2O_3$ structure is a result of boehmite treatment on SnO_2 spheres for the involvement of aluminum. The penetration of boehmite sol (AlOOH) into the SnO_2 spheres contributes the formation of the thick alumina shell, which plays key role for the thermal storage stability. This result also provided the possibility for a facile method for designing new metal nanoparticles with a particle-distributed nanostructure. Our results also demonstrate the great potential of $Sn@Al_2O_3$ particles in the applications as a thermal energy storage material in high temperature conditions which is not suitable for organic PCM.

References

1. Zhao, C. Y.; Zhang, G. H. Review on microencapsulated phase change materials (MEPCMs): Fabrication, characterization and applications. *Renew. Sust. Energ. Rev.* **2011,** *15* (8), 3813-3832.
2. Mohamed, S. A.; Al-Sulaiman, F. A.; Ibrahim, N. I.; Zahir, M. H.; Al-Ahmed, A.; Saidur, R.; Yılbaş, B. S.; Sahin, A. Z. A review on current status and challenges of inorganic phase change materials for thermal energy storage systems. *Renew. Sust. Energ. Rev.* **2017,** *70*, 1072-1089.
3. Pielichowska, K.; Pielichowski, K. Phase change materials for thermal energy storage. *Prog. Mater. Sci.* **2014,** *65*, 67-123.
4. Aftab, W.; Huang, X.; Wu, W.; Liang, Z.; Mahmood, A.; Zou, R. Nanoconfined phase change materials for thermal energy applications. *Energy Environ. Sci.* **2018,** *11* (6), 1392-1424.
5. Alam, T. E.; Dhau, J. S.; Goswami, D. Y.; Stefanakos, E. Macroencapsulation and characterization of phase change materials for latent heat thermal energy storage systems. *Appl. Energ.* **2015,** *154*, 92-101.
6. Liu, M.; Saman, W.; Bruno, F. Review on storage materials and thermal performance enhancement techniques for high temperature phase change thermal storage systems. *Renew. Sust. Energ. Rev.* **2012,** *16* (4), 2118-2132.
7. Ge, H.; Li, H.; Mei, S.; Liu, J. Low melting point liquid metal as a new class of phase change material: An emerging frontier in energy area. *Renew. Sust. Energ. Rev.* **2013,** *21*, 331-346.
8. Yang, X.-H.; Tan, S.-C.; He, Z.-Z.; Liu, J. Finned heat pipe assisted low melting point metal PCM heat sink against extremely high power thermal shock. *Energy Convers. Manag.* **2018,** *160*, 467-476.
9. Hering, W.; Stieglitz, R.; Wetzel, T. Application of liquid metals for solar energy systems. *EPJ Web of Conferences* **2012,** *33*, 03003.
10. Pacio, J.; Singer, C.; Wetzel, T.; Uhlig, R. Thermodynamic evaluation of liquid metals as heat transfer fluids in concentrated solar power plants. *Appl. Therm. Eng.* **2013,** *60* (1), 295-302.
11. Ge, H.; Liu, J. Phase change effect of low melting point metal for an automatic cooling of USB flash memory. *Front. Energy* **2012,** *6* (3), 207-209.
12. Lin, Y.; Cooper, C.; Wang, M.; Adams, J. J.; Genzer, J.; Dickey, M. D. Handwritten, Soft Circuit Boards and Antennas Using Liquid Metal Nanoparticles. *Small* **2015,** *11* (48), 6397-403.

13. Miner, A.; Ghoshal, U. Cooling of high-power-density microdevices using liquid metal coolants. *Appl. Phys. Lett.* **2004,** *85* (3), 506-508.
14. Ma, K.-Q.; Liu, J. Heat-driven liquid metal cooling device for the thermal management of a computer chip. *J. Phys. D: Appl. Phys.* **2007,** *40* (15), 4722-4729.
15. Ghadimi, A.; Saidur, R.; Metselaar, H. S. C. A review of nanofluid stability properties and characterization in stationary conditions. *Int. J. Heat Mass Transfer* **2011,** *54* (17), 4051-4068.
16. Cingarapu, S.; Yang, Z.; Sorensen, C. M.; Klabunde, K. J. Synthesis of indium nanoparticles: digestive ripening under mild conditions. *Inorg. Chem.* **2011,** *50* (11), 5000-5.
17. Hsu, T.-H.; Chung, C.-H.; Chung, F.-J.; Chang, C.-C.; Lu, M.-C.; Chueh, Y.-L. Thermal hysteresis in phase-change materials: Encapsulated metal alloy core-shell microparticles. *Nano Energy* **2018,** *51*, 563-570.
18. Liu, M.; Ma, Y.; Wu, H.; Wang, R. Y. Metal Matrix–Metal Nanoparticle Composites with Tunable Melting Temperature and High Thermal Conductivity for Phase-Change Thermal Storage. *ACS Nano* **2015,** *9* (2), 1341-1351.
19. Liu, M.; Wang, R. Y. Phase change nanocomposites with tunable melting temperature and thermal energy storage density. *Nanoscale* **2013,** *5* (16), 7234-7237.
20. Zhu, S.; Nguyen, M. T.; Fumoto, K.; Kanie, K.; Muramatsu, A.; Yonezawa, T. Sn Nanoparticles Confined in Porous Silica Spheres for Enhanced Thermal Cyclic Stability. *ACS Appl. Nano Mater.* **2018,** *1* (8), 4073-4082.
21. Muta, H.; Kurosaki, K.; Uno, M.; Yamanaka, S. Thermoelectric properties of constantan/spherical SiO_2 and Al_2O_3 particles composite. *J. Alloys Compd.* **2003,** *359* (1), 326-329.
22. Persson, K. Materials Data on $AlSnO_3$ (SG:194) by Materials Project. **2014**.
23. Menon, S. G.; Choudhari, K. S.; Shivashankar, S. A.; Chidangil, S.; Kulkarni, S. D. Microwave solution route to ceramic $ZnAl_2O_4$ nanoparticles in 10 minutes: inversion and photophysical changes with thermal history. *New J. Chem.* **2017,** *41* (13), 5420-5428.
24. Lai, S. L.; Guo, J. Y.; Petrova, V.; Ramanath, G.; Allen, L. H. Size-Dependent Melting Properties of Small Tin Particles: Nanocalorimetric Measurements. *Phys. Rev. Lett.* **1996,** *77* (1), 99-102.
25. O'Neill, M. J. The Analysis of a Temperature-Controlled Scanning Calorimeter. *Anal. Chem.* **1964,** *36* (7), 1238-1245.
26. Höhne, G. W. H.; Cammenga, H. K.; Eysel, W.; Gmelin, E.; Hemminger, W. The temperature calibration of scanning calorimeters. *Thermochim. Acta* **1990,** *160* (1), 1-12.

27. Turnbull, D. The Subcooling of Liquid Metals. *J. Appl. Phys.* **1949,** *20* (8), 817-817.
28. Banhart, F.; Hernández, E.; Terrones, M. Extreme Superheating and Supercooling of Encapsulated Metals in Fullerenelike Shells. *Phys. Rev. Lett.* **2003,** *90* (18), 185502.
29. Safari, A.; Saidur, R.; Sulaiman, F. A.; Xu, Y.; Dong, J. A review on supercooling of Phase Change Materials in thermal energy storage systems. *Renew. Sust. Energ. Rev.* **2017,** *70*, 905-919.
30. Navarrete, N.; Gimeno-Furio, A.; Mondragon, R.; Hernandez, L.; Cabedo, L.; Cordoncillo, E.; Julia, J. E. Nanofluid based on self-nanoencapsulated metal/metal alloys phase change materials with tuneable crystallisation temperature. *Sci. Rep.* **2017,** *7* (1), 17580.
31. Lai, C.-C.; Chang, W.-C.; Hu, W.-L.; Wang, Z. M.; Lu, M.-C.; Chueh, Y.-L. A solar-thermal energy harvesting scheme: enhanced heat capacity of molten HITEC salt mixed with Sn/SiO_x core–shell nanoparticles. *Nanoscale* **2014,** *6* (9), 4555-4559.
32. Cingarapu, S.; Singh, D.; Timofeeva, E. V.; Moravek, M. R. Nanofluids with encapsulated tin nanoparticles for advanced heat transfer and thermal energy storage. *Int. J. Energy Res.* **2014,** *38* (1), 51-59.
33. Hong, Y.; Ding, S.; Wu, W.; Hu, J.; Voevodin, A. A.; Gschwender, L.; Snyder, E.; Chow, L.; Su, M. Enhancing Heat Capacity of Colloidal Suspension Using Nanoscale Encapsulated Phase-Change Materials for Heat Transfer. *ACS Appl. Mater. Interfaces* **2010,** *2* (6), 1685-1691.

Chapter 4.

SiO_2 Encapsulated Core-Shell Nanoparticles: Structure Transformation via Liquid Metal Diffusions

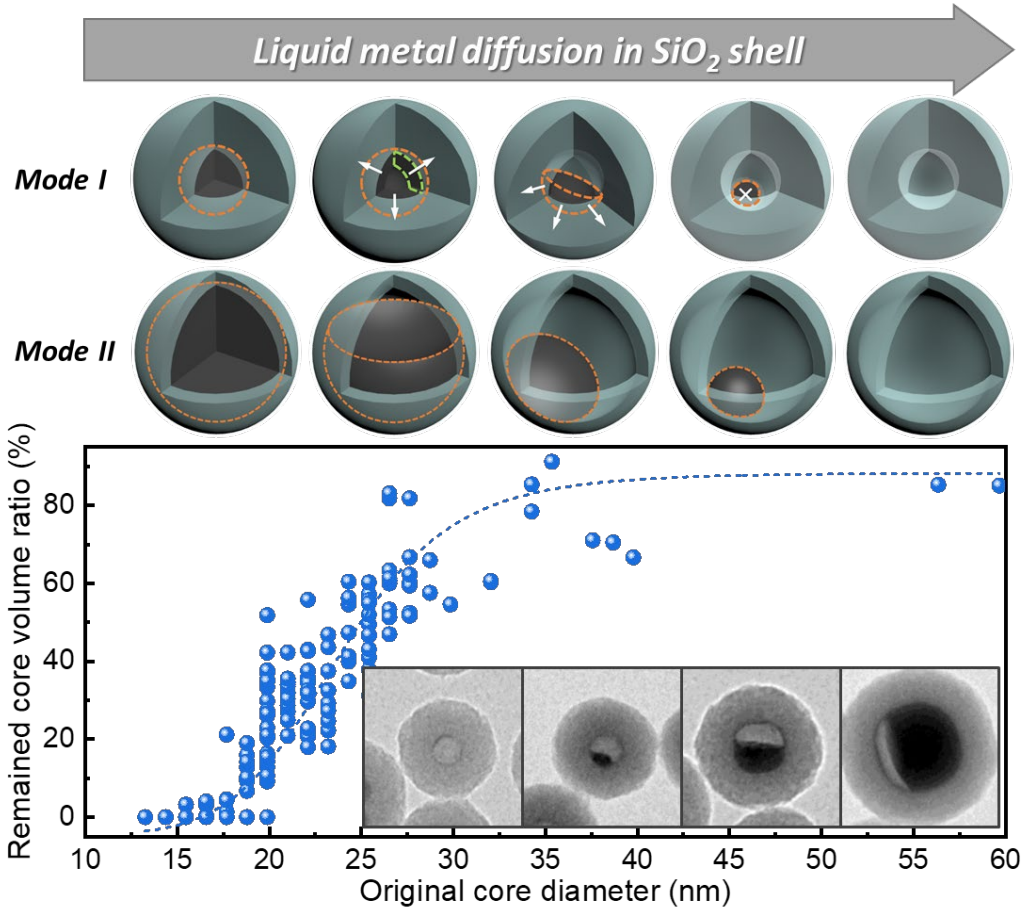

Abstract

Precise design of hollow nanostructure can be realized via various approaches that developed in last two decades, endowing the nanomaterials with unique structures and outstanding performances, showing their talents in a broad range of fields. Herein, we demonstrate the formation of SnO_2@SiO_2 hollow nanostructures, for the first time, by diffusion of liquid state Sn cores in Sn@SiO_2 core-shell nanoparticles with real-time observation via in situ transmission electron microscopy (TEM). Based on the in-situ results, a designed transformation of nanoparticle structure from core-shell Sn@SiO_2 to yolk-shell Sn@SiO_2 and hollow SnO_2@SiO_2 is demonstrated, showing the controllable structure from designed starting core-shell Sn@SiO_2 nanoparticles via liquid state Sn diffusion in SiO_2 shell. The present approach expands the toolbox for the design and preparation of yolk-shell and hollow nanostructure, thus provides us a new strategy in fabrication of more complicated nanostructures.

4.1 Introduction

Hollow nanoparticles were applied to a broad range of applications, such as catalyst,[1] energy conversion and storage [2], sensors [3] and biomedicines due to their unique properties including large specific surface area, low density, etc., determined by their ingenious structures. Much work so far has focused on the synthesis of hollow nanoparticles, which basically can be classified into three strategies: (1) hard templating pathway, (2) soft templating pathway, and (3) self-templating synthetic route which includes surface-protected etching, Ostwald ripening, the Kirkendall effect, and galvanic replacement.[5-11] Generally, all these strategies consist of two basic steps, including (1) formation of precursor for hollow structure (e.g., core-shell nanostructure), and (2) creation of hollow space by various methods including etching of cores, removal of templates, net outward diffusion, etc.[11]

Until now, the formation of hollow structure in most of the research was carried out and observed via ex situ techniques, in which the involved transient information during the hollowing process was missing. To gain more insight, *in situ* transmission electron microscopy (TEM) was used in recent research to observe the hollowing process caused by galvanic reaction [13, 14] and the Kirkendall effect [15, 16]. E. Sutter *et al.* used liquid-cell electron microscopy to investigate galvanic replacement reactions between Ag nanoparticle templates and aqueous Pd salt solutions. They observed the transformation from Ag nanoparticles into hollow Ag-Pd nanostructures.[13] Chee *et al.* used liquid-cell electron microscopy for observation of hollow Ag nanostructure with the void formation due to the nanoscale Kirkendall effect occurred in conjunction with

galvanic replacement.[15] Several studies have reported the *in situ* observation of hollow structure formation by removing core templates from the core-shell structures. Yang *et al.* observed that when exposing to electron beam irradiation, $ZnO@Al_2O_3$ core-shell nanowires can be transformed into $ZnO@Al_2O_3$ composite nanotubes via local etching of ZnO cores.[17] Zhu *et al.* observed the transformation of Se-C core-shell NPs into yolk-shell NPs and hollow NPs by electron beam irradiation, which induced the evaporation of embedded Se.[17]

In this study, we report the formation of $SnO_2@SiO_2$ hollow nanostructures, for the first time, by diffusion of liquid state Sn cores in $Sn@SiO_2$ core-shell nanoparticles with real-time observation via in situ TEM. According to the in-situ observation, diffusion of liquid state Sn at 300°C contributes to the moving-out of embedded Sn cores, creating the hollow space inside SiO_2 shell structures. Based on this understanding, to the best of our knowledge, we demonstrate the synthesis of yolk-shell $Sn@SiO_2$ and hollow $SnO_2@SiO_2$ nanoparticles from as-designed starting core-shell $Sn@SiO_2$ nanoparticles, for the first time, showing the nanostructure control via liquid state metal diffusion in SiO_2 shell structure. The present approach expands the toolbox for the design and preparation of yolk-shell and hollow nanostructure, provides a new strategy in fabrication of more complicated nanostructures.

4.2 Methods

4.2.1 Synthesis of Sn nanoparticles

The Sn nanoparticles were synthesized using a well-developed method.[18] 25 mL of oleylamine was vacuum dried in a 50-mL three-necked flask at 140°C for 1.5 h, then naturally cooled down to 30°C. Anhydrous $SnCl_2$ (0.5 mmol) (min. 98%, Junsei, Tokyo, Japan) were added into the flask before heating to 140°C and holding for extra 30 minutes to remove the moisture. Afterwards, the flask was heated to 190°C under the atmosphere of argon with constant stirring, followed by an injection of 3.6 mmol $Li[N(SiMe_3)_2]$ (1.0 M in toluene, Aldrich) and a second injection of 0.6 mmol Diisobutylaluminium hydride (DIBAH, 1.0 M in toluene, Kanto, Tokyo, Japan) within 10 s. The reaction solution became brown then gradually turned to black. The solution was stirred at 180°C for 1 h to ensure the near-complete reaction of metal precursor, then cooled down to 50°C in an ice-water bath. 500 μL of dried oleic acid (OA, Junsei, Tokyo, Japan) were added before cooling down to 30°C. The obtained solution was washed with ethanol and centrifuged (8000 rpm, 5 min). The precipitate was redispersed in a mixture solvent (6 mL, volume ratio: OA: hexane = 1: 50) and then washed with ethanol before final redispersion in 25 mL of hexane as a stock solution. In addition, $InSn_4$ nanoparticles were prepared in a similar way by using $InCl_3$ mixed with $SnCl_2$ at certain molar ratios as the precursor.

4.2.2 Synthesis of $Sn@SiO_2$ core-shell nanoparticles

To encapsulate Sn nanoparticles with uniform SiO_2 shell, a modified reversed micro-emulsion method was used. For a typical synthesis, 12 mL of an Sn nanoparticle-

dispersed stock solution was mixed with 0.61 g (0.594 mL) of polyethylene glycol mono-4-nonylphenyl ether (n = approx. 5, TCI, Tokyo, Japan) and 62 μL of deionized water (purified using a PureLabo system, Organo/ELGA, >18 MΩ). This emulsion was sonicated for 15 min to produce good dispersions of the NPs without aggregation. Afterward, 50 μL of TEOS (Tetraethyl orthosilicate) were added under vigorous stirring (800 rpm). After 30 min the hydrolysis and condensation of TEOS were triggered upon injection of 30 μL of ammonia solution (min. 28.0 %, Junsei, Tokyo, Japan). The mixture was stirred at 400 rpm for 10 h. Afterward, the obtained samples (Sn@SiO_2 core-shell nanoparticles) were washed with ethanol three times and finally dried in vacuum at room temperature. In particular, the thickness of SiO_2 shell can be easily tuned by changing the concentration of Sn nanoparticle-dispersed stock solution.

4.2.3 In situ TEM observation

In situ TEM observations were carried out using a dedicated 1000 kV JEM-1000K RS TEM (JEOL, Tokyo, Japan) operated at 1000 kV. A wire-type heating holder (JEOL, EM-Z081834SWHH, Tokyo, Japan) was used. The powder samples (Sn@SiO_2) were loaded on a tungsten wire and heated up to 300°C under vacuum. TEM images were recorded with a charge-coupled device with an exposure time of typically 0.5 s and 5 s. The electron beam current flux for strong electron beam condition was 37.3 $pA \cdot cm^{-2}$, and for weak electron beam condition was 2.7 $pA \cdot cm^{-2}$, as measured with a Faraday gauge.

4.2.4 Ex situ TEM observation

The ex situ TEM observation of $Sn@SiO_2$ was carried out using a conventional TEM (JEM-2000FX microscope, JEOL) operated at 200 kV and a high-resolution field-emission gun TEM (JEM-ARM200F Cold, JEOL) operated at 200 kV at room temperature and under a pressure of 10^{-6} Pa.

4.3. Results and discussion

4.3.1 Structure characterization

The modified reverse-emulsion method realizes uniform and controllable SiO_2 encapsulation of Sn nanoparticles, producing $Sn@SiO_2$ core-shell nanoparticle samples with two dimensions: a) 20-nm core with 20-nm shell (Figure S4.2, Supporting Information); b) 30-nm core with 8-nm shell (Figure S4.3, Supporting Information), which were loaded on a tungsten wire (showed in Figure 4.1a and b, respectively, in vacuum at 25°C), used as the heater for temperature control, inside a TEM heating holder for in situ TEM observation, respectively (Figure S4.1, Supporting Information). Several $Sn@SiO_2$ core-shell nanoparticles in Figure 4.1a were examined by selected area electron diffraction (SAED), the diffraction spots in correspondent pattern shown in Figure 4.1c are indexed to tetragonal Sn (JCPDS No. 04-0673), indicating the existence of metallic Sn cores. After finishing the whole heating process (from 25°C to 300°C, in vacuum) in TEM and cooling down to 25°C, most of the Sn cores disappeared and some decreased in size, forming hollow and yolk-shell nanostructures as shown in

Figure 4.1d-f. $Sn@SiO_2$ nanoparticles shown in Figure 4.1a were observed under a strong electron beam condition (37.3 $pA \cdot cm^{-2}$). In this condition, significant deformation of SiO_2 shells occur with interconnections between them (Figure 4.1d). Meanwhile, according to the SAED pattern of the hollow and yolk-shell nanostructures in Figure 4.1d (Figure S4.4), the rings are indexed to SnO_2 (JCPDS No. 41-1445) while several dim spots were indexed to the (200) and (101) plane of tetragonal Sn (JCPDS No. 04-0673), demonstrating the transformation of Sn to SnO_2 occurred during heating process with observation. A weak electron beam condition (2.7 $pA \cdot cm^{-2}$) was applied when observing $Sn@SiO_2$ nanoparticles shown in Figure 4.1b. After heating, most of the Sn cores disappeared, leaving hollow SiO_2 structure remained without significant deformation (Figure 4.1f), in which the existence of SnO_2 were exhibited by indexing the corresponding SAED pattern (inset image in Figure 4.1f) to SnO_2 (JCPDS No. 41-1445).

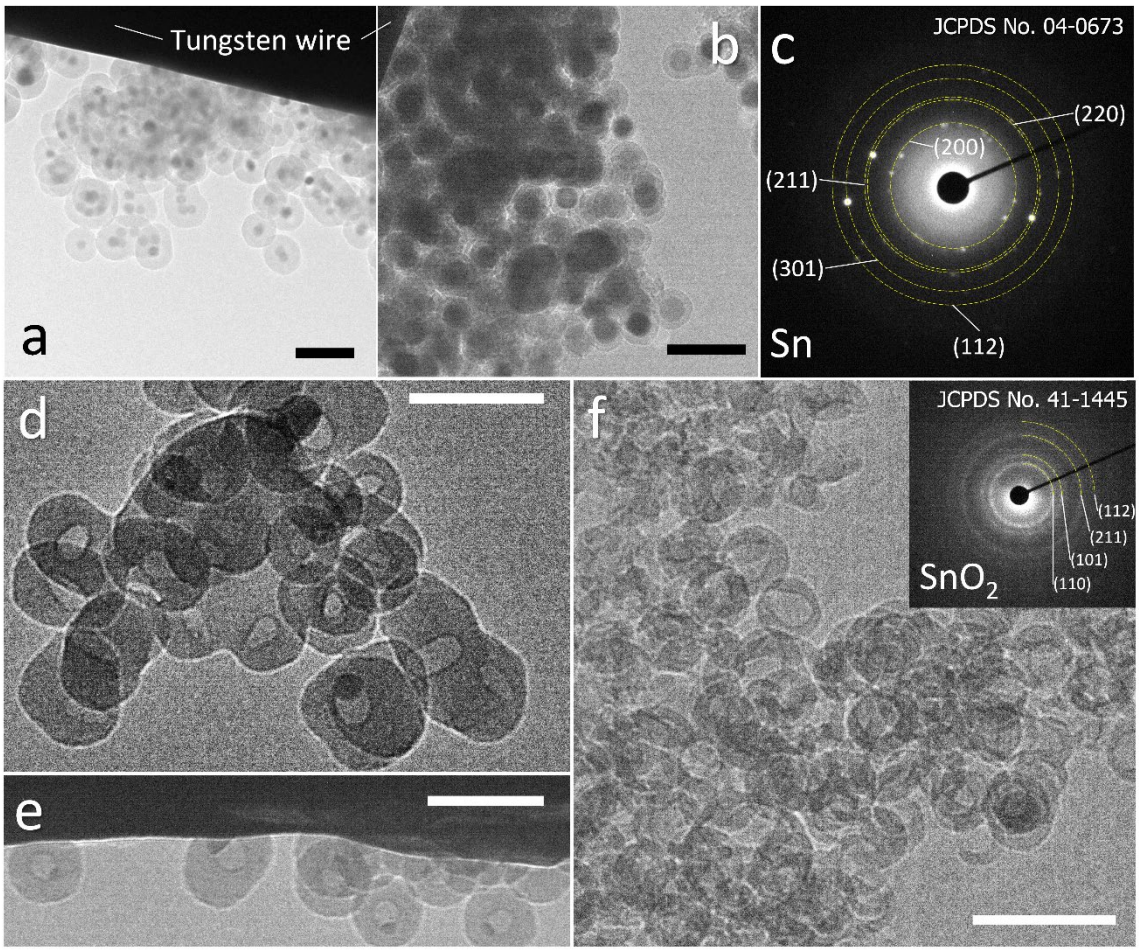

Figure 4.1 Morphology of $Sn@SiO_2$ before and after heating in TEM.

(a, b) TEM image of $Sn@SiO_2$ samples, with two different Sn core sizes (a: 20 nm, b: 30 nm) and shell thicknesses (a: 20 nm, b: 8 nm), which are loaded on a tungsten wire inside a heating holder observed in vacuum at room temperature (25°C), respectively. (c) The SAED pattern of $Sn@SiO_2$ shown in (a). TEM images of $Sn@SiO_2$ after heating from room temperature (25°C) to 300°C in vacuum performed in a high-voltage TEM operated in 1000 kV in (d, e) strong electron beam condition (37.3 $pA{\cdot}cm^{-2}$) and (f) weak beam condition (2.7 $pA{\cdot}cm^{-2}$), inset: SAED pattern shows as-formed SnO_2. All scale bars are 100 nm.

4.3.2 Dynamic motions of Sn nanodroplets inside SiO_2 structure

We first discuss the dynamic motions of Sn nanodroplets inside the deforming SiO_2 structure at an elevated temperature under electron beam irradiation according to the detailed structure evolution and transformation that recorded in situ during the heating process. When temperature exceeds the melting point (T_m) of metallic Sn (bulk: 231°C, 20 nm in diameter: 223°C),[19] the SiO_2 encapsulated solid-state Sn cores are transformed to a liquid state as Sn nanodroplets. Figure 4.2a show dynamic motions of Sn nanodroplets inside SiO_2 structure at 300°C in vacuum under electron beam irradiations (strong electron beam condition, 37.3 $pA \cdot cm^{-2}$) captured from movie (Supplementary Movie 1, Supporting Information). As the initial state, Sn cores A and B, with the initial diameters of 16.9 and 21.2 nm, respectively, were located at the central positions of two adjacent Sn@SiO_2 core-shell nanoparticles with a clear boundary in between (Figure 4.2a, $t = t_0$). As the heating processed, both core A and B decreased in size (Figure 4.2a, $t = t_0 + 314$ s) and core A started to move from the center position (Figure 4.2a, $t = t_0 + 322$ s). The moving directions of Sn cores are shown as the blue arrows marked in the TEM images according to the movie. By $t_0 + 362$ s, dynamic motions in random directions inside SiO_2 shell are observed from the movie. After $t_0 + 368$ s, core A started to move along the fixed direction toward core B and reached the edge of SiO_2 shell at $t_0 + 391$ s. Meanwhile, core B moved in a similar way toward the edge of SiO_2 shell and met core A at $t_0 + 421$ s. After that, both core A and B gradually became invisible by contrast in SiO_2 structure (Figure 4.2a, $t = t_0 + 556$ s). The observed moving and disappearance of Sn cores may give evidence for Sn diffusion

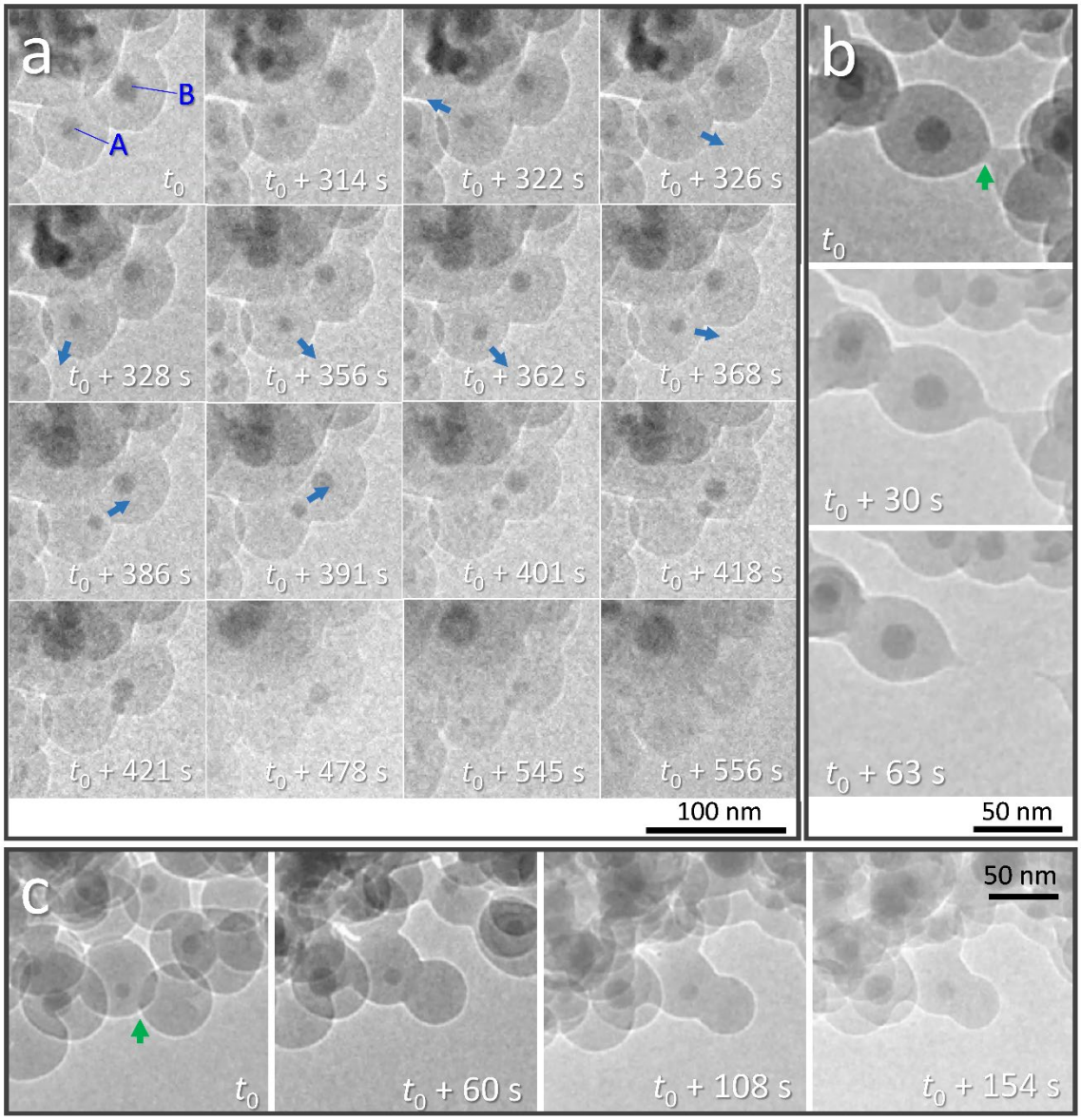

Figure 4.2 In-situ observation of $Sn@SiO_2$ at 300°C in vacuum at strong electron beam condition (37.3 $pA \cdot cm^{-2}$).

(a) Random motion and gradual decrease in size of Sn droplets that embed inside SiO_2 shell indicate the possible diffusion of Sn at an elevated temperature (300°C). The blue arrows show the moving direction of Sn droplets according to the movie. Deformation of SiO_2 shell structure occurred during observation: (b) breakage of connected SiO_2 shell of two $Sn@SiO_2$ core-shell particles and (c) connection of two individual particles are shown (marked with green arrows).

inside the SiO_2 structure. It is worth mentioning that no clear cavity can be observed after Sn cores changed their positions during heating, which probably can be explained by the structural deformation and viscous flow of SiO_2 under high-dose electron beam irradiation.[21-23]

Furthermore, the structure deformation of SiO_2 shell was clearly observed in Figure 4.2b and c during heating (300°C) under electron beam irradiation (37.3 $pA \cdot cm^{-2}$). Figure 4.2b shows the breakage of two connected $Sn@SiO_2$ core-shell nanoparticles. The necking existed initially between these two $Sn@SiO_2$ core-shell nanoparticles (Figure 4.2b, $t = t_0$, marked by a green arrow), then stretched out in length (Figure 4.2b, $t = t_0 + 30$ s), and finally broke accompanied with tail-like morphology (Figure 4.2b, $t = t_0 + 63$ s) (Supplementary Movie 2, Supporting Information). Figure 4.2c exhibited the merging and connection of two individual particles. The green arrow in Figure 4.2c shows the overlap and a clear boundary between SiO_2 shells by contrast (Figure 4.2c, $t = t_0$). With heating processed, this boundary turned blur (Figure 4.2c, $t = t_0 + 60$ s) and then disappeared (Figure 4.2c, $t = t_0 + 108$ s), indicating the necking between SiO_2 shells and merging of two individual particles, respectively (Supplementary Movie 2, Supporting Information). It is reasonable to believe that these evolutions of SiO_2 structure was not induced by simply heating, since in our case, the heating temperature 300°C is far below ~0.7 T_g (glass-transition temperature) of SiO_2 (1373 K), which is not able to contribute viscous flow of SiO_2 for significant deformation rate.[23] In addition, the temperature increase caused by energy transfer from electron beam under our condition is also far below 0.7 T_g according to the calculation

given by Zheng *et al*.[20] To minimize the effect from electron beam irradiation, Sn@SiO_2 core-shell nanoparticles distributed in other places, which were far from the focus area for movie recording during the heating process, were observed after cooling down to 25°C. Reduced deformation is observed compared to the SiO_2 structure in focus area, whereas the hollow nanoparticles still formed (Figure 4.1e).

4.3.3 Outward diffusion of liquid-state Sn cores

From the above discussion, the observed dynamic movements and vanishing of Sn cores show the possible occurrence of Sn diffusion in SiO_2 structure. Figure 4.3 shows the in-situ observation of two different pathways: mode I and mode II, for the disappearance of Sn cores in SiO_2, providing a visual demonstration of hollow SiO_2 formation induced by melting and diffusion of Sn.

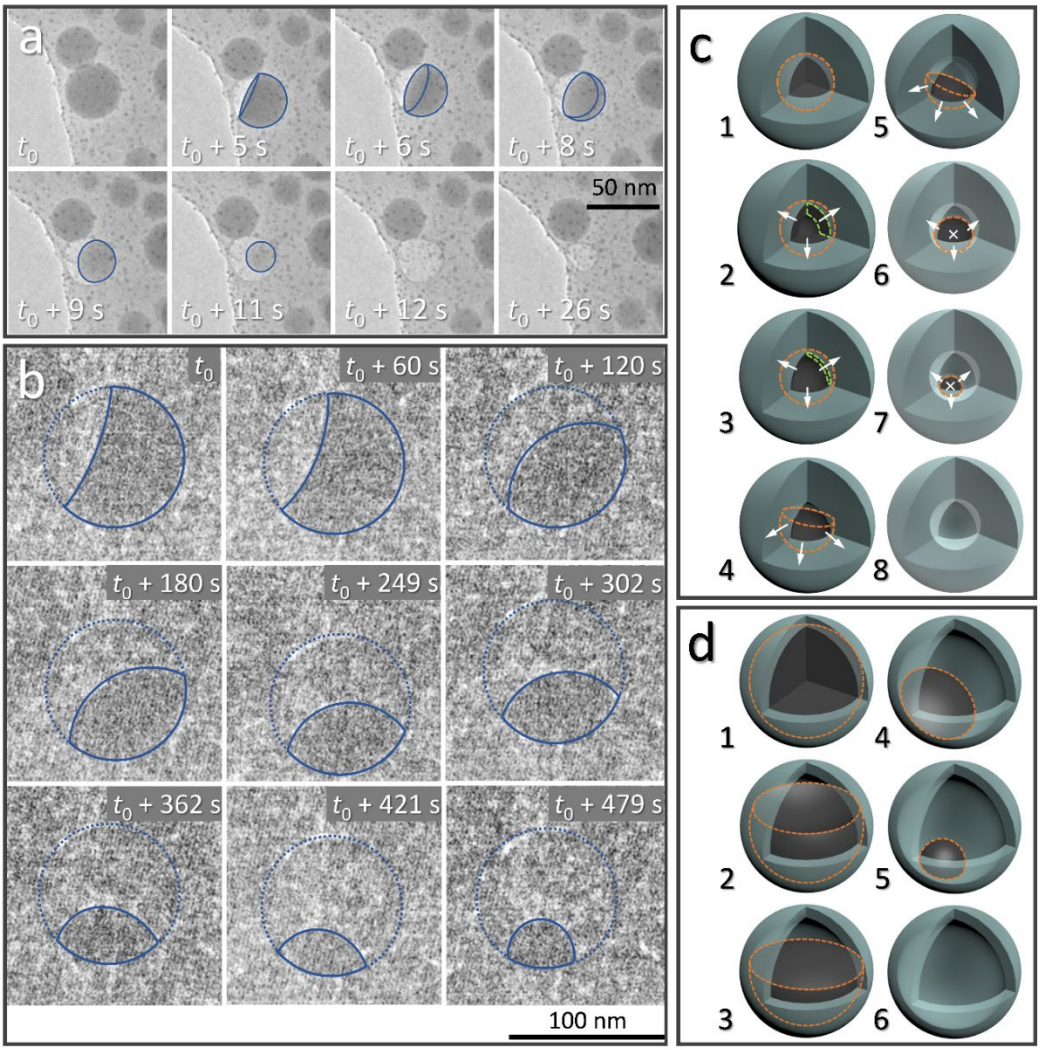

Figure 4.3 In-situ observation of the disappearance of single liquid-state Sn core.

In-situ observation of the disappearance of single liquid-state Sn core in (a) strong electron beam condition (37.3 pA·cm^{-2}) (mode I: balloon-like liquid-state Sn layer forms and decreases in thickness due the outward diffusion of Sn into the outside SiO_2 structure, and disappears in seconds) and (b) weak electron beam condition (2.7 pA·cm^{-2}) (mode II: the remained Sn core slowly decreases in size due to the diffusion of Sn, and gradually disappears) at 300°C in vacuum, respectively. The blue solid line in (a) and (b) show the outline of remained Sn core during diffusion process. The position of SiO_2 shell in (b) is outlined by a blue dash line. Schematics of two different diffusion modes: (c) mode I and (d) mode II, illustrating the diffusion process that shown in (a) and (b). In (c) and (d), the outline of remained Sn core and the thickness of liquid Sn layer are marked by orange dash lines and green dash lines, respectively. The white arrows are used for showing diffusion directions (white crosses "x" represent the arrow directed into the page).

Figure 4.3a shows the vanishing of Sn cores inside SiO_2 structure at 300°C in mode I, captured from the movie (Supplementary Movie 3, Supporting Information). This process was illustrated in Figure 4.3c (8 stages marked by number 1−8). The Sn core with the size of 38.5 nm is embedded in deformed SiO_2 structure which derived from the interconnected SiO_2 shell structure, induced by electron beam irradiation (strong electron beam condition, 37.3 $pA \cdot cm^{-2}$) as we discussed above. At 300°C, this Sn core first melted to a liquid droplet (stage 1 in Figure 4.3c, outlined by an orange dash line), and showed a decreased contrast compared with the as-formed ultra-small particles distributed around, indicating that the Sn core did not exist as a filled spherical droplet but a balloon-like spherical liquid layer that adhered on the inner surface of cavity in SiO_2 structure (Figure 4.3a, $t = t_0$) (stage 2 and 3 in Figure 4.3c, the layer was shown by using green dash line). It is reasonable to consider that uniform diffusion of Sn may occur throughout the direction that perpendicular to the Sn-SiO_2 interface (shown by white arrows in stage 2 and 3 in Figure 4.3c). As the diffusion proceeded, the liquid Sn layer decreased in thickness (stage 3 in Figure 4.3c) then broke with the appearance of a gap (Figure 4.3a, $t = t_0 + 5$ s) (stage 4 in Figure 4.3c). The balloon-like spherical liquid layer turned to bowl-like structure and then vanished quickly with the decrease in the area of Sn-SiO_2 interface (Figure 4.3a, $t_0 + 8$ s ~ $t_0 + 11$ s) (stage 4-7 in Figure 4.3c), finally forming the hollow space in SiO_2 structure (Figure 4.3a, $t_0 + 12$ s) (stage 8 in Figure 4.3c). In addition, the edge between the single and overlapped liquid Sn layer makes it easy to distinguish the liquid Sn layer by contrast (Figure 4.3a, $t_0 + 5$

s ~ t_0 + 8 s). Moreover, the left hollow space also shrunk with the further deformation of SiO_2 structure (Figure 4.3a, $t = t_0$ + 26 s).

In a weak electron beam condition (2.7 pA·cm^{-2}), another type of outward Sn diffusion was observed at 300°C in vacuum, named mode II, shown in Figure 4.3b, which are captured from the movie (Supplementary Movie 4, Supporting Information). Figure S4.5a shows that a Sn@SiO_2 core-shell nanoparticle (core diameter: ca. 90 nm, shell thickness: ca. 8 nm) (blue arrow) with a small inside cavity and numerous hollow-structure SiO_2 nanoparticles surrounded was selected. The whole hollowing process is illustrated in Figure 4.3d, in which Sn cores are outlined with orange dash lines. At the beginning, a part of liquid Sn core was diffused out forming a cavity inside the SiO_2 shell (Figure 4.3b, $t = t_0$) (stage 2 in Figure 4.3d), then the left Sn core decreased in size with time increasing (Figure 4.3b, t_0 + 60 s ~ t_0 + 479 s) (stage 2-4 in Figure 4.3d) until the Sn core disappeared completely (Figure S4.5b, Supporting Information) (stage 6 in Figure 4.3d). In this process, the free surface of Sn core which is initially concave, turns nearly flat, finally becomes convex and disappears. According to the observation, Sn may diffuse through the interconnected SiO_2 shell structure (Figure S4.5a, Supporting Information) since no leakage or outside Sn particles were formed during our observation. Moreover, the wetting angle that shown in Figure 4.3b at $t = t_0$ + 60 s was less than 90° and kept changing as heating proceeded, displaying a reversible wetting transition on the curved inner surface of the shell. Combining the results from Figure 4.3a, it indicates that the embedded Sn droplets can completely wet the inner surface of the SiO_2 shell in the as-prepared Sn@SiO_2 core-shell structure.

Several previous studies showed in-situ observation of core-removal hollowing process including local etching of cores[24], evaporation of cores[17], draining away of liquid cores[25], etc. Our observation showed a core-removal hollowing process by diffusion of liquid-state metal cores inside shell structure, which has not been reported to the best of our knowledge.

It is worth mentioning that ultra-small liquid-state Sn nanodroplets (diameter < 5 nm) appeared and distributed in SiO_2 structure accompanied with the disappearance of Sn cores during heating process (Figure 4.3a). To collect more information on this phenomenon, a SiO_2 sphere distributed with ultra-small nanodroplets attached on the tungsten wire was observed during heating (Supplementary Movie 5, Supporting Information). The captured images are shown in Figure 4.4a. During the heating process, the SiO_2 structure kept shrinking with the shape transformation from a sphere to a spherical cap ($t_0 \sim t_0 + 107$ s). Meanwhile, no change in the area of contact interface (red double arrow, $t_0 + 4$ s and $t_0 + 104$ s) was observed. To show the shrinkage more clearly, a blue dash line triangle was drawn with vertices a, b and c located at the positions of three characteristic Sn nanodroplets ($t = t_0$). The change in size and shape of these triangles shows the shrinkage of SiO_2, and the relative positions of these triangles indicate that the SiO_2 structure did not move but clung to the tungsten wire during the observation. The mean diameter of distributed Sn nanodroplets inside SiO_2 in each image is measured and accounted to show the growth of as-formed nanodroplets (Figure 4.4b), which increased from 1.8 nm to 2.9 nm. The corresponding size histograms are shown in Figure S4.6. Notably, during our observation, bigger Sn

nanodroplets grew with time while small ones gradually disappeared, resulting in a decrease in the total number of Sn nanodroplets (Figure 4.4c). This phenomenon indicates the occurrence of Ostwald ripening which is the result of the reduction in interface energy by diffusion process inside SiO_2 structure.[26, 27]

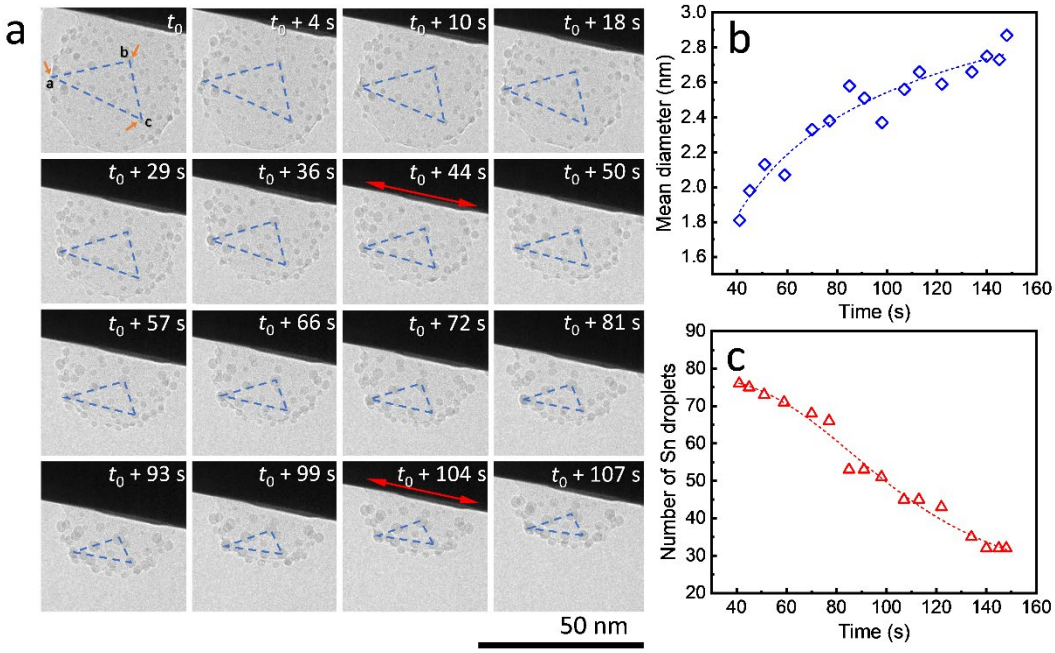

Figure 4.4 Ostwald ripening in SiO_2 structure.

(a) Disappearance and growth of ultra-small Sn nanodroplets formed after disappearance of Sn cores during in-situ TEM observation (strong electron beam condition, 37.3 pA·cm^{-2}) at 300°C in vacuum. The change in shape and size of the blue dash line triangle with vertices a, b and c located at the positions of three typical particles (t_0) indicates the shrinkage of SiO_2 structure during the observation. (b) Increase in mean diameter and (c) decrease in number of ultra-small Sn nanodroplets in the observation field throughout the time. The dash lines in (b) and (c) show the increase and decrease tendency, respectively.

4.3.4 Controllable nanostructure of $Sn@SiO_2$

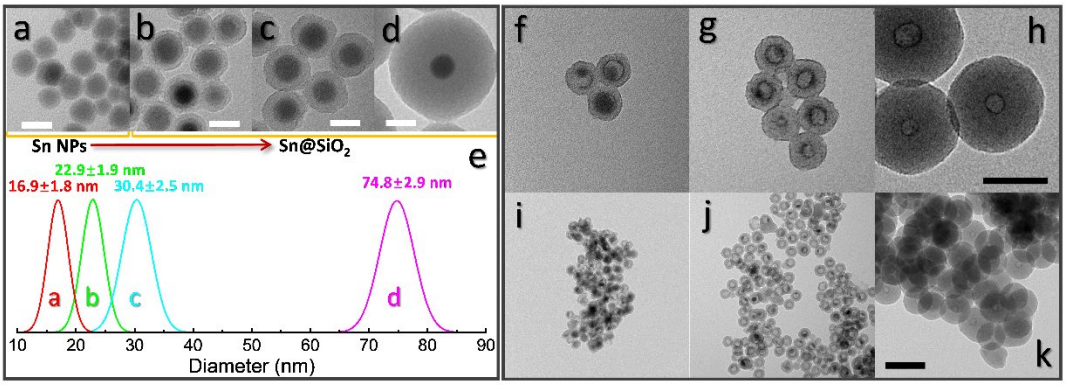

Figure 4.5 Formation of yolk-shell and hollow NPs from $Sn@SiO_2$ with different shell thicknesses but same Sn core.

TEM images of (a) Sn nanoparticles used as the cores of $Sn@SiO_2$ core-shell nanoparticles and $Sn@SiO_2$ core-shell nanoparticles with the shell thickness of (b) 3.0 nm, (c) 6.8 nm and (d) 29.0 nm, respectively. (e) Size histogram of Sn nanoparticles and $Sn@SiO_2$ shown in (a-d). (f-k) TEM images of $Sn@SiO_2$ core-shell nanoparticles, with various shell thickness ((f, i): 3.0 nm, (g, j): 6.8 nm, (h, k): 29.0 nm), after loading in a sealed Al pan and heating from 25°C to 300°C at a ramping rate of 10°C/min in a DSC. Scale bars for (a-d) are 20 nm, for (f-h) are 50 nm, and for (i-k) are 100 nm.

To further investigate the formation of hollow structure via Sn diffusion in SiO_2 structure, $Sn@SiO_2$ core-shell nanoparticles with various shell thickness (3.0 nm, 6.8 nm, and 29.0 nm) are synthesized (Figure 4.5b-d). The mean diameter of the original Sn nanoparticles used for the cores of $Sn@SiO_2$ is 16.9 nm, which is shown in Figure 4.5a. Also, the narrow size distributions of Sn nanoparticles and $Sn@SiO_2$ core-shell nanoparticles are exhibited in Figure 4.5e. To form the hollow SiO_2 structure, these three $Sn@SiO_2$ samples were transferred to a sealed aluminum pan and heated in a

differential scanning calorimeter (DSC) under a fixed heating condition (from 25°C to 300°C, ramping rate: 10°C/min, hold for 30 min at 300°C, naturally cooling down). It should be pointed out that different results are obtained from different SiO_2 shell thickness. After heating, Sn@SiO_2 with 3.0 mm SiO_2 shell was transformed into the yolk-shell structure as shown in Figure 4.5f and i, in which most of Sn cores remain inside SiO_2 shell but decrease in size. With a thicker shell (6.8 nm), the Sn@SiO_2 shown in Figure 4.5g and j contains much less Sn core after heat treatment, a big proportion of the SiO_2 structure become hollow, part of them had small Sn cores remained. As for the Sn@SiO_2 with the thickest SiO_2 shell (29.0 nm), no Sn cores are found after heating, only hollow SiO_2 structure remains. Based on these results, it seems that the as-prepared SiO_2 shell may have a capacity for containing certain amount of Sn species which come from the Sn cores by diffusion in a liquid state at an elevated temperature over the melting point of Sn. To collect more evidences for this hypothesis, Sn@SiO_2 core-shell nanoparticles with various core sizes but uniform SiO_2 shell with the thickness of 29.0 nm are designed and synthesized. After the same heating process, we find that the morphologies of the as-obtained products showing a continuous evolution from solid Sn@SiO_2 core-shell structure to yolk-shell structure and then hollow structure (Figure 4.6a). Figure 4.6b shows that when the shell thickness is fixed, the volume ratio between the remained Sn core and the original Sn core will increase with the diameter of the original Sn core. That is to say, Sn@SiO_2 core-shell nanoparticles with larger Sn cores may remain a greater proportion of Sn core after heating and diffusion. Combining with the results from Figure 4.5, we believe that the amorphous SiO_2 shell

that fabricated in our case provides space with a certain capacity for Sn species to stay after heating and diffusion. As we discussed in Figure 4.1f, SnO_2 is found after heating in vacuum at 300°C. This formation of SnO_2 may be contributed by the interactions between liquid Sn and the dangling bonds and hydroxyl on the surface of silica.[29-31] With the diffusion processes, the as-formed SnO_2 filled and blocked the channels for the diffusion of Sn, thus kept the rest Sn core staying undiffused in the half-core and yolk-shell Sn@SiO_2 cases. Figure 4.6c shows the distribution of the volume ratio between as-formed void (regarded as equal to the volume of diffused Sn) and SiO_2 shell, which is calculated from the measured data from more than 200 Sn@SiO_2 yolk-shell/hollow nanoparticles. These ratios are determined by the amount of Sn element distributed in a unit volume of SiO_2 shell. Based on above discussion, we believe that the SiO_2 shells of Sn@SiO_2 yolk-shell nanoparticles became "saturated" with Sn element after Sn diffusion by heating. The mean ratio is counted as 2.74, based on which, the maximum diameter of the original Sn core for the formation of hollow structure with the SiO_2 shell thickness of 29.0 nm is calculated as 17.9 nm.

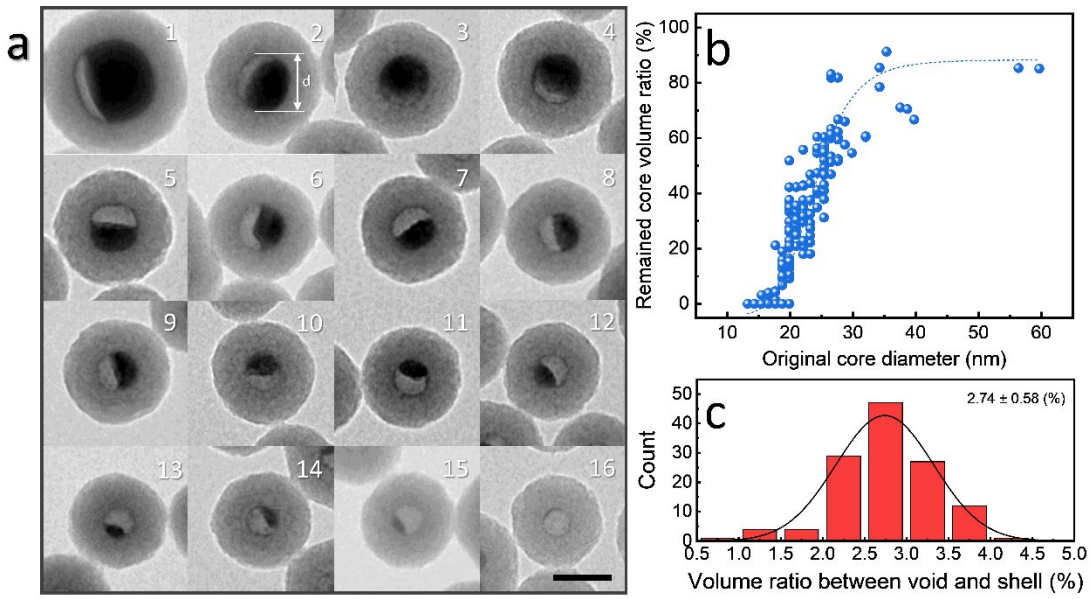

Figure 4.6 Formation of yolk-shell and hollow NPs from Sn@SiO_2 with the same thicknesses but different sizes of Sn core.

(a) After heating in a DSC (loaded in a sealed Al pan and heated from 25°C to 300°C at a ramping rate of 10°C/min), the Sn@SiO_2 core-shell nanoparticles are transformed into yolk-shell (1-15) and hollow nanoparticles (16), showing a gradual evolution from core-shell to yolk-shell and finally hollow nanoparticles. Sn@SiO_2 core-shell nanoparticles with the same shell thickness (29.0 nm) but various core diameters (shown in a-2 as "d") (20~59 nm) are used as starting materials. Scale bar is 40 nm. (b) Volume ratio between remained Sn core and the original Sn core obtained by measuring more than 200 particles with various diameters from 13.3 to 59.7 nm. The increasing ratio of remained Sn core with bigger original core diameter indicate that Sn@SiO_2 NPs with bigger Sn cores will keep more Sn remained after heating, showing controllable Sn diffusion based on size difference (c) Histogram of volume ratios between as-formed void and shell which is close to Gaussian distribution. The mean value of this ratio is 2.74 ± 0.58, indicating a possible containing capacity of SiO_2 structure for Sn.

High-angle annular dark-field scanning transmission electron microscopy (HAADF-STEM), energy dispersive spectroscopy (EDS) elemental mapping and X-

ray photoelectron spectroscopy (XPS) are used for investigating the element distribution of as-formed hollow SiO_2 structure. The HAADF-STEM image in Figure 4.7a shows a high Z contrast of inner surface in the hollow SiO_2 structures. Meanwhile, many bright spots in the shell area are found, indicating the existence of embedded Sn element which has a higher Z contrast (Figure 4.7a and Figure S4.7d). Elemental mapping in Figure 4.7b shows that Sn element is uniformly distributed inside the SiO_2 hollow structure. During the ex-situ observation, similarly, the deformation of SiO_2 is found: the shrinkage occurred, and the surface became rough after electron beam focusing (Figure S4.7a, b). Figures S4.7e and the inset image show HRTEM image and its corresponding fast Fourier transform (FFT) pattern, respectively, the interplanar distance is calculated as 0.343 nm, corresponding to the (110) crystal planes of tetragonal SnO_2 (JCPDS No. 41-1445) which is in good agreement with the SAED results shown in Figure 4.1f and Figure S4.4. To check the Sn distribution on surface and near surface area (3−10 nm), XPS wide scan was performed on Sn@SiO_2 core-shell nanoparticles before and after heat treatment in DSC (Figure 4.7c). Before heat treatment, no signal from Sn was detected, while strong signal from Sn appeared when testing the Sn@SiO_2 core-shell nanoparticles after heat treatment, showing a strong evidence for outward diffusion of Sn. In addition, the XPS narrow scan (Figure S4.8) shows that most of Sn in hollow structure existed as SnO_2, which is in a good agreement with the previous discussion.

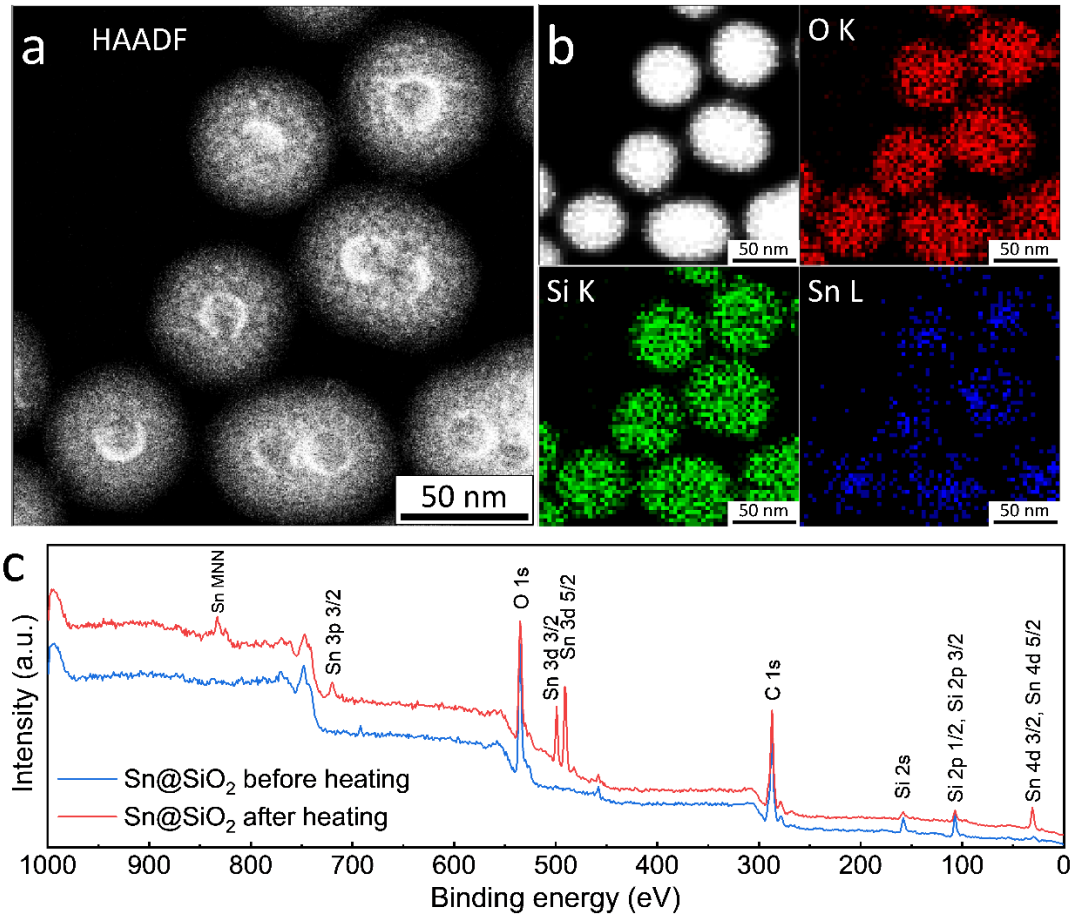

Figure 4.7. Element distribution of as obtained hollow NPs.

(a) HAADF-STEM image and (b) EDS element mapping images of as-formed hollow structure in ex-situ TEM observation, showing the distribution of Sn, Si and O, respectively. (c) The XPS wide scan of Sn@SiO_2 core-shell nanoparticles before and after heating.

It must also be mentioned that the In-Sn@SiO_2 nanoparticles were prepared by a similar method (Figure S4.9c). In-Sn alloy has an even lower melting temperature. We applied the same condition of the heating process for Sn@SiO_2 on In-Sn@SiO_2. The hollow structure also appeared after being heated above the melting temperature

(Figure S4.9d), indicating that the diffusion of both In and Sn occurred inside SiO_2 structure.

4.4. Conclusions

In summary, a novel design of controllable nanostructure of $Sn@SiO_2$ from core-shell to yolk-shell and hollow has been achieved through a liquid metal diffusion process. The transformation of $Sn@SiO_2$ core-shell nanoparticles into hollow SiO_2 nanostructure by diffusion of liquid Sn cores inside $Sn@SiO_2$ was real-time observed via in-situ TEM. The diffusion of liquid state Sn acts as the role for removing the cores thus creating the cavity for hollow nanostructure. Importantly, based on our findings, we demonstrated the control over the morphologies of hollow/yolk-shell $Sn@SiO_2$ nanostructures by adjusting the volume ratio between core and shell of starting $Sn@SiO_2$ core-shell nanoparticle precursors. Furthermore, our findings here provide valuable knowledge of diffusion of liquid state metal inside SiO_2 structure, as well as a novel tool in designing complicated hollow nanostructures in future studies.

References

1. Prieto, G.; Tüysüz, H.; Duyckaerts, N.; Knossalla, J.; Wang, G.-H.; Schüth, F. Hollow Nano- and Microstructures as Catalysts. *Chem. Rev.* **2016**, 116 (22), 14056-14119.

2. Wang, J.; Cui, Y.; Wang, D. Design of Hollow Nanostructures for Energy Storage, Conversion and Production. *Adv. Mater.* **2018**, 1801993.

3. Lee, J.-H. Gas sensors using hierarchical and hollow oxide nanostructures: Overview. *Sensors and Actuators B: Chemical* **2009**, 140 (1), 319-336.

4. Zhang, Y.; Hsu, B. Y. W.; Ren, C.; Li, X.; Wang, J. Silica-based nanocapsules: synthesis, structure control and biomedical applications. *Chem. Soc. Rev.* **2015**, 44 (1), 315-335.

5. Wang, W.; Dahl, M.; Yin, Y. Hollow Nanocrystals through the Nanoscale Kirkendall Effect. *Chem. Mater.* **2012**, 25 (8), 1179-1189.

6. Jin Fan, H.; Knez, M.; Scholz, R.; Nielsch, K.; Pippel, E.; Hesse, D.; Zacharias, M.; Gosele, U. Monocrystalline spinel nanotube fabrication based on the Kirkendall effect. *Nat. Mater.* **2006**, 5 (8), 627-31.

7. Fan, H. J.; Gosele, U.; Zacharias, M. Formation of nanotubes and hollow nanoparticles based on Kirkendall and diffusion processes: a review. *Small* **2007**, 3 (10), 1660-71.

8. Wang, X.; Feng, J.; Bai, Y.; Zhang, Q.; Yin, Y. Synthesis, Properties, and Applications of Hollow Micro-/Nanostructures. *Chem. Rev.* **2016**, 116 (18), 10983-11060.

9. Lu, Q.; Gao, F. Synthesis and property studies of hollow nanostructures. *CrystEngComm* **2016**, 18 (39), 7399-7409.

10. Zhang, Q.; Wang, W.; Goebl, J.; Yin, Y. Self-templated synthesis of hollow nanostructures. *Nano Today* **2009**, 4 (6), 494-507.

11. Fan, H. J.; Gösele, U.; Zacharias, M. Formation of Nanotubes and Hollow Nanoparticles Based on Kirkendall and Diffusion Processes: A Review. *Small* **2007**, 3 (10), 1660-1671.

12. Lou, X. W.; Archer, L. A.; Yang, Z. Hollow Micro-/Nanostructures: Synthesis and Applications. *Adv. Mater.* **2008**, 20 (21), 3987-4019.

13. Sutter, E. A.; Sutter, P. W. In situ liquid cell electron microscopy of Ag–Au galvanic replacement reactions. *Nanoscale* **2017**, 9 (3), 1271-1278.

14. Sutter, E.; Jungjohann, K.; Bliznakov, S.; Courty, A.; Maisonhaute, E.; Tenney, S.; Sutter, P. In situ liquid-cell electron microscopy of silver–palladium galvanic replacement reactions on silver nanoparticles. *Nat. Commun.* **2014**, 5, 4946.

15. Niu, K. Y.; Park, J.; Zheng, H.; Alivisatos, A. P. Revealing bismuth oxide hollow nanoparticle formation by the Kirkendall effect. *Nano Lett.* **2013**, 13 (11), 5715-9.

16. Chee, S. W.; Tan, S. F.; Baraissov, Z.; Bosman, M.; Mirsaidov, U. Direct observation of the nanoscale Kirkendall effect during galvanic replacement reactions. *Nat. Commun*. **2017**, 8 (1), 1224.

17. Yang, Y.; Scholz, R.; Berger, A.; Kim, D. S.; Knez, M.; Hesse, D.; Gösele, U.; Zacharias, M. Transmission Electron Microscopy in situ Fabrication of ZnO/Al2O3 Composite Nanotubes by Electron-Beam-Irradiation-Induced Local Etching of ZnO/Al2O3 Core/Shell Nanowires. *Small* **2008**, 4 (12), 2112-2117.

18. Zhu, J.; Sun, T.; Hng, H. H.; Ma, J.; Boey, F. Y. C.; Lou, X.; Zhang, H.; Xue, C.; Chen, H.; Yan, Q. Fabrication of Core−Shell Structure of M@C (M=Se, Au, Ag2Se) and Transformation to Yolk−Shell Structure by Electron Beam Irradiation or Vacuum Annealing. *Chem. Mater.* **2009**, 21 (16), 3848-3852.

19. Kravchyk, K.; Protesescu, L.; Bodnarchuk, M. I.; Krumeich, F.; Yarema, M.; Walter, M.; Guntlin, C.; Kovalenko, M. V. Monodisperse and Inorganically Capped Sn and Sn/SnO2 Nanocrystals for High-Performance Li-Ion Battery Anodes. *J. Am. Chem. Soc.* **2013**, 135 (11), 4199-4202.

20. Lai, S. L.; Guo, J. Y.; Petrova, V.; Ramanath, G.; Allen, L. H. Size-Dependent Melting Properties of Small Tin Particles: Nanocalorimetric Measurements. *Phys. Rev. Lett.* **1996**, 77 (1), 99-102.

21. Zheng, K.; Wang, C.; Cheng, Y.-Q.; Yue, Y.; Han, X.; Zhang, Z.; Shan, Z.; Mao, S. X.; Ye, M.; Yin, Y.; Ma, E. Electron-beam-assisted superplastic shaping of nanoscale amorphous silica. *Nat. Commun*. **2010**, 1, 24.

22. Storm, A. J.; Chen, J. H.; Ling, X. S.; Zandbergen, H. W.; Dekker, C. Fabrication of solid-state nanopores with single-nanometre precision. *Nat. Mater.* **2003**, 2, 537.

23. Storm, A. J.; Chen, J. H.; Ling, X. S.; Zandbergen, H. W.; Dekker, C. Electron-beam-induced deformations of SiO2 nanostructures. *J. Appl. Phys.* **2005**, 98 (1), 014307.

24. Brückner, R. Properties and structure of vitreous silica. *I. J. Non-Cryst. Solids* **1970**, 5 (2), 123-175.

25. Yang, Z.; Walls, M.; Lisiecki, I.; Pileni, M.-P. Unusual Effect of an Electron Beam on the Formation of Core/Shell (Co/CoO) Nanoparticles Differing by Their Crystalline Structures. *Chem. Mater*. **2013**, 25 (11), 2372-2377.

26. Huang, C.-W.; Hsin, C.-L.; Wang, C.-W.; Chu, F.-H.; Kao, C.-Y.; Chen, J.-Y.; Huang, Y.-T.; Lu, K.-C.; Wu, W.-W.; Chen, L.-J. Direct observation of melting behaviors at the nanoscale under electron beam and heat to form hollow nanostructures. *Nanoscale* **2012**, 4 (15), 4702-4706.

27. Voorhees, P. W. The theory of Ostwald ripening. *J. Stat. Phys*. **1985**, 38 (1), 231-252.

28. Finsy, R. On the Critical Radius in Ostwald Ripening. *Langmuir* **2004**, 20 (7), 2975-2976.

29. Zhuravlev, L. T. The surface chemistry of amorphous silica. Zhuravlev model. *Colloids and Surfaces A: Physicochemical and Engineering Aspects* **2000**, 173 (1), 1-38.

30. Iler, R. K. The Chemistry of Silica: Solubility, Polymerization, *Colloid and Surface Properties and Biochemistry of Silica.* **1979**.

31. Zhu, S.; Nguyen, M. T.; Fumoto, K.; Kanie, K.; Muramatsu, A.; Yonezawa, T. Sn Nanoparticles Confined in Porous Silica Spheres for Enhanced Thermal Cyclic Stability. *ACS Appl. Nano Mater.* **2018**, 1 (8), 4073-4082.

Chapter 5.

Conclusion and prospective

A nanostructure in which phase-change Sn NPs were confined inside p-SiO_2 spheres was synthesized through a facile method utilizing common starting chemicals. The p-SiO_2 spheres effectively stabilized the embedded Sn NPs during cyclic melting–cooling. The melting depression phenomenon of the Sn NPs expands the application window of phase-change thermal energy storage using low-melting-temperature metals. The formation of voids inside Sn NPs@p-SiO_2 was investigated for the first time. The transformation of the Sn precursor occurred and included the formation and decomposition of the amorphous Sn precursor, formation and reduction of crystal Sn oxides, and interactions between Sn NPs and SiO_2 during annealing in a 3% H_2/N_2 atmosphere. It is believed that the transformation of the Sn precursor during annealing accompanied by the modification of the formed Sn NPs led to the formation of big voids inside p-SiO_2 spheres, which gives inspiration for new strategies for the synthesis of hollow SiO_2 spheres and yolk–shell SiO_2 structures.

Alumina-encapsulated Sn particles (Sn@Al_2O_3) were successfully prepared and used as PCMs. The fabrication process consisted of a surfactant-free solvothermal synthesis of SnO_2spheres, boehmite treatment on SnO_2 spheres, calcination in the air, and the final hydrogen reduction to transform SnO_2 to metallic Sn. All the steps of fabrication are facile and low-cost which can be simply applied to the mass production. The as-obtained Sn@Al_2O_3 particles with a high PCM content (92.37 wt %) showed a

stable thermal behavior and morphology during 100 melt–freeze cycles in the air atmosphere. The $Sn@Al_2O_3$ shows a core–shell structure with small Sn nanoparticles dispersed in the shell. The formation of $Sn@Al_2O_3$ structure is a result of boehmite treatment on SnO_2 spheres for the involvement of aluminum. The penetration of boehmite sol (AlOOH) into the SnO_2 spheres contributes to the formation of the thick alumina shell, which plays a key role in the thermal storage stability. This result also provided the possibility for a facile method for designing new metal nanoparticles with a particle-distributed nanostructure. These results also demonstrate the great potential of $Sn@Al_2O_3$ particles in the applications as a thermal energy storage material in high-temperature conditions which are not suitable for organic PCMs.

A novel design of controllable nanostructure of $Sn@SiO_2$ from core-shell to yolk-shell and hollow has been achieved through a liquid metal diffusion process. The transformation of $Sn@SiO_2$ core-shell nanoparticles into hollow SiO_2 nanostructure by diffusion of liquid Sn cores inside $Sn@SiO_2$ was real-time observed via in-situ TEM. The diffusion of liquid state Sn acts as the role for removing the cores thus creating the cavity for hollow nanostructure. Importantly, based on these findings, the control over the morphologies of hollow/yolk-shell $Sn@SiO_2$ nanostructures was demonstrated by adjusting the volume ratio between core and shell of starting $Sn@SiO_2$ core-shell nanoparticle precursors. Furthermore, these findings provide valuable knowledge of diffusion of liquid state metal inside SiO_2 structure, as well as a novel tool in designing complicated hollow nanostructures in future studies.

Appendix

A. Supporting Information for Chapter 2

Table S1 Crystalline size of SnO_2 in p-SiO_2 with different annealing temperatures

Annealing temperature under 3% H_2/N_2 flow (°C)	**Crystal size of SnO_2 (nm)**
330	2.68
360	6.02
400	7.79

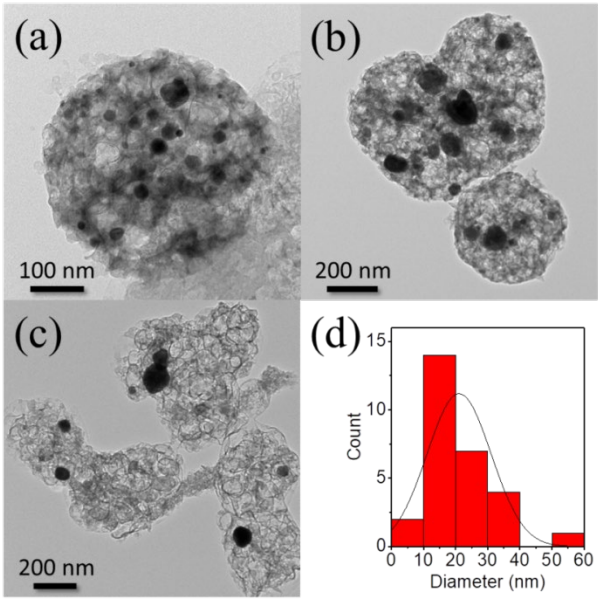

Figure S2.1. (a-c) The TEM images of NaOH etched Sn NPs@p-SiO_2 and (d) the size histogram of obtained Sn NPs

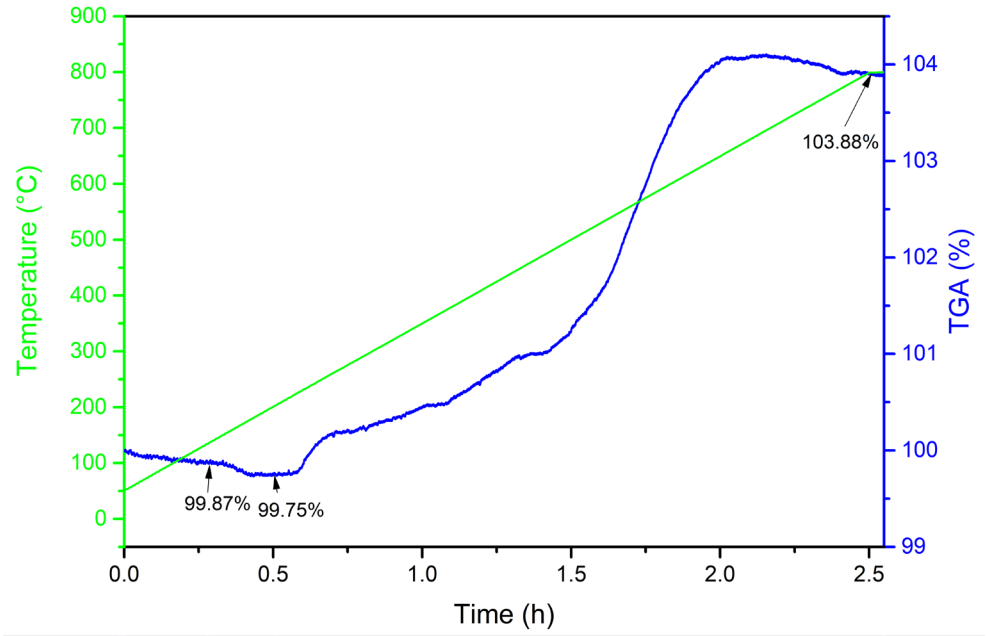

Figure S2.2. TGA results of Sn@p-SiO_2 in air

Estimation of the amount of Sn in Sn@p-SiO_2

We assumed our product Sn@p-SiO_2 is consisted with a wt% Sn, b wt% SnO_2, c wt% H_2O and d wt% p-SiO_2. So, obviously,

$$a + b + c + d = 100 \quad \text{(S1)}$$

From the TGA results of Sn@p-SiO_2 in air, we observed a mass increase from 99.87 wt% to 103.88 wt% which includes mass gain from oxidation of metallic tin to SnO_2 and loss from removal of a trace amount H_2O:

$$a \times \frac{32}{118.7} - c = 103.88 - 99.87 \quad \text{(S2)}$$

Weight loss below 200°C in figure S2 came from the removal of H_2O:

$$c = 0.12 \quad \text{(S3)}$$

From XPS results showed in figure 4, we assume the molar ratio between Sn : SnO_2 is 54.88 : 45.12. So, their mass ratio should be 0.958: 1

$$a - 0.958b = 0 \quad \text{(S4)}$$

From equations S1-S4, the mass percentage of each component in the product is

Sn: SnO_2: H_2O: p-SiO_2 = 15.32: 15.99: 0.12: 68.57

Thus, the molar ratio between Sn and Si is 17.1%: 82.9%.

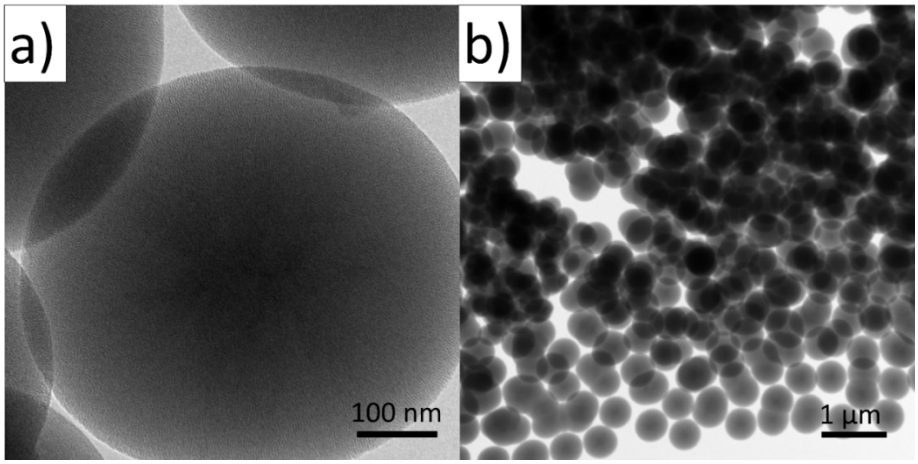

Figure S2.3. TEM images of calcinated porous silica spheres with different magnifications.

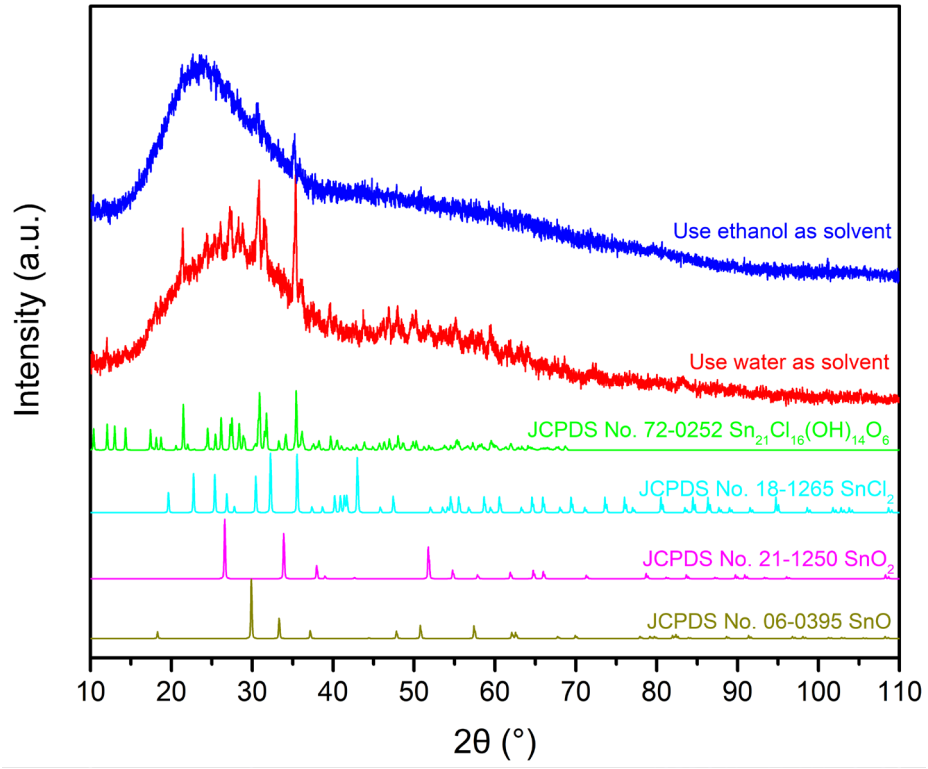

Figure S2.4. XRD results of $SnCl_2$@p-SiO_2 prepared using water (red) and ethanol (blue) as the solvents for impregnation of Sn precursor.

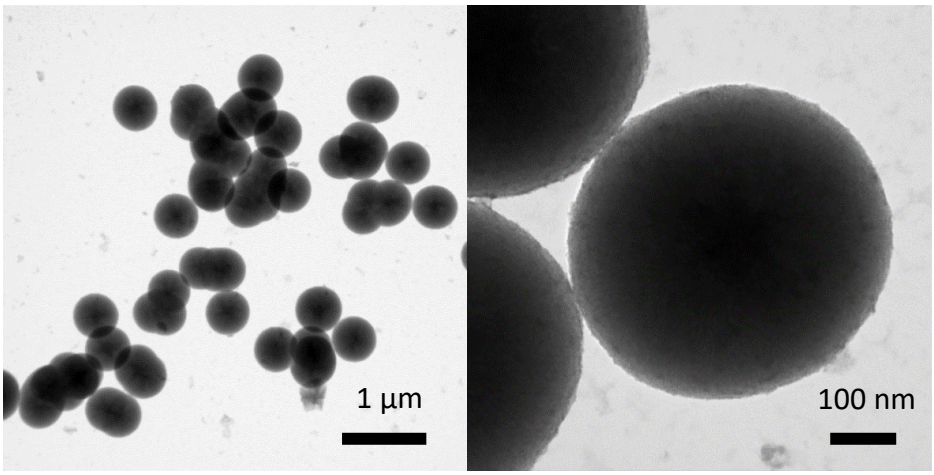

Figure S2.5. TEM images of $SnCl_2$@p-SiO_2 using water as solvent for impregnation with different magnifications.

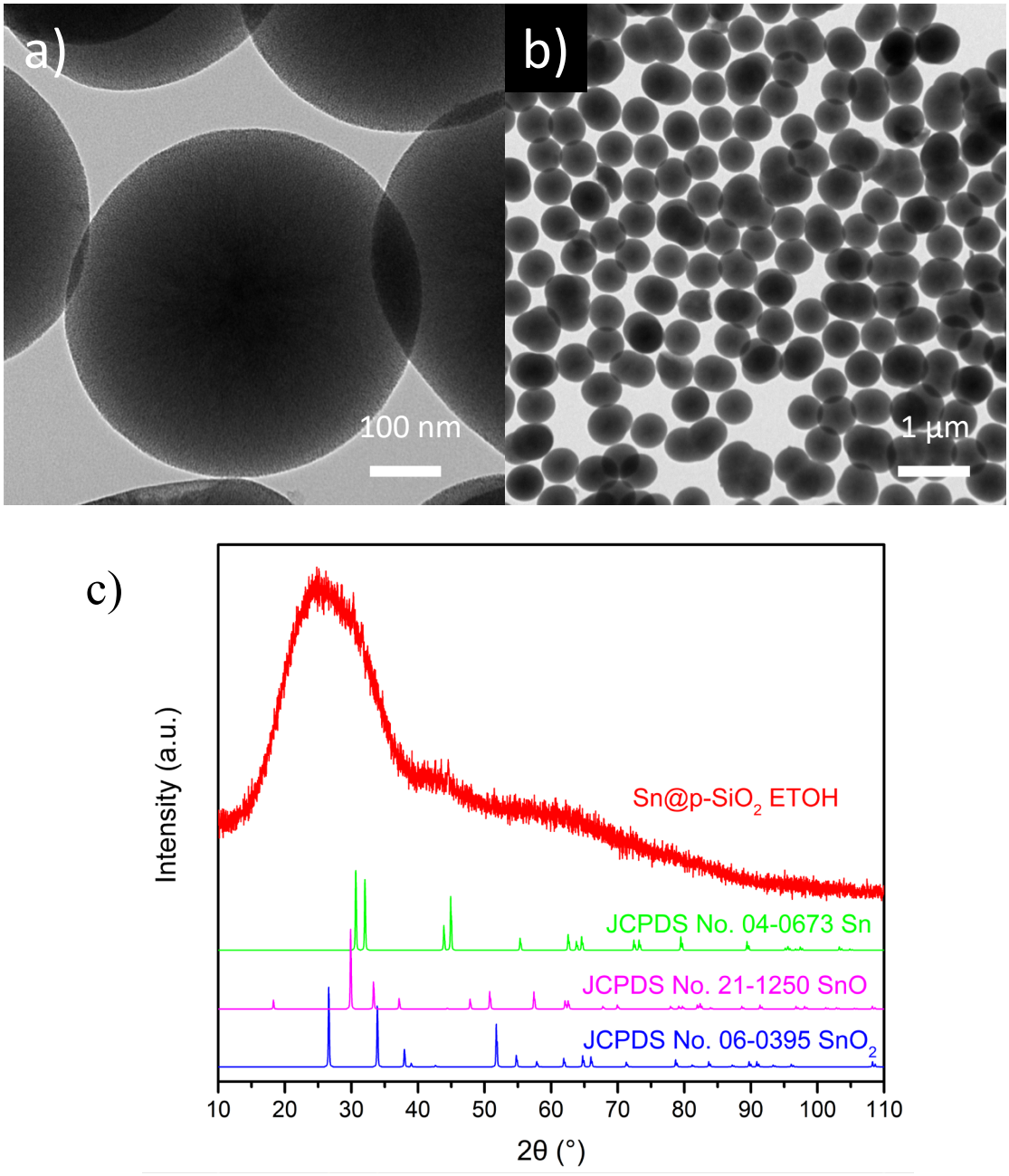

Figure S2.6. (a,b) TEM images and (c) XRD pattern of Sn@p-SiO_2 using ethanol as solvent for impregnation of Sn precursor.

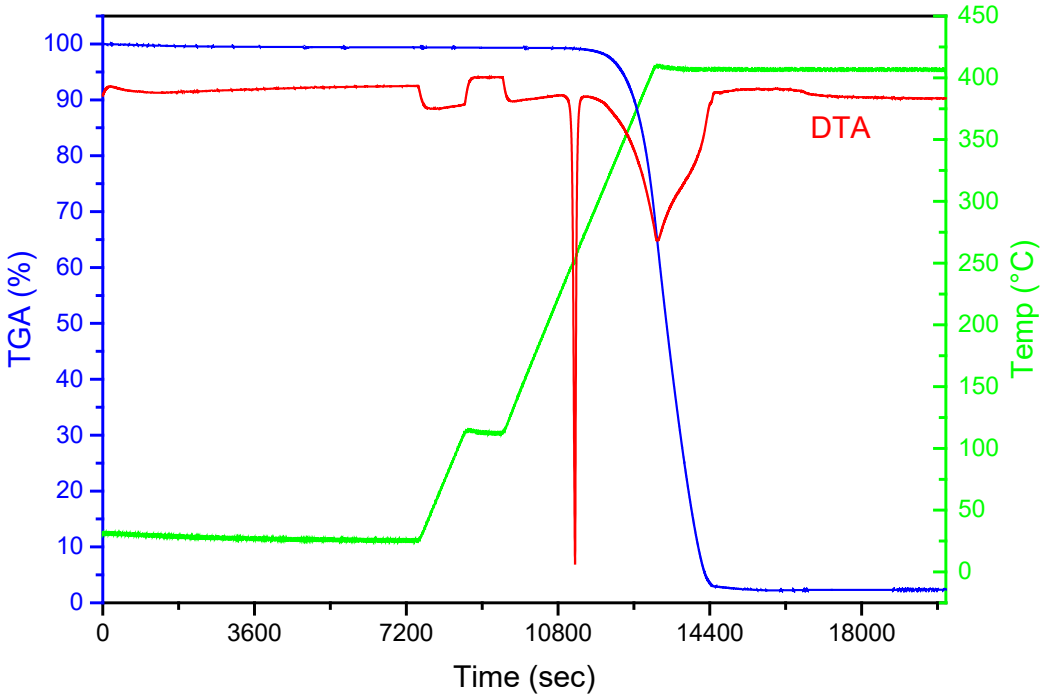

Figure S2.7. TG-DTA results of anhydrous $SnCl_2$ powder in N_2.

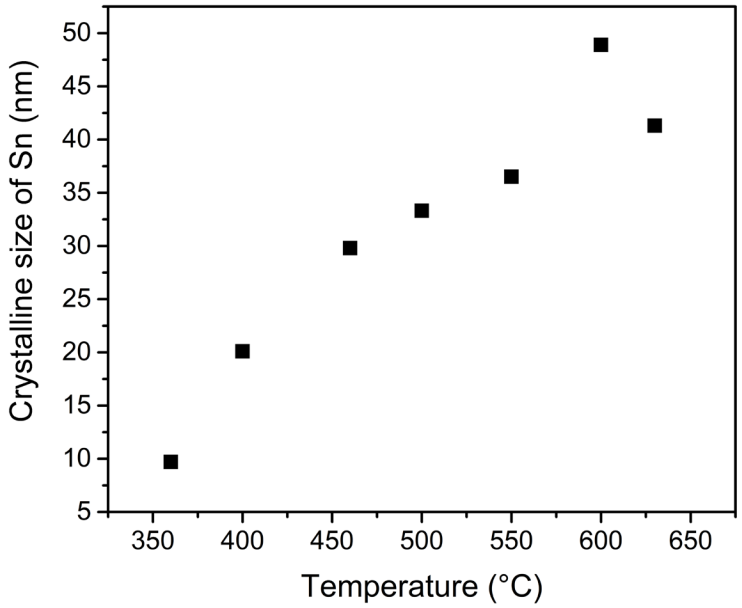

Figure S2.8. The relationship between the reduction temperature and the size of Sn nanoparticles obtained. The size increases with the reduction temperature.

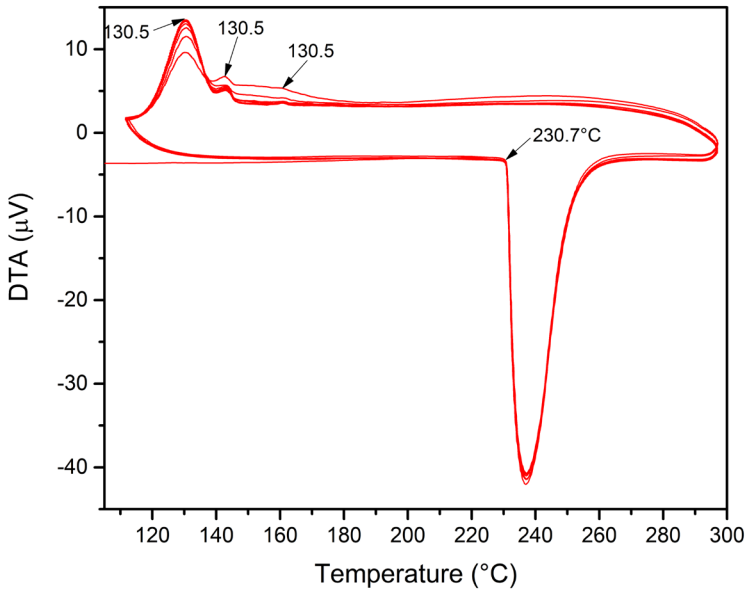

Figure S2.9. DTA measurement results of bulk tin for 10 melt-freeze cycles

Model for calculating melting temperature:

The model for calculating melting temperature is proposed by S. L. Lai *et al*.[S1] This model assumes that a solid particle is embedded in a thin liquid overlayer and the melting temperature is taken to be the temperature of equilibrium between the solid sphere core and the liquid overlayer of a given critical thickness t_0.

The melting point T_m of Sn particles with radius r is expressed as

$$T_m = 232 - 782\left[\frac{\sigma_s}{15.8(r-t_0)} - \frac{1}{r}\right] \quad \text{(S5)}$$

where T_m is melting temperature of nanoparticle [°C] and r is particle radius [Å] and t_0 is the critical thickness of the liquid layer at T_m which is set to be 18 Å. The interfacial surface tension between the solid and liquid, σ_s, can be determined experimentally in terms of Eq. S5. The slope $\frac{dT_m}{d\frac{1}{r}}$ at large r is related to σ_s. σ_s is determined to be 48 ± 8 mN/m.

Reference

S1. Lai, S. L.; Guo, J. Y.; Petrova, V.; Ramanath, G.; Allen, L. H., Size-Dependent Melting Properties of Small Tin Particles: Nanocalorimetric Measurements. *Phys. Rev. Lett.* **1996,** *77*, 99-102.

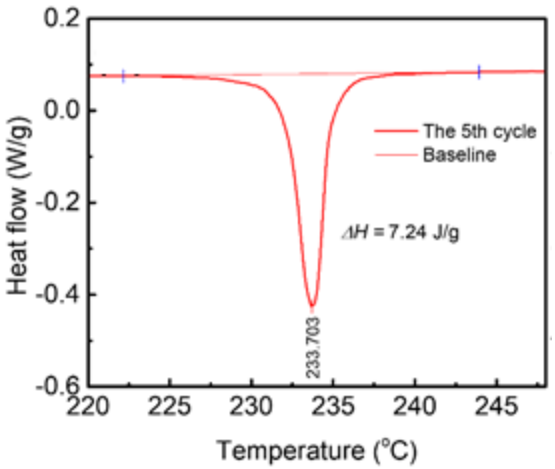

Figure S2.10. Example of the DSC curve for the 5th cycle in the 220 – 245°C range during 100 melt-freeze cycles for calculating the enthalpy of melting.

B. Supporting Information for Chapter 3

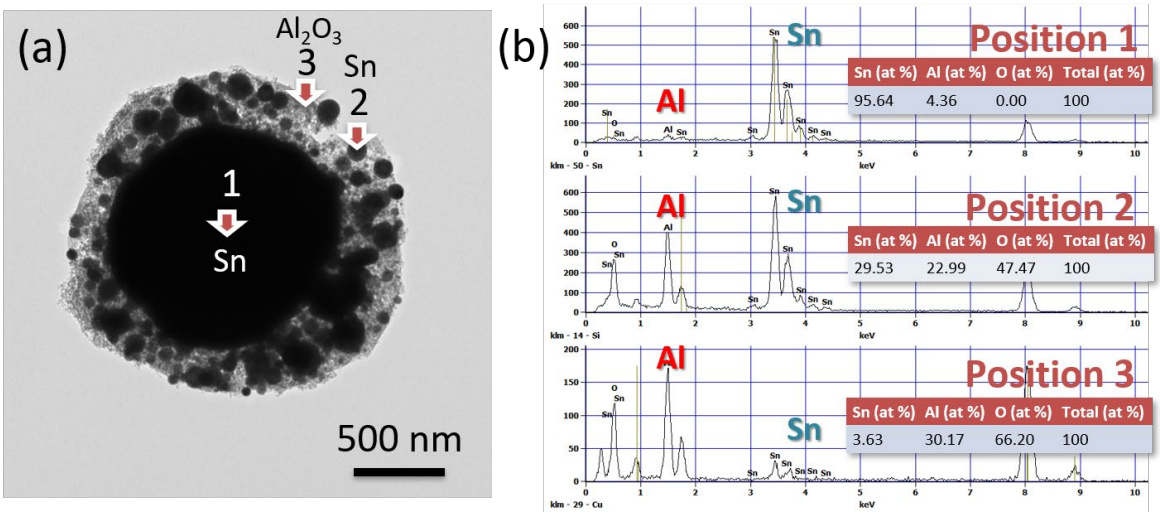

Figure S3.1. (a) TEM image of as-synthesized Sn@Al_2O_3. (b) EDS results from different positions marked in (a).

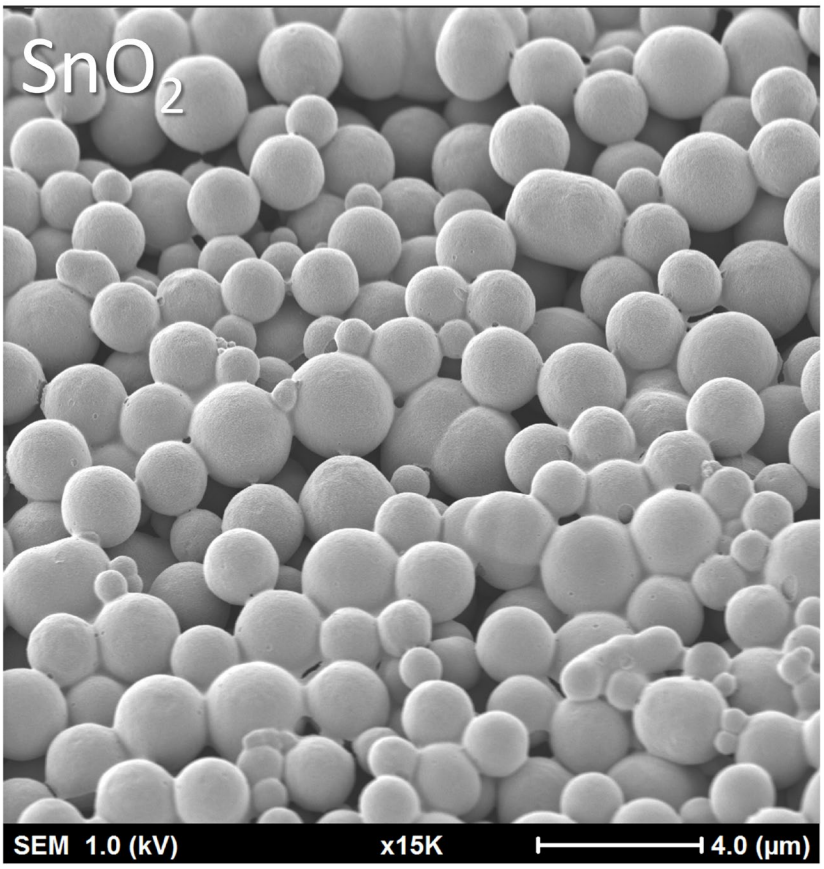

Figure S3.2. SEM image of calcined SnO_2 spheres.

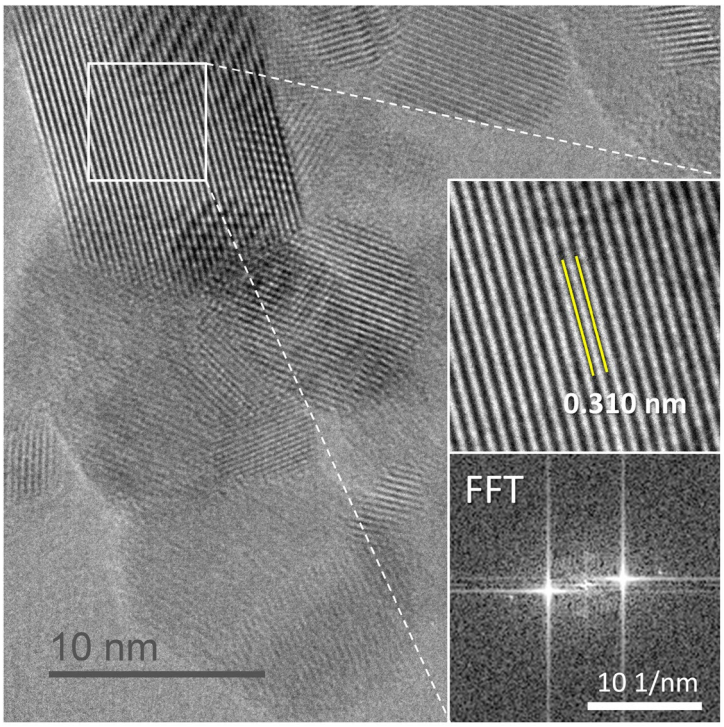

Figure S3.3. HRTEM image of SnO_2@Al_2O_3.

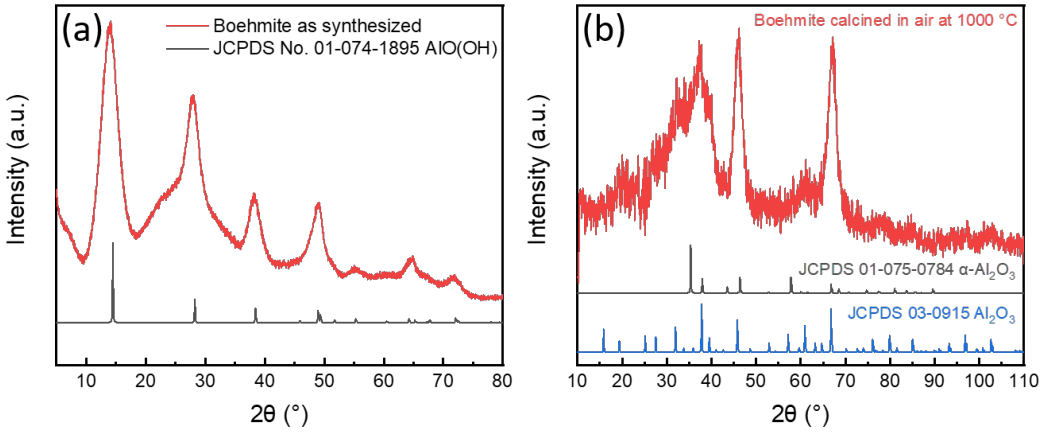

Figure S3.4. XRD patterns of boehmite (a) as synthesized and (b) after calcination at 1000°C in the air.

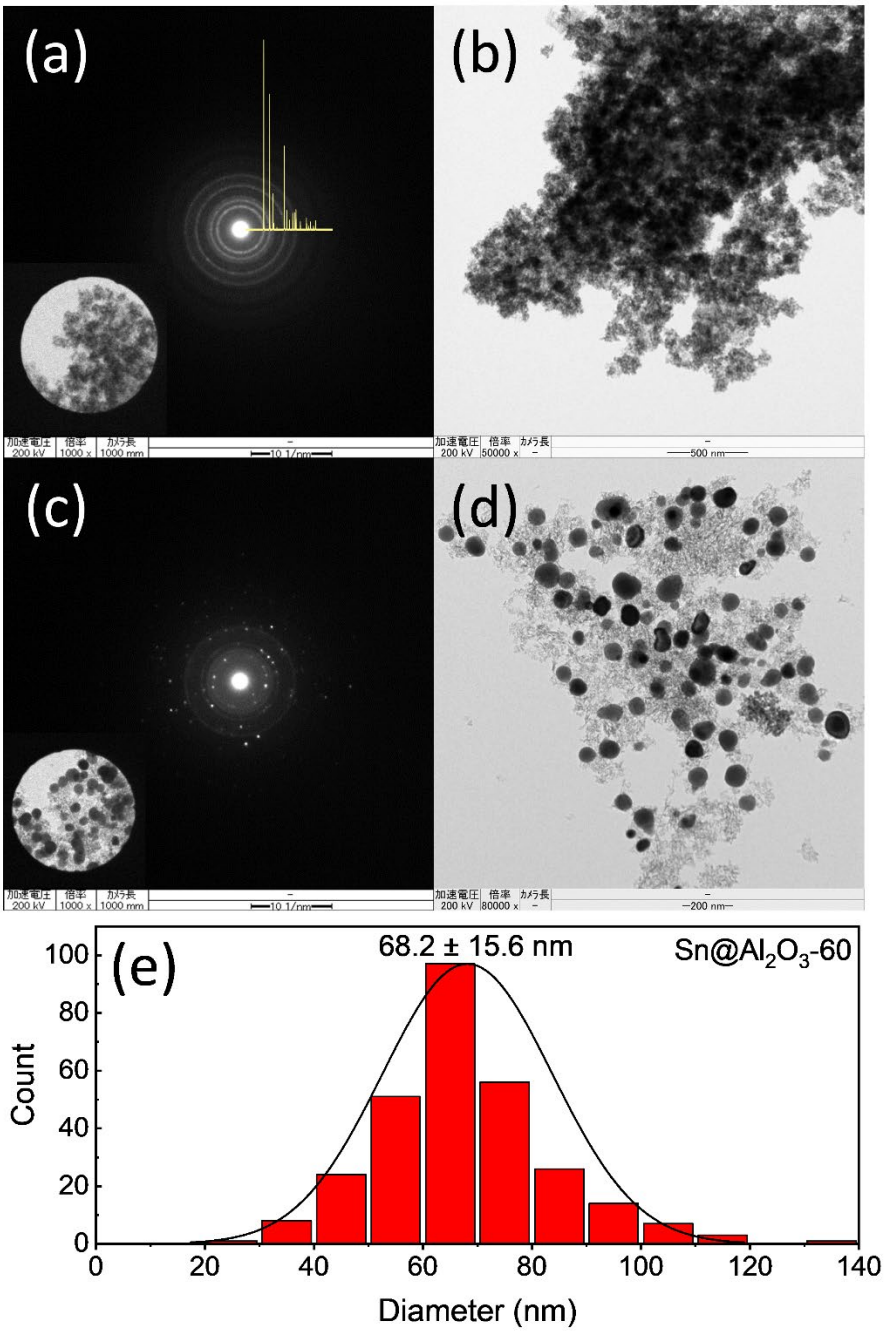

Figure S3.5. TEM images and SEAD patterns of as-synthesized (a, b) SnO_2@Al_2O_3-60 and (c, d) Sn@Al_2O_3-60 using SnO_2 spheres (~60 nm) as Sn precursor. (e) Size histogram of Sn NPs in Sn@Al_2O_3-60.

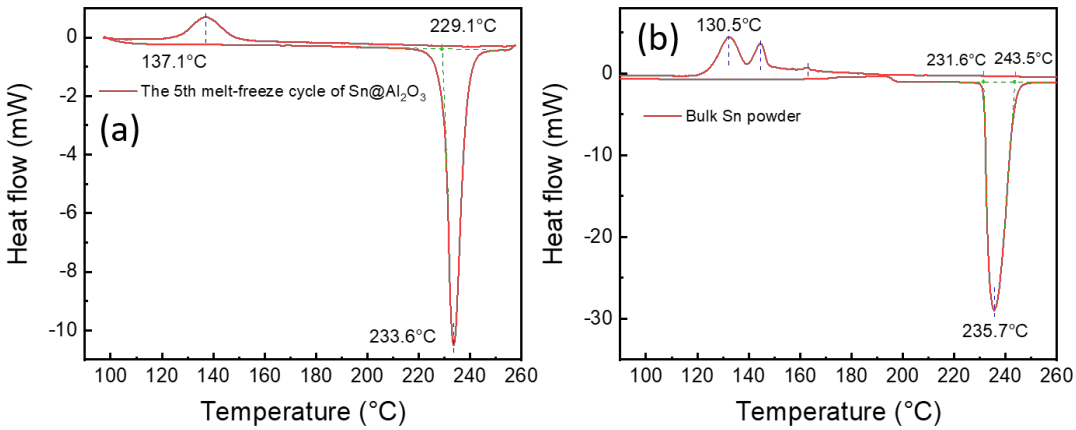

Figure S3.6. Typical melt-freeze DSC curves of (a) Sn@Al_2O_3-1600 at the 5th cycle and (b) commercial Sn powder.

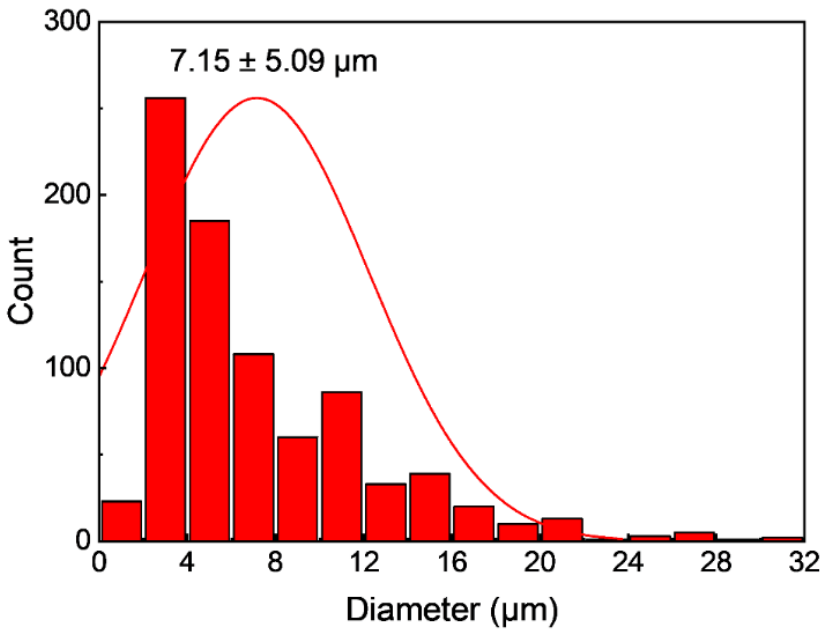

Figure S3.7. Size histogram of commercial Sn powder.

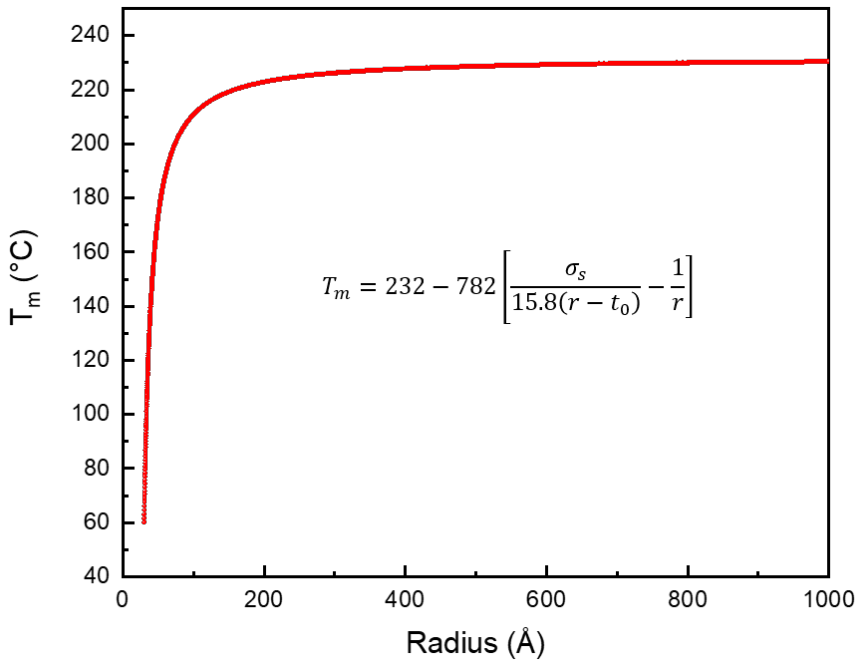

Figure S3.8. Size-dependent melting of Sn nanoparticles.

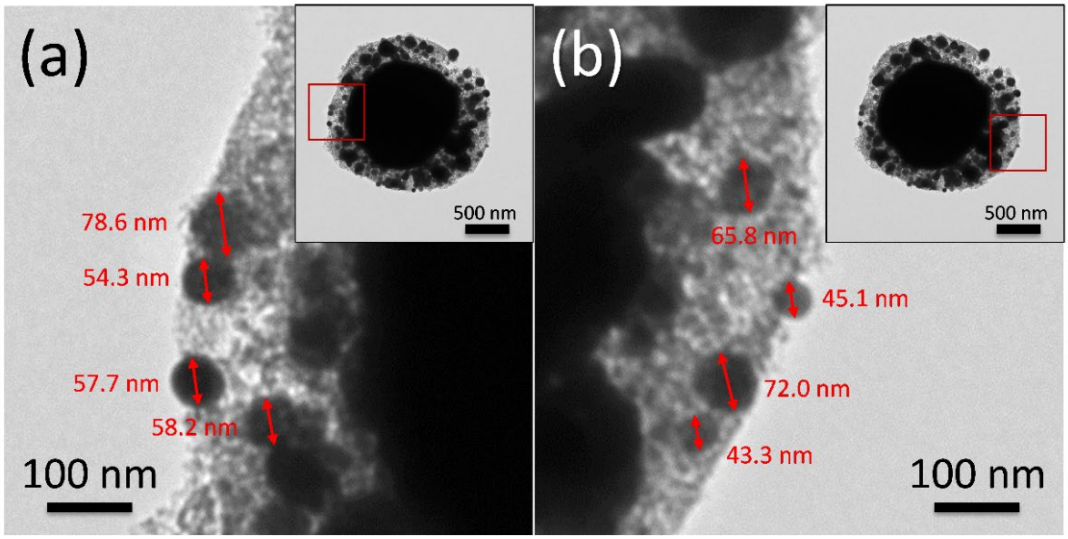

Figure S3.9. TEM images of small Sn NPs of 40-80 nm located in the Al_2O_3 shell of Sn@Al_2O_3-1600 as marked by red squares in the insets.

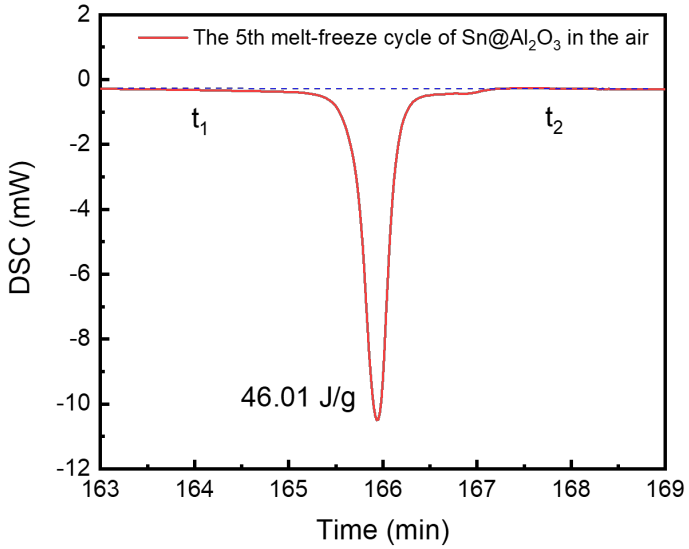

Figure S3.10. The DSC curve of the 5th melt-freeze cycle of Sn@Al_2O_3-1600 in the air with time as x-axis.

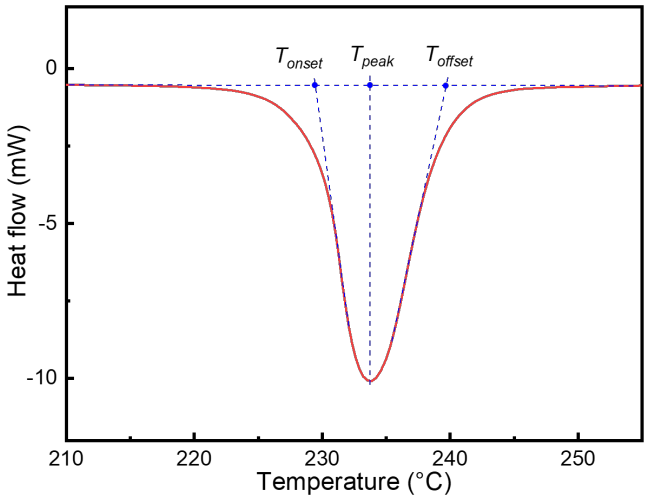

Figure S3.11. Definition of onset temperature (T_{onset}), peak temperature (T_{peak}) and offset temperature (T_{offset}).

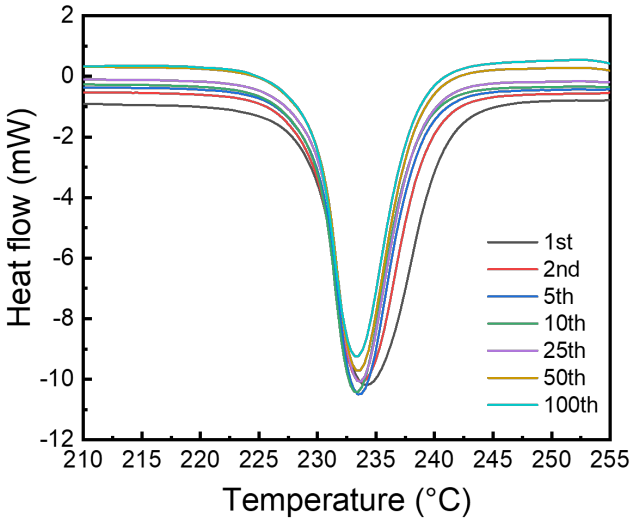

Figure S3.12. Typical melting DSC curves of Sn@Al_2O_3-1600 at the 1st, 2nd, 5th, 10th, 25th, 50th and 100th melt-freeze cycles.

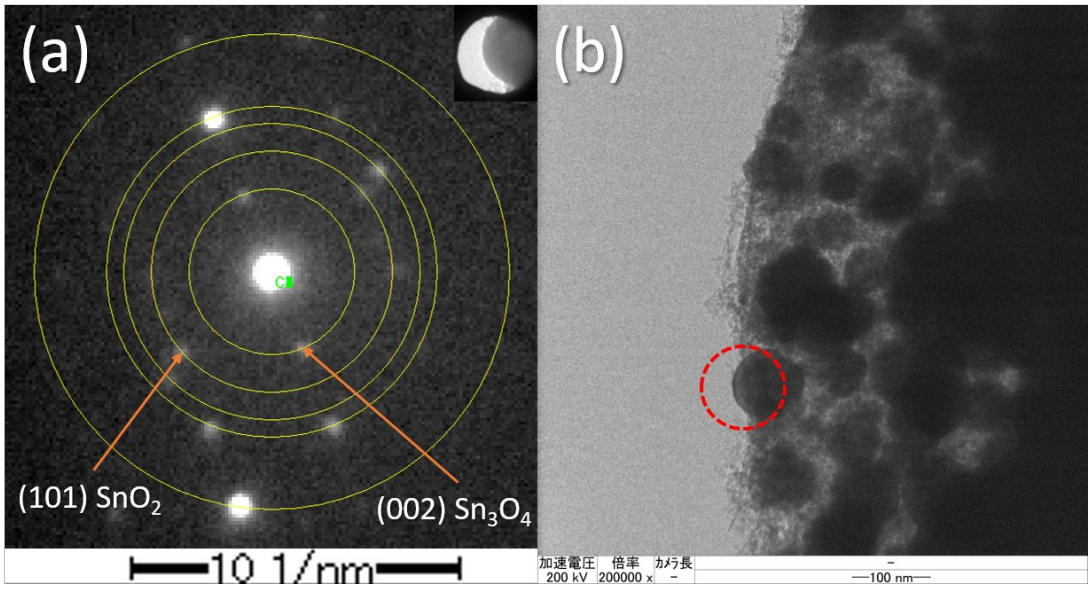

Figure S3.13. The SAED pattern (a) of a Sn nanoparticle (inset) located at the surface of Sn@Al_2O_3-1600 as shown in the TEM image (b) after 100 melt-freeze cycles in the air.

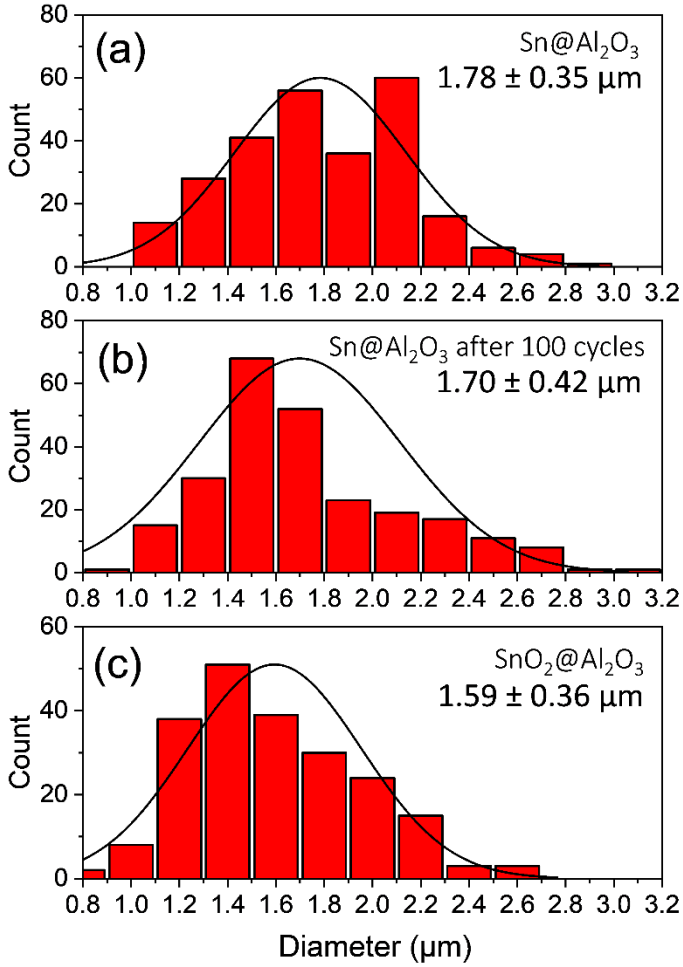

Figure S3.14. The size distributions of $Sn@Al_2O_3$-1600 ((a) before and (b) after DSC melt-freeze cycles) and (c) $SnO_2@Al_2O_3$-1600.

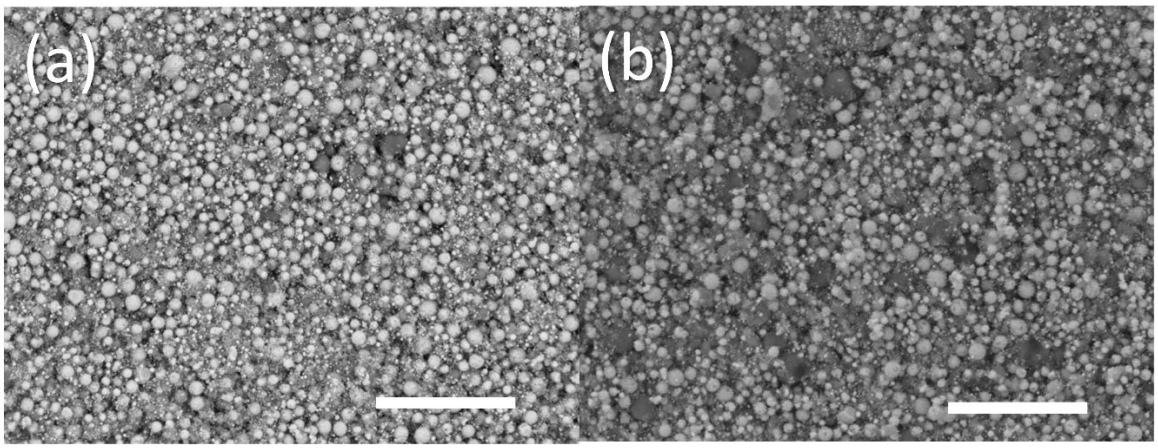

Figure S3.15. SEM images of Sn@Al_2O_3-1600 with a low magnification (a) before and (b) after melt-freeze cycle test. Scale bar: 20 µm.

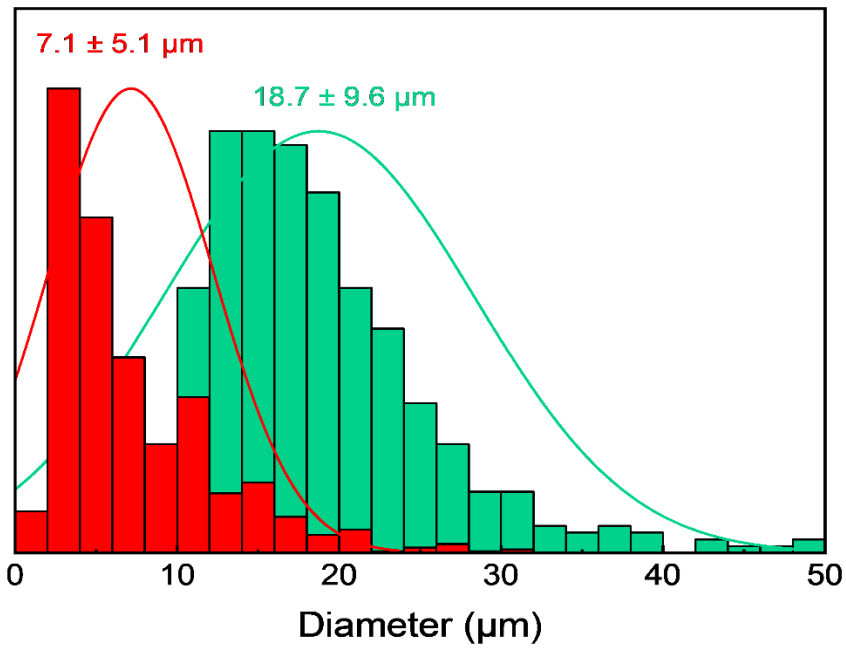

Figure S3.16. The size distributions of commercial Sn powder before (red) and after (green) DSC melt-freeze cycles.

C. Supporting Information for Chapter 4

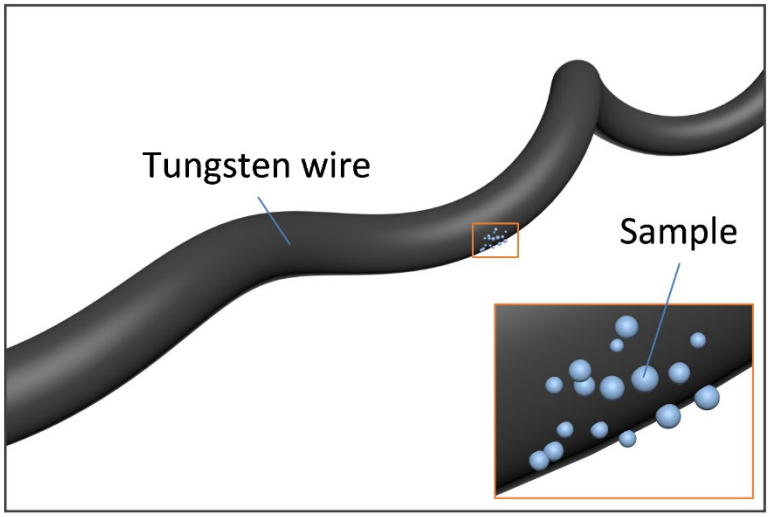

Figure S4.1. Schematic of sample loading: Sn@SiO_2 core-shell nanoparticles are loaded on a tungsten wire inside a heating sample holder.

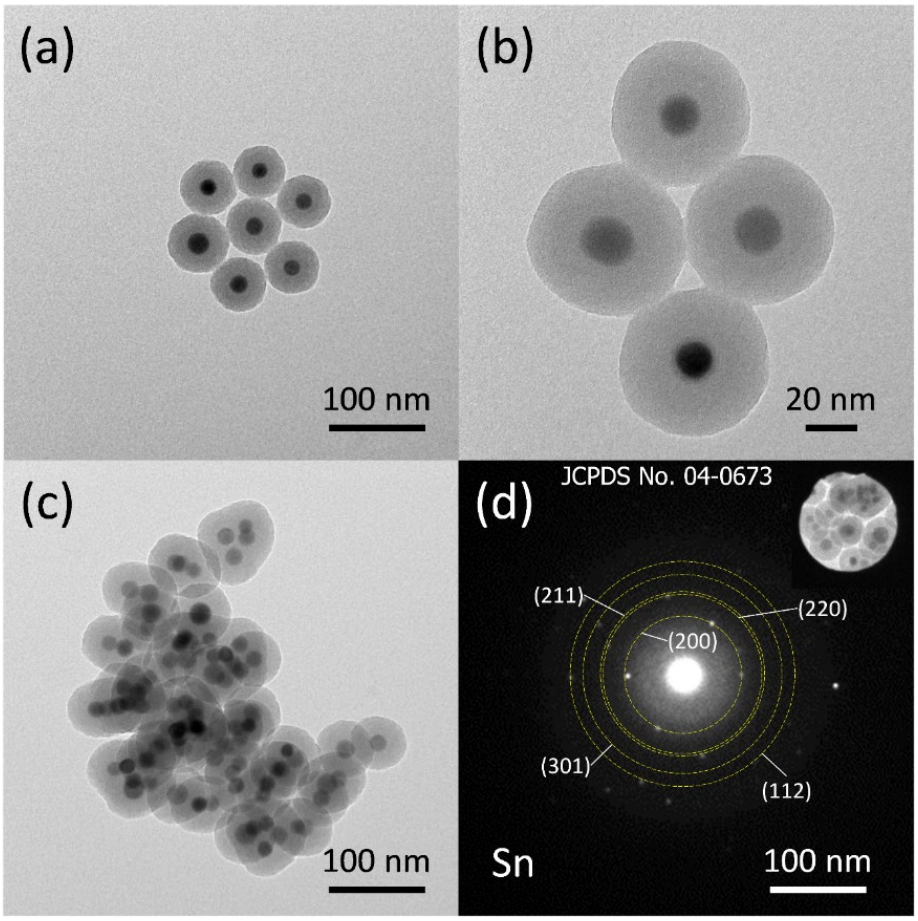

Figure S4.2. (a-c) TEM images of as-synthesized Sn@SiO_2 core-shell nanoparticles (core diameter: 20 nm, shell thickness: 20 nm). (d) SAED pattern of as-synthesized Sn@SiO_2 core-shell nanoparticles.

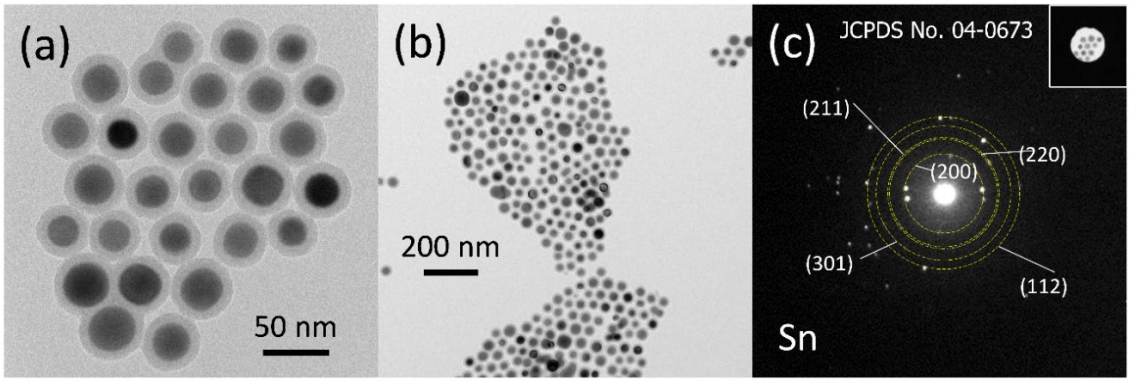

Figure S4.3. (a, b) TEM images of as-synthesized Sn@SiO_2 core-shell nanoparticles (core diameter: 30 nm, shell thickness: 8 nm). (c) SAED pattern of as-synthesized Sn@SiO_2 core-shell nanoparticles.

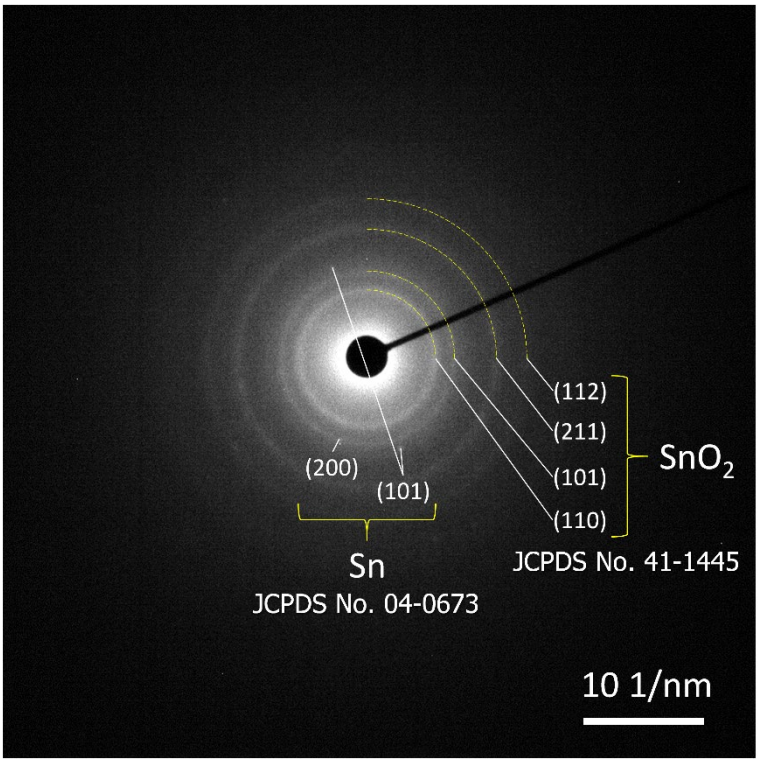

Figure S4.4. SAED pattern of hollow structure shown in Figure 1d.

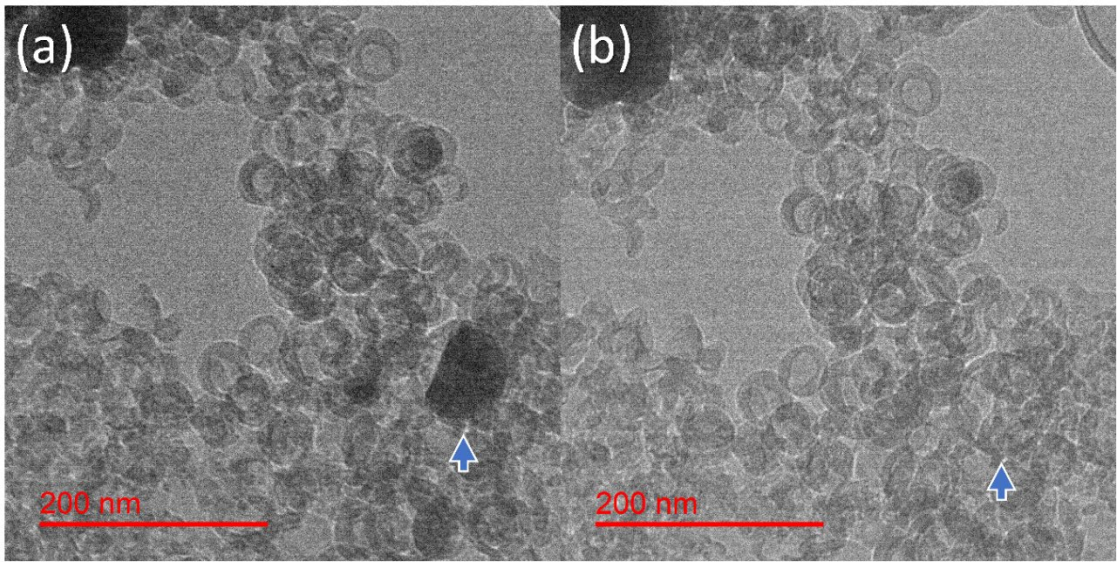

Figure S4.5. (a) TEM image of Sn@SiO_2 (blue arrow) with hollow SiO_2 structure surrounded (t_0). Interconnection of hollow silica structure is shown which provides the diffusion paths for Sn. (b) TEM image of as-formed hollow SiO_2 structure (blue arrow) after heating process.

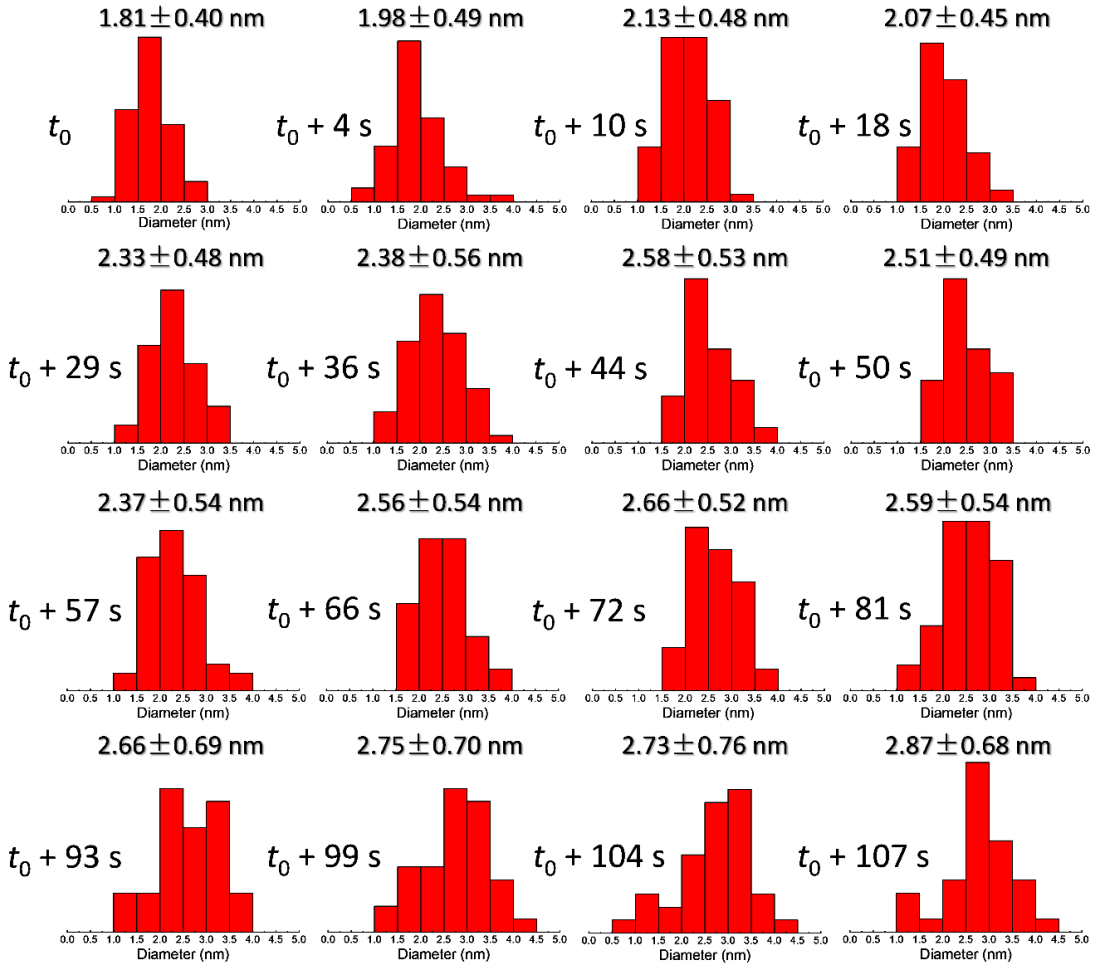

Figure S4.6. Size histogram of Sn nanoparticles appeared in SiO_2 structure (shown in Figure 4) during heating observed via in-situ TEM.

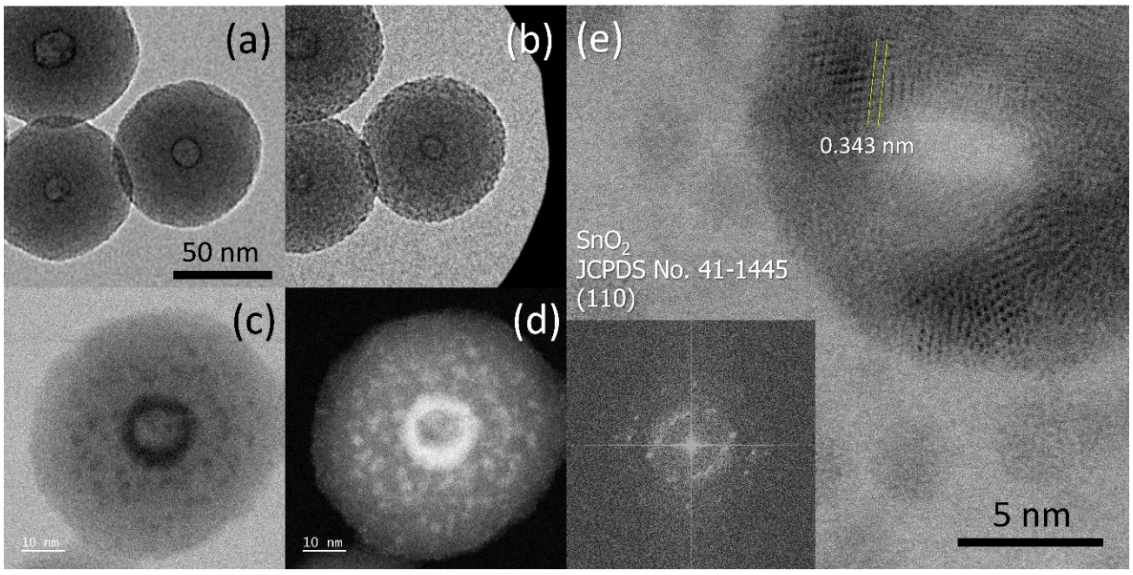

Figure S4.7. TEM images of void shrinkage in as-formed hollow SiO_2 structure by heating in a DSC (a) before and (b) after electron beam focusing. (c) STEM, (d) HAADF-STEM image and (e) High-resolution TEM image of h-Sn@SiO_2 after electron beam focusing. Inset in (e): corresponding fast Fourier transform (FFT) pattern.

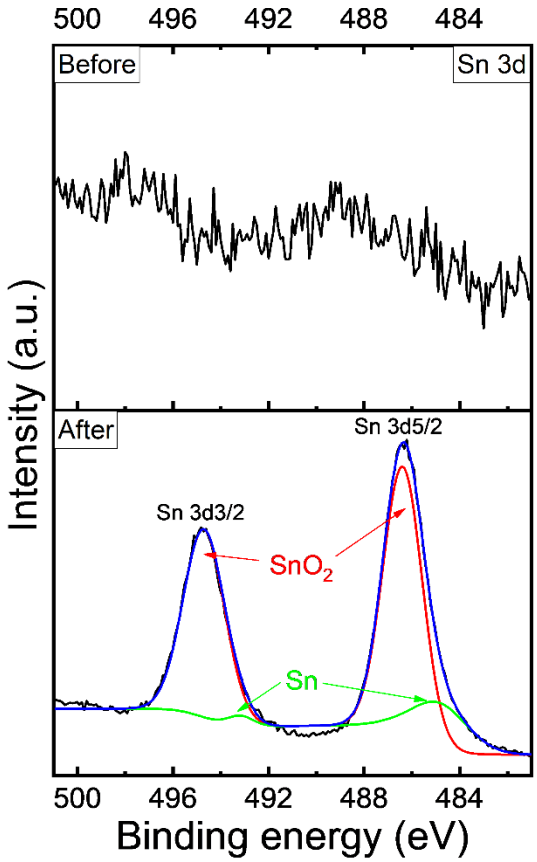

Figure S4.8. XPS narrow scan of Sn@SiO_2 core-shell nanoparticles before and after heating in DSC for diffusion.

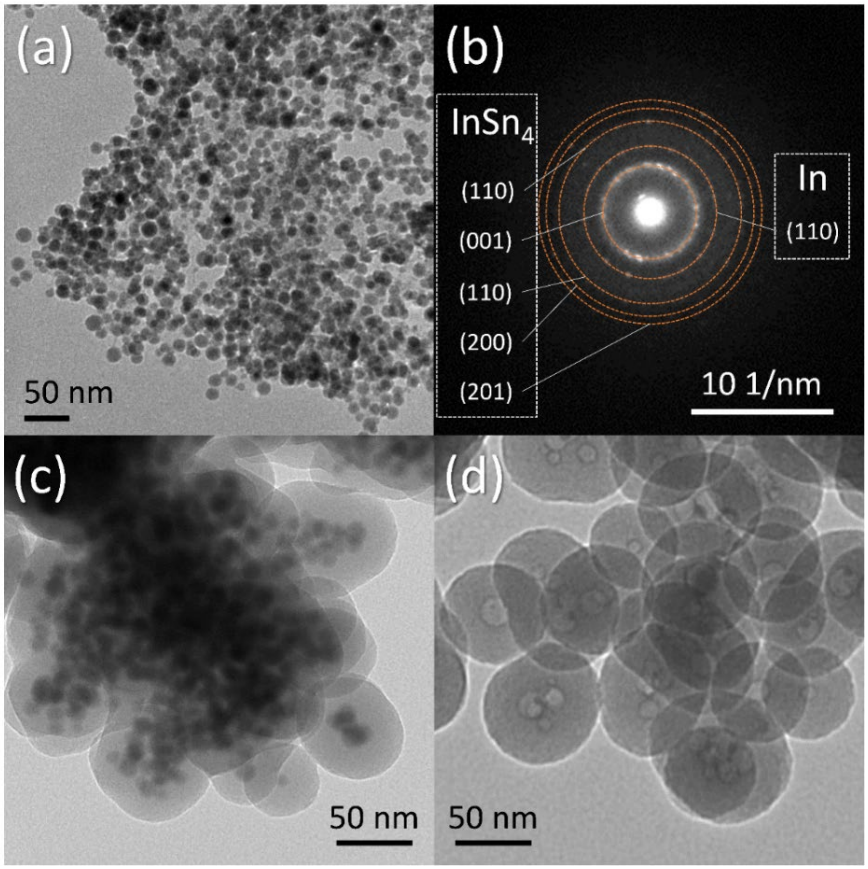

Figure S4.9. TEM image of as-synthesized (a) $InSn_4$ nanoparticles (c) $InSn_4@SiO_2$ core-shell nanoparticles. (b) SAED pattern of as-synthesized $InSn_4$ nanoparticles. (d) $InSn_4$ nanoparticles after heating in a DSC (from 25°C to 300°C, 10°C/min, loaded in a sealed Al pan).

Acknowledgments

Looking back to my 3-years-study for pursuing the Ph.D. degree, I have gained a lot of thoughts, feelings and experiences that may affect the rest of my whole life, which make me realize that a Ph.D. degree is not an ending but more likely a new starting point with many expectations and ideas. During this period, I received so much help from different people. Without their help, I would not able to finish this thesis.

First, I would like to express my sincere appreciation to my supervisor, Prof. Tetsu Yonezawa, who taught and trained me a lot, and set a good example in my life with his profound knowledge and creative academic thinking, which I can never forget. Meanwhile, I would like to sincerely thank Assist. Prof. Mai Thanh Nguyen, who spent a lot of time and provided the guidance for my research and experiments with great patience. In addition, I would like to thank Mr. Hiroki Tsukamoto for his technical support in using many of our facilities, and Assist. Prof. Yohei Ishida, for his important academic advices.

Our group members from Novel Material Hybrid Engineering Laboratory, Hokkaido University, also helped me a lot during my Ph.D. study. These members are Lyn Marie Z. De Juan, Masamu Nishimoto, Huang Zhong, Deng Lianlian, Islam MD. Saiful, Daichi Matsumoto, Ikumi Akita, Saw Min Jia, Kunihiro Narita, Yu Kai, Shi Jiajia, Chau Yuen Ting Rachel, Deng Dan. Thank you for the great support. In addition, I want to thank all the students in our group, thanks for your cooperation and help.

There were many professors and staffs who provided me their valuable advices, technical support and equipment for my experiments. They are Prof. Seiji Miura, Prof. Kazuhiko Iwai, Prof. Masatoshi Sakairi, Prof. Shigeo Arai, Prof. Cheng-Yen Wen, Prof.

Tamaki Shibayama, Prof. Koji Fumoto, Profs. Atsushi Muramatsu, Dr. Tomoharu Tokunaga, Dr. Kiyoshi Kanie, Mr. Takashi Tanioka, Ms. Ryoko Kurishiba, Ms. Rena Ishikawa, Mr. Keita Suzuki, Mr. Takashi Endo, Ms. Minako Kondo, Mr. Kimitaka Higuchi. Thanks to their kind help and professional support, I have learned a lot from them.

I would like to express my thanks to my fartherland, China, the place where I was born and grew up. The 20 years of study in China gave me the foundation to go further. I am also appreciated for the CSC scholarship provided by the Chinese government, which supported my study in Japan.

Finally, I would like to say thank you to my parents, who raised me with their patience and diligent work. They always support me and respect to every decision I made and help me keep to the straight and narrow. Last but not the least, I would like to say thank you to my dear wife, Yanan Ye, who gives me the biggest support in everything and makes me feel like the luckiest man in the world. Our conversation always gave me unexpected new ideas. And my daughter, Zhihan Zhu, I hope you are happy and healthy every day.

Shilei Zhu

In Sapporo

Publication list

[1] Zhu, S.; Nguyen, M. T.; Fumoto, K.; Kanie, K.; Muramatsu, A.; Yonezawa, T., Sn Nanoparticles Confined in Porous Silica Spheres for Enhanced Thermal Cyclic Stability. *ACS Appl. Nano Mater.* **2018**, 1 (8), 4073-4082.

[2] Zhu, S.; Nguyen, M. T.; Tokunaga, T.; Yonezawa, T., Size-Tunable Alumina-Encapsulated Sn-Based Phase Change Materials for Thermal Energy Storage. *ACS Appl. Nano Mater.* **2019**, 2 (6), 3752-3760.

[3] Saw, M. J.; Nguyen, M. T.; Zhu, S.; Wang Y.; Yonezawa, T., Synthesis of Sn/Ag-Sn nanoparticles via room temperature galvanic reaction and diffusion. *RSC Adv.*, in press.

[4] Zhu, S.; Nguyen, M. T.; Tokunaga, T.; Wen, C.-Y.; Yonezawa, T., From Core-Shell to Yolk-Shell and Hollow: Controllable Nanostructure via Liquid Metal Diffusions. *Submitted.*

Conference

[1] Poster presentation, 2017 Autumn Meeting of The Japan Institute of Metals and Materials, S. Zhu, M. T. Nguyen, T. Yonezawa “Synthesis of Sn Nanoparticles Confined within Mesoporous Silica Spheres”

[2] Oral presentation, 化学系学協会北海道支部 2018 年冬季研究発表会, S. Zhu, M. T. Nguyen, T. Yonezawa “Synthesis of Sn Nanoparticles Embedded in SiO_2”

[3] Poster presentation, 日本金属学会、日本鉄鋼協会両北海道支部合同平成３０年度サマーセッション S. Zhu, M. T. Nguyen, T. Yonezawa “Synthesis of InSn Alloy Nanoparticles for Thermal Storage”

[4] Oral presentation, 平成３０年度日本鉄鋼協会・日本金属学会両北海道支部合同冬季講演大会 S. Zhu, M. T. Nguyen, T. Yonezawa “Facile Synthesis of Al_2O_3 Coated Sn ($Sn@Al_2O_3$) for Reversible Thermal Energy Storage”